# CRYSTALLIZATION KINETICS, STRUCTURAL AND OPTICAL PROPERTIES OF In-Se-Bi BULK AND THIN FILMS FOR REVERSIBLE PHASE CHANGE MEMORY APPLICATIONS

**MUCHIRA IRENE WANJIKU (Msc)**

**I84/32275/2015**

**A Thesis Submitted In Fulfilment of the Requirements for the Award of the Degree of Doctor of Philosophy (Material Science) in the School of Pure and Applied Sciences of Kenyatta University**

**December, 2021**

# DECLARATION

I declare that the work presented in this thesis is my original work and has not been presented for a degree in any other university or any other award.

**Signature**.....Were..... **Date**.02/12/21.....

**Muchira Irene Wanjiku** **I84/32275/2015**
Department of Physics

**SUPERVISORS**

We confirm that the work reported in this thesis was carried out by the candidate under our supervision

**Signature**.....Mfaye..... **Date**.....02/12/2021

**Dr. Walter K. Njoroge**
Department of Physics
School of Pure and Applied Sciences
Kenyatta University

**Signature**.....Munji..... **Date**.....02-12-2021

**Dr. Mathew K. Munji**
Department of Physics
School of Pure and Applied Sciences
Kenyatta University

**Signature**.....Mokhotjwa..... **Date**.02/12/21.....

**Prof. Simon D. Mokhotjwa**
Department of Physics
University of South Africa

**DEDICATION**

TO

Sons; - Innocent Kayiindi and Ian Christian Muchira

Daughters; - Ivy Mumbi and Yvonne Njambi

## ACKNOWLEDGEMENTS

Most importantly, I would like to thank the almighty God for his care and strength during the entire period of this study.

I am immensely grateful to my supervisors Dr. Walter K. Njoroge, Dr. Mathew K. Munji and Prof. Simon D. Mokhotjwa for their research guidance, support and encouragement which made this work a success.

I would also like to sincerely thank Prof Hendrik Swart, Dr. Luyanda Noto and Dr. Raphael Nyenge for their professional support, research facilitation and meaningful interaction during the entire research period.

Many thanks to University of South Africa (UNISA) and University of the Free State (UFS) for the support and opportunity to do research in their laboratories. I am sincerely indebted to Prof. Simon D. Mokhotjwa who went out of his way to make this possible.

I thank my fellow researchers and staff of the department of physics University of South Africa (UNISA), University of the Free State (UFS) and Kenyatta University for the assistance and support they accorded me during research.

Big thanks to National Research foundation (NRF), African Development Bank (ADB) and Organization for Women in science (OWSD) for funding this research.

Special thanks go to my late husband Engineer James Mwaniki for his huge support during the study. He sacrificed a lot to take care of our children when I was away at South Africa for laboratory work. I would like to thank sons Innocent and Ian, daughters Ivy and Yvonne for their support, love and understanding all through. Last but not least, my truthful indebtness to my parents and siblings for their fundamental moral support.

# TABLE OF CONTENTS

## LIST OF FIGURES

## LIST OF TABLES

## LIST OF ACRONYMS AND ABBREVIATIONS

| | |
|---|---|
| A | Absorption coefficient |
| DRAM | Dynamic Random Access Memory |
| DSC | Differential Scanning Calorimetry |
| EDS | Energy Dispersive Spectroscopy |
| Eg | Band gap |
| Ei | Imaginary dielectric constant |
| Er | Real dielectric constant |
| FE-SEM | Field Emission Scanning Electron Microscopy |
| FWHM | Full width at half maximum |
| GST | $Ge_2Sb_2Te_5$ |
| In-Se-Bi | Indium selenium bismuth |
| MBE | Molecular Beam Epitaxy |
| n | Refractive index |
| NVM | Non-Volatile Memory |
| PCM | Phase Change Memory |
| PLD | Pulsed Laser Deposition |
| PMT | Photomultiplier Tube |
| PRAM | Phase Change Random Access Memory |
| PROM | Programmable Read Only Memory |
| PVD | Physical Vapour Deposition |
| ROM | Read Only Memory |
| RW | Rewritable |

| | |
|---|---|
| S | Sulphur |
| Se | Selenium |
| SEM | Scanning Electron Microscopy |
| $T_c$ | Crystallization temperature |
| Te | Tellurium |
| TEM | Travelling Electron Microscopy |
| $T_g$ | Glass transition temperature |
| XPS | X-ray Photoelectron Spectroscopy |
| XRD | X-Ray Diffraction |
| $\lambda$ | Wavelength |
| $\sigma$ | Conductivity |

## ABSTRACT

A detailed study of crystallization kinetics and structural properties of In-Se-Bi alloys has been carried out in this research. Kissinger's analysis method was employed to investigate crystallization kinetics of the material sample. Electrical, morphological and optical characteristics have also been studied. Bulk samples of $In_2Se_3$ doped with Bi were synthesized using melt quenching technique. The elemental composition of the bulk samples was realized using Field Emissions Scanning Electron Microscope (FE-SEM) attached with Energy Dispersive Spectroscopy (EDS). To investigate thermal properties of the samples, Differential Scanning Calorimetry (DSC) technique was employed. DSC runs were done at 5, 10, 15 and 20K/min heating rates in dry nitrogen ambient at 200 ml per minute flow rate in isothermal conditions. X-ray diffractometer (XRD) technique was used to determine the structural properties of the samples. Copper target was used as the X-ray source of wavelength 1.54Å (CuKα1). The 2θ spectrum scan ranged from 5 to $90^o$ at a speed of $2^o$per minute. The XRD results showed the as-deposited samples were amorphous which upon annealing changed to polycrystalline. To deposit In-Se-Bi thin films, Pulsed laser deposition (PLD) technique was used. Electrical characteristics tests were carried by four point probe using Keithly 237 source meter interfaced with a computer. Electrical resistivity was found to decrease from 85.19 MΩcm to 22.96 MΩcm with increase in percentage bismuth. Elemental mapping carried out on the thin film samples using FE-SEM equipped with EDS revealed irregular distribution of spherical particles. Bulk samples showed agglomeration of particles without a definite shape. To determine optical band-gap, Kubelka-Munk function was applied on Ultraviolet Visible Spectroscopy (UV-VIS) reflectance spectrum. The optical band gap values were higher for the doped samples as compared with the un-doped. The values ranged from 1.36 eV to 1.30 eV for as-synthesized powder samples. There was decrease in optical band gap with increase in bismuth concentration. Similar findings were made for annealed powder samples where band gap values decreased from 1.85 eV to 1.79 eV as percentage bismuth increased. Photoluminescence (PL) properties were studied by use of He-Cd laser of wavelength 325 nm. Emission increased with increase in bismuth concentration for both as prepared and annealed powder samples. X-ray photoelectron spectroscopy (XPS) output showed that bismuth was present in all doped samples. Activation energy of the samples was determined using Kissinger equation. It was found to decrease from 0.231 eV to 0.172 eV with increase in percentage bismuth for values with 0% Bi to 6% Bi concentration. However, activation energy increased with bismuth concentration for higher bismuth concentration of 8% Bi and 10% Bi. XPS studies confirmed elemental composition of the samples where for indium $3d_{5/2}$ peak was at 445.0 eV and $3d_{3/2}$ peak was at 452.5 eV binding energies. The two peaks are due to spin-orbit splitting of the d orbitals. XPS spectrum for selenium showed a peak for 3d orbitals at 54.3 eV binding energy. Bismuth exhibited two asymmetrical peaks at $4f_{5/2}$ and $4f_{7/2}$ respectively. In conclusion, addition of Bismuth to the binary alloy of indium and selenium enhanced its qualities for use in phase change memory applications in terms of low power consumption and less switching time due to decrease in resistivity and activation energy.

# CHAPTER ONE

# INTRODUCTION

## 1.1 Background of the study

Memories form part of our day to day life. Starting from cell phones to other electronic gadgets in our homes and offices, we are surrounded by memory devices. Therefore there is increasing demand for memory which is affordable and meets our needs as technology scales to the next level. Flash memory, a non-volatile memory technology has been in use in trying to meet the memory demand in today's society. However, scaling is proving a challenge (Miyaji *et al.,* 2011; Miyaji *et al.,* 2012). Therefore there is need for more advanced technology to provide solution to this problem. Phase change memory is a key area researchers are currently working on to come up with an alternative technology. This new technology is aimed at providing high storage density, low power consumption, high write speed and prolonged cycle. In order for the phase change memory devices to compete with flash devices, the issue of data retention at high temperature has to be addressed. Phase change memory employs phase change materials which belong to a group called chalcogenide glasses. These materials change phase upon application of electrical or thermal energy and the change is reversible.

Chalcogenide glasses fall in group six elements in the periodic table. For quite some time, a lot of research has been going on concerning these materials (Rao and Mohan, 1980; Lathrop and Eckert, 1989 and Asokan *et al*., 1889) with respect to the physics involved and device technology. The flexibility and simplicity in synthesis of glasses by varying the constituents which results to variation in their short range order brings changes in

their physical properties. Therefore, it is possible to make changes in their properties as one desires for various applications in modern day technology. These materials have a myriad of applications which include memory chips, optical reversible phase change memory recording, optical fibres and memory devices (Suri *et al*., 2006). Apart from huge application of selenium in commercial devices, it also shows peculiar characteristic of reversible phase transformation (Tanaka, 1989; Aggarwal and Sangherra, 2002). This characteristic makes it outstanding in memory devices application. Selenium glasses when brought to a temperature higher than its glass transition temperature and then cooled rapidly, form amorphous phase and when allowed to cool slowly they become crystalline. The two amorphous and crystalline states are reversible and exhibits distinct electrical and optical characteristics which form the basis for reversible phase change memory shown in figure 1.1. Introduction of a metallic element such as indium (In), antimony (Sb), bismuth (Bi), lead (Pb) or a chalcogen such as tellurium brings outstanding changes in properties.

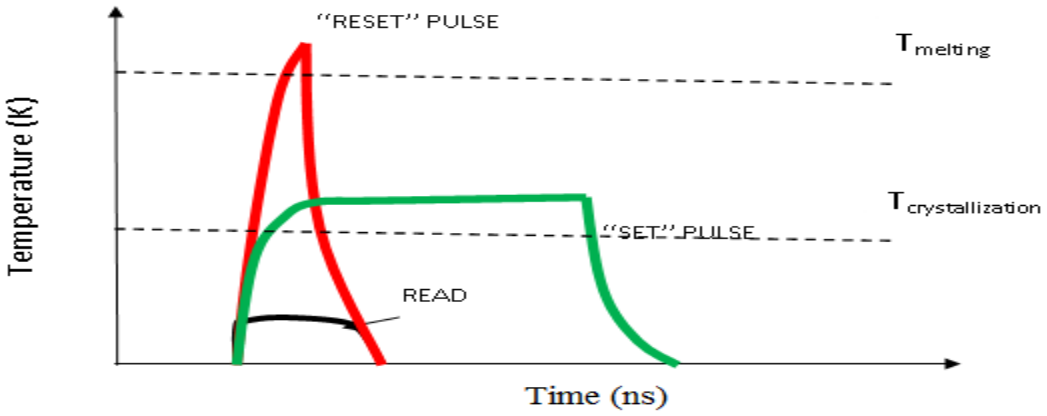


**Figure 1.1: Operations of a PCM showing read, reset and set pulses (Burr *et al.*, 2010)**

Phase change memory (PCM) has a unique property of scalability which ensures its ability to form structures in the nano scale range. Therefore, devices with high storage densities and rapid access times are possible with this PRAM technology. Scalability is the key in terms of placing PCM at a higher competitive edge as compared to existing flash technology. Current research is concentrating on a material with better write endurance and lower in cost while enhancing the performance of today's solid state devices.

Invention of fast crystallizing chacolgenide materials was the trigger for phase change memory technology. These materials include $Ge_2Sb_2Te_5$ and Ag-and In-doped $Sb_2Te$ (Yamada *et al.*, 1991; Tominaga *et al*., 1997). The properties to look in a material for PRAM are;- Wide separation of SET and RESET resistances, swift switching amidst amorphous and crystalline states, the two states being sensed without affecting them, last longer and fast speed (Burr *et al*., 2010).

Isothermal and non-isothermal methods have been utilized to evaluate crystallization kinetics on phase change materials (Cheng, 2010). Isothermal approach involves bringing the sample under test quickly to a glass transition temperature and generated heat is studied as a function of temperature. Non-isothermal phenomena takes place when a material is heated at a constant heating rate and generated heat plotted as function of temperature or time (Rao *et al*., 2008). Non-isothermal method can be used to get thermal analysis results in precise and relatively rapid way.

From literature, much focus has been on $GeSb_2Te_4$ and $Ge_2Sb_2Te_5$ alloys where studies involve determining their electrical, structural and optical characteristics (Yamada *et al.*, 1991; Mendoza-Galván and González-Hernández, 2000). The current study therefore involves the study of $In_2Se_3$ doped with Bi as a substitute material for PRAM implementation.

### 1.2 Problem Statement and Justification

$Ge_2Sb_2Te_5$ compound has been studied for a long time for phase change memory devices application. Nevertheless there are many shortcomings which have arisen with this material. These include low temperature of crystallization which affects the capability to maintain data at elevated temperatures and low crystalline resistance leading to high RESET current of PRAM memory devices.

Presently, vibrant researches are ongoing to come up with superior materials that meet today's technological needs and come up with a commercially viable PRAM memory cell which has the following characteristics;- Swift reversible transition, High cyclic reliability, data retention for a long time and economical in consumption of power. It has been established through research that indium selenide alloys are excellent materials for PRAM application owing to better characteristics compared to GST (Agarwal *et al.*, 1991). These include; - A higher crystalline resistance, a simple crystal structure and lower atomic constituents.

In spite of great potential information of technological application of chalcogenide alloys, little information is presented about their kinetics of crystallization. Consequently the current study systematically analysis crystallization kinetics, structural and optical properties of In-Se-Bi alloys in the process of exploring for a substitute material for PRAM applications.

## 1.3 Objectives

### 1.3.1 General Objective

To investigate crystallization kinetics, structural and optical properties of In-Se-Bi bulk and thin films for reversible phase change memory applications.

### 1.3.2 Specific Objectives

(i) To synthesis alloys of In_Se_Bi powder samples using melt quenching method

(ii) To deposit thin films of In_Se_Bi by pulsed laser deposition (PLD) technique

(iii) To study kinetics of crystallization of In_Se_Bi using Differential Scanning Calorimetry (DSC)

(iv) To determine optical properties of In_Se_Bi bulk and thin films samples

(v) To determine electrical properties of In_Se_Bi thin films samples

(vi) To determine structural properties of In_Se_Bi bulk and thin films samples

(vii) To investigate the effect of bismuth on band gap and activation energy of the In-Se-Bi samples

### 1.4 Rationale of the Study

Studies on Ge-Se-Bi have already been reported by Achamma *et al*., 2007. However, not much work has been reported on the crystallization kinetics, structural and optical analysis of $In_2Se_3$ doped with bismuth. Selenium based chalcogenide are known for their unique properties such as reversible phase transformation, and applications in switching and memory (Vazquez *et al.,* 2004; Singh *et al*., 2005). Chalcogenides studies are of intense interest because of their application in semiconductor memories. In particular, selenium has got a myriad of applications including switching and electronic memories devices. However, in its pure form, it has drawbacks such as low sensitivity and a short life time. To overcome these shortcomings, selenium can be doped with other elements such as bismuth, tellurium and indium.

Bismuth addition causes excellent alterations in optical characteristics and produce p to n transition in the glasses (Tohge *et al.,* 1979; Nagels *et al.,* 1981; Nagels *et al.,* 1983; Tohge *et al.,* 1983). Chacogenide materials have been reported to have large refractive index values, low phonon energy, infrared transparency and high photosensitivity. These properties make them good candidates for electronic and optical devices (Zogg and Arnold, 2007; Xia *et al.,* 2010). This study systematically analyzed In-Se-Bi alloy for its suitability in PCM applications. In the current work, a full study of the structural, optical and electrical properties of chalcogenide glassy In-Se-Bi bulk and thin films was made. The suitability of $In_2Se_{3:}$ X% Bi for use as a reversible phase change memory device and device specifications was concluded from the results.

# CHAPTER TWO

# LITERATURE REVIEW

## 2.1 Related Works

Gupta *et al.,* 2021 explored on recent developments on PCM, current challenges and future prospects. DRAMs, Flash memory, SRAM and EPROMs were found to have limitations. These include SRAMs being relatively expensive, EPROMs requiring high power and also possess poor flexibility. Phase change memory operates in a picosecond timescale and that is why they are faster than flash memory. However challenges which include the reduction of heating in the PCM cell because excessive heat may damage the PCM cell. Therefore Suitable phase change materials are required so as to increase the rate of crystallization and amorphization. There is a challenge to reduce the device size so as to minimize power consumption and also a need to innovate fast switching materials so as to increase data rate to achieve a memory device, capable of non-volatile operations beyond gigahertz data-transfer rates. The principal aim of today PCM developers is to increase the density of memory and decrease energy and power utilization.

Le Gallo and Sebastian, 2020 carried out an overview of PCM which is arguably the most mature resistive memory technology of the present day. They reported that PCM has been studied and mass-produced, for instance in DVDs and Blu-ray disks. It has already appeared as a digital memory product on the market. Its attractive properties such as multi-level storage, fast read/write latency, non-volatility, good cycling endurance and good scalability make it an ideal candidate for applications in novel computing fields. However, there are still several questions that remain to be answered regarding the

crystallization mechanism, electrical transport, relaxation effects, and noise in PCM. Besides, there are also outstanding issues associated with the fabrication process of PCM for further scaling and integration with advanced CMOS technology nodes. Hence, there is definitely a demand for enhancing our understanding of PCM device physics, refining the already existing physics based models of PCM, and potentially improving them based on more accurate physics, in order for PCM to be successfully integrated as memory and computing elements in next generation computer systems.

Indium and selenium elements have got direct band gap energy. The employment of these materials in many devices fabrications is mainly due to its optical and electrical properties. Singh *et al.,* 2019 did a research on $In_xSe_{100-x}$ thin films. They realized there was change in morphology with increase in indium content which verified structural phase transition. Also the optical band gap calculated using Tauc's plots varied from 1.88 eV to 1.12 eV and was found to decrease with indium content.

Nilanthy *et al.,* 2018 demonstrated that $\gamma$-InSe and the $\beta$ and $\gamma$ phases of $In_2Se_3$ can be grown epitaxially on $\varepsilon$-GaSe substrates using a physical vapour transport method. The $In_xSe_y$ epilayers were characterized using Raman, photoluminescence, X-ray photoelectron and electron dispersive X-ray spectroscopies. Each $In_xSe_y$ phase and stoichiometry exhibited distinct optical and vibrational properties, providing a tuneable photoluminescence emission range from 1.3 eV to approximately 2 eV suitable for exploitation in electronics and optoelectronics. The group also found out that crystal structures of $\gamma$- and $\delta$-$In_2Se_3$ are hexagonal and trigonal respectively and the

rhombohedral crystal structures of $\alpha$- and $\beta$-$In_2Se_3$ phases were very similar to each other. For $\gamma$-InSe, the room temperature PL emission was centred at an energy $E$ = 1.26 eV, s-grown $\alpha$-$In_2Se_3$ had a peak at $E$ = 1.41 eV, $\beta$-$In_2Se_3$ at $E$ = 1.43 eV and $\gamma$- $In_2Se_3$ is peaked at $E$ = 1.95 eV.

Yong *et al., 2*014 conducted a research on effects of pressure and deposition time on the characteristics of $In_2Se_3$ films grown by magnetron sputtering. Single-phase κ-$In_2Se_3$ was prepared at 4.0 Pa while, additionally, γ-$In_2Se_3$ was recognized when the working pressure was lower than 4.0 Pa. The band gap decreased from 2.6 to 2.1 eV with increasing working pressure from 0.5 to 4 Pa. At higher pressure, the films showed a granule-like surface morphology combined with small irregular grains. The optical transmittance of the films decreased from 95% to 40% and the band gap varied in the range from 2.9 to 2.0 eV with increasing film thickness from 80 nm to 967 nm, respectively.

$In_2Se_3$ naturally appears in five distinct phases i.e. a, b, c, d and j. These are centered on the material's optical band gap (Julien *et al.,* 1990). The different phases in existence in the material compete during the growth process of the film and result in amorphous and polycrystalline phases in a sample (Madugu *et al.,* 2014). The indium and selenium semiconductor alloy material has been studied extensively for photovoltaic devices applications (Gopal *et al.,* 2005; Ates *et al.,* 2009) and semiconductor memory devices. $In_xSe_y$ typically exist in distinct forms such as InSe, $In_2Se_3$, $In_4Se_3$ and $In_6se_7$ (Parlak and Ercelebi, 1998). A wide band gap (1.80 eV) c-$In_2Se_3$ (Harrero and Otega, 1987) can be

applied as a window layer whereas b-$In_2Se_3$ with a band gap of 1.55eV can be utilized as an absorber layer in fabrication of solar cell devices. A group of researchers found out that c-$In_2Se_3$ band gap can be in the range of 1.70–1.80 eV (Harrero and Otega, 1987; Ates *et al.,* 2009). Thin films from indium selenide material have been made by employing different deposition techniques which includes vacuum evaporation (Damon and Redington, 1954; El–Sayed, 2004).

Lovu *et al.* (2002) conducted a research to establish the effect of metallic dopants on the optical and photoconductivity characteristics of As–Se chalcogenide materials. Chalcogenide glasses are known to be p-type semiconductors. The valence band of these materials consists of lone pair orbitals (Kolobov 1996; Kastner 1972). Structural defects have little effect on the valence band which is a lone pair band as compared to conduction band with anti-bonding orbitals. This makes the scope of localized tail states at the valence band edge lower than the localized states at the conduction band edge. As a result, the number of excited electrons above the conduction band mobility edge becomes lower than the number of excited holes below the valence band mobility edge. Consequently the materials are p-type semiconductors (Kolobov, 1996). The materials also have defect states which are positively and negatively charged called valence-alternation pairs (Kastner *et al.,* 1976). Fermi level is usually pinned midway the band gap by these valence-alternation pairs making them resistant to doping (Mott, 1967). However research has shown that addition of charged particles can alter the ratio of valence-alternation pairs and alleviate the fermi level (Mott, 1976). Bismuth has been identified as one of the additives which can alter the ratio of valence-alternation pairs.

When the amount of charged additives is more than the valence-alternation pairs, the chalcogenide material may show the reversal from p-type to n-type charge carrier. Tohge *et al.,,* 1980 proved the p-type to n-type transition in In-Se and Ge-Se glasses after Bi and Pb addition respectively.

Ovshinsky (1968) discovered a phase change optical memory device in 1960s which could store binary bits by utilizing phase transition from amorphous to crystalline of chalcogenide glasses brought out by laser beam. Since then there has been improvement in terms of materials with superior qualities and better operating efficiencies. Many compounds such as GeSbTe, InSbTe and GeTe have been employed as phase change materials, because of the easy deposition in amorphous phase. Mehta *et al.* (2004) carried out crystallization kinetics on Se-Te-Ag chalcogenide glasses by making use of DSC technique at various heating rates. Activation energy of crystallization carried out by Kissinger, Matusita and Bennett's relations was lower in ternary compound as compared to binary as a result of addition of silver. Hiereche and belhadgi (2007) carried out non-isothermal crystallization studies of glasses made up of GST alloys by utilizing DSC technique. They observed two phase transition temperature followed by two recrystallization temperature peaks. Activation energy values evaluated using Matusita, Kissinger and Ozawa models were greater in Tellurium than in GeTe.

Singh *et al.,* 2008 studied the outcome of annealing on structural properties and thermal effects on conductivity of $Se_{90}In_{10}$ by employing XRD and transient plane source (TPS) techniques. The researchers observed change in structural properties and thermal

conductivity after annealing at 50$^{o}$C for one hundred and twenty minutes as a result of structural transformation and relaxation. Research work on phase transformation, device performance and activation energy of thin films from Si doped GST was reported by Park *et al*. (2008). Analytical techniques such as four point probe, XPS and XRD were used where four orders of magnitude resistance contrast was established. Further, activation energy decreased with increase in amount of silicon added.

Goo *et al*. (2011) came up with a method of determining crystallization kinetics of $Ge_2Sb_2Te_5$ by In-situ resistance method of measurements. Modified JMAK equations were used to establish a linear relationship between logarithmic time and reciprocal temperature. Activation energy of crystallization obtained was 2.67eV. Matsuzaki *et al*. (2005) performed a research and found that oxygen doping of GST film led to high activation energy as a result of smaller grain size and give rise to improved data retention. N-doped GST single cell phase change memory appliances exhibited retention write times above ten years at eighty five degrees Celsius as established by Kim and Ahn, (2005). Results showed that activation energy is less in devices compared to blanket films due to damage induced during fabrication process and structural defects at boundary between GST and bottom electrode.

Kissinger and Fredman theories were used to investigate crystallization kinetics of selenium and indium glassy alloy. They concluded that activation energy is dependent on the fraction of material crystallized (Shukra *et al*., 2010). Morikawa *et al*. (2007) did some studies on indium doped GeTe for phase change material application. They found

out that indium doped GeTe had superior retention properties than GST for a period of ten years for a temperature range of 122$^{o}$C to 156$^{o}$C depending on fraction of indium used. Fayek *et al*. (2008) used differential thermal analysis to investigate crystallization kinetics of $Se_{0.62}Ge_{0.38}$ and $Se_{0.62}Ge_{0.35}X_{0.03}$ (X = 0, Bi, In and Sb) compound by varying the rates of heating. It was concluded that phase transition and recrystallization temperatures are influenced by rates of heating and composition of the sample. Both phase transition and recrystallization temperatures increased with increase in heating rates. In chalcogenide glasses knowledge on activation energy for crystallization is necessary in order to understand their thermal relaxation.

Choi *et al.,* 2009 conducted a research on heating rates effects on crystallization activation on thin films made of amorphous $Ga_2Se_2Te_5$alloy. In-situ electrical sheet resistance study showed crystallization activation energy values of 2.34eV for rates of heating less than 40$^{o}$C/min but at higher rates the values reduced to 0.49 eV. The decrease was as a result of reduction in activation energy of nucleation and growth of crystalline phase. El-Oyoun, 2000 did a research on crystallization kinetics of chalcogenide $Bi_{10}Se_{90}$ alloy under isothermal conditions by employing DSC. The average value of Avrami Index was 2.04±0.12, the activation energy of crystallization was 182.13±3.69kJ/mol and frequency factor of 3.520 ±33) x$10^{9}s^{-1}$.

Phase change memory cell was in the test market for mobile telephone in the year 2010 (Peter, 2010). Later another PRAM cell was developed in 2012 by Samsung Company (Choi *et al.,* 2012). In year 2012 July, Micron Company produced PRAM memory cells for use in mobile telephone devices (Micron technology, Inc. 2013). The cells produced

have exhibited the good qualities of PRAM such as fast erase times, fast write erase times, low cost per bit, low power consumption, scalability, long retention times and high endurance.

According to Schotmiller *et al.,* 1968, bismuth addition to some chalcogenides such as selenium leads to change of carrier from type p to n. Researchers (Wang *et al.,* 1995) looked at the effect of bismuth and tin on the structure of Ge-Se-Te. They used analytical techniques such as Differential Thermal Analysis, Fourier transform infra-red to expand the infra-red transparency region of the chalcogenides and XRD. They found out that addition of tin increased phase transition and recrystallization temperatures. Stability of amorphous phase and chemical durability of the material were also observed.

Researchers, El-Zahed and El-Korashy (2000), investigated how composition influences both the electrical and optical properties of $Ge_{20}Bi_xSe_{80-x}$ (x = 0, 5, 9, 10, 15, 20 and 25). They determined the optical band gap with different bismuth percentages. It decreased from 2.1 eV to 1.65 eV with bismuth percentage up to 10. There was a small change for bismuth percentage greater than ten. Also there was a great decrease in activation energy for bismuth percentage of up to 10. The energy decreased from 0.97 eV to 0.09 eV.

Addition of a dopant to a PCM material affects its characteristics. The performance of a PRAM cell is affected by the change in materials parameters. The table 2.1 shows some of these effects (Burr *et al.,* 2010).

**Table 2.1: Phase change material characteristics and effects on PRAM performance**

| Phase change material characteristic | Effects on PRAM performance |
|---|---|
| Crystallization temperature | Data retention in amorphous phase<br>SET power |
| Melting temperature | RESET power |
| Resistance in crystalline and amorphous phases | SET current<br>RESET current<br>On/OFF ratio |
| Threshold voltage | SET voltage |
| Thermal conductivity in amorphous and crystalline phases | SET power<br>RESET power |
| Crystallization speed | Rate of data reading/writing |

Bhat *et al.*, 2001 carried out a research which sought to find the role of defects in the change of carrier type upon addition of small amount of bismuth to germanium selenium alloy. They used photoluminescence spectroscopy on $Ge_{20}Se_{100-x}Bi_x$ and $Ge_{20}Se_{70-x}Bi_xTe_{10}$. They found out the alloy with low bismuth constituent showed luminescence but the alloy which exhibited n-type conductivity did not show. Research has shown that doping can result in enhancement of material properties for phase change memory application. For instance a dopant which makes a PCM material to have high crystallization temperatures, leads to improved data retention. This also helps when the cell is used for applications which involve high temperature. Also high resistance in amorphous and crystalline phases leads to decrease in the programming current which consequently reduces the power consumed.

Despite all these milestones, continued research is required to keep the PRAM in the competitive market of memory cells. From the previous research it is proven that PRAM cell is viable; however it faces some challenges which it needs to overcome. The device scaling and multilevel cell application need to be addressed. From literature review, we can deduce that there are other materials with superior qualities as compared to the known GST for PRAM applications. These materials exhibit higher crystallization temperature and higher speed of crystallization (Njoroge *et al*., 2001; Raoux *et al*., 2008). A modern day phase change memory technology requires rapid switching, low consumption of power, high storage density and improved retention of data. Therefore further research in materials and device technology is vital to achieve enhanced stability and retention of amorphous marks in elevated temperature. A material with minimal power consumption is paramount. For these reasons this research is based on kinetics of crystallization, structural and optical characteristics of In-Se doped with Bi bulk and thin films for PRAM applications.

# CHAPTER THREE

# THEORETICAL CONSIDERATION

## 3.1 Semiconductor Memory Technology

Memory is an array of storage cells. Semiconductor memories are part of modern day to day life. As a modern technology, there is need for improvement in terms of performance and storage density to be up to date with technological advancement. The high rate of technological growth has seen fast growth in very large scale integrated technology in terms of devices like tablets, smartphones, personal computers and sensors used in various applications. The technological industry need low power and reliable semiconductor devices as well as scalable devices in order to quench the thirst for the memory hungry modern society. Memory can be grouped into primary, secondary and tertiary memory. Primary memory consists of the internal memory of an electronic device. It is faster and expensive but loses data when power goes off. It is composed of registers, main and cache memories. On the other hand secondary memory refers to the peripheral devices. Data does not disappear when power is off. It consists of hard drives, CD drives, DVD drives, memory sticks and solid state drives. Tertiary memory is nonvolatile and slow. It is used to store data not required in the near future. An example is the optical jukeboxes.

Volatile memories need to be powered in order to retain data. Non-volatile memories do not lose data with power outages and therefore no need to refresh. Examples of volatile types of memories are static random access memories and dynamic random access

memories. They have fast read and write cycles hence good for use as primary cache memories.

Secondary and tertiary memories fall under non-volatile type of memory. The read only memory (ROM), programmable read only memory (PROM) and flash memories are examples of non-volatile memory. They do not have fast read write cycles. Flash disks, solid state drives, universal serial bus drives and memory cards use non-volatile memory technology.

Modern research focuses on the main memory in order to come up with a storage device which is fast and non-volatile. The said device should have speed that matches that of dynamic random access memory (DRAM) in terms of capacity and flash in terms of price. PRAM is a potential prospect for this extensive memory technology. The main qualities of this memory are robustness, low latency, durability and low cost.

### 3.1.1 Static Random Access Memory

Static random access memory (SRAM) is a volatile memory because it retains data only when the memory device is powered. Compared to DRAM which stores data inform of charge in a capacitor, SRAM does not need regular refreshing. Its operation speed is higher than that of DRAM and it is relatively expensive. It is mainly used as computers cache memory. It operates like a latch. The data remain in the memory once written provided the device remains connected to power. It stores data through switching of cross coupled inverters. SRAM memory cell consist of arrays arranged in rows and columns as

shown in figure 3.1. The rows are the word lines and columns the bit lines. Every cell has a distinctive address which is marked off by the joint of a row and a column. The cell is a bi-stable flip flop which is linked to the internal circuit by two access transistors.

During the instance when memory cell is not addressed, the access transistors are closed and the data latched in the flip-flop. This is the stable state of the flip-flop.

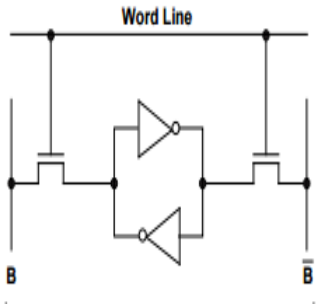


**Figure 3.1: Static RAM**

To select a cell, the access transistors are put on so as to connect the flip-flop to the internal circuit of the cell. The transistors are connected to the word line and the row is set at $V_{CC}$. The sides of the flip-flops are joined to the bit lines labeled B and $\bar{B}$ in figure 3.1.

To read the cell, the bit lines are joined to the sense amplifier which senses when logic one or zero is stored in the cell. To write data in to cell, data goes to the write circuit which writes the data onto the flip-flop. After the write and read process, the word line is set to zero. To ensure the data in the cell remains unaltered, it must be supplied with steady power which will not fluctuate beyond ±10% of $V_{CC}$.

### 3.1.2 Dynamic random access memory

Dynamic random access memory (DRAM) is a volatile memory which has an advantage compared to other memories because of its simple structure. Transistors and capacitors are small components which can fit in large number in a chip. It is therefore capable of attaining very high density levels. DRAM has the disadvantage of high power consumption because of its dynamic nature. It stores data through charging and discharging of capacitor. DRAM finds application where low cost and high densities are required. Due to its structural simplicity, DRAM is cheaper per bit compared to SRAM which is made up of four or six transistors. It is mainly used in the main memory of a computer.

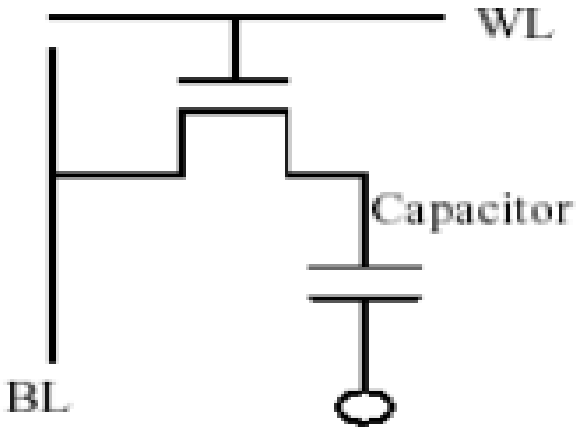


**Figure 3.2: DRAM**

The schematic diagram for DRAM is shown in figure 3.2. It is composed of a transistor and a capacitor. The capacitor assumes two states where it can be charged or discharged and the two states are taken to represent a 0 or 1 bits. Capacitors usually leak charge even when not in conducting state. Due to this the capacitors slowly discharges eventually losing the data. Loss of charge leads to loss of stored data. To prevent this loss, the cell

must be refreshed periodically to restore the charge. Each cell is accessed and refreshed during a refresh interval.

There are two lines connected to each DRAM cell. The word line controls the transistor gate and bit line is connected to the MOSFET channel which connects the sense amplifiers. DRAM cell has a support circuit which is responsible for writing and reading data and to refresh the memory cells. The circuitry is composed of sense amplifiers, address logic, read and write circuitry and internal registers.

The purpose of the sense amplifiers is to amplify the signal detected on the cell. The address logic selects the rows and the columns to initiate or terminate write or read operations. Internal registers initiate the refresh cycles as required. In order to write data, the row and column address of the particular cell is selected. Data is then taken to the input pins of the cell. The memory cell's capacitor is either charged or discharged depending on whether the cell stores logic 1 or logic 0.

### 3.1.3 Flash memory

This technology was invented by Dr. Fujio Masuoka in the year 1980 (Hwang *et al.*, 2003). Flash memory has a long life span and is robust because it can operate in areas under high pressures and temperatures. The most common type of flash memory in use is NAND flash. It has a storage capacity in the range of 512MB up to 256GB. It has fast read and write cycles. The erase times are 2 ms on average and it is also lower in cost.

It is a nonvolatile memory device which is capable of being programmed and erased. It has the properties of both ROM and RAM. It has many uses in today's modern technology world. For instance in digital cameras, laptop computers, personal digital assistants, mobile phones, solid-state drives, universal serial bus drives and MP3 players.

Flash memory resembles the electrically erasable programmable read only memory (EEPROM) in that it is programmed and erased using an electronic device. The main difference between EEPROM and flash is that EEPROM erase and rewrite the data byte by byte. On the other hand flash memory erases and rewrites its data in entire blocks making it faster than EEPROM.

A flash memory cell is a MOSFET which has two gates (figure 3.3). Below the control gate, a floating gate which is insulated using an oxide layer is fixed. The floating gate is isolated electrically by an insulating layer and therefore electrons on it are trapped till removed by an applied electric field. The memory cell stores data by charging and discharging the floating gate. When the floating gate is charged, current does not flow through the transistor. This is equivalent to logic 0. When the floating gate is discharged, the transistor conducts and this represents logic 1. The whole process is facilitated by supplying voltage between the control gate and source or drain.

Floating gate and control gate are segregated by a thin oxide layer. It links to the word line via the control gate. When there is a link, a logic bit 1 is registered in the cell. The value is changed to logic 0 through a process called Fowler-Nordheim tunneling. Flash

memory has advantages of high speed access, smaller size, solid state and light in weight compared to hard disks.

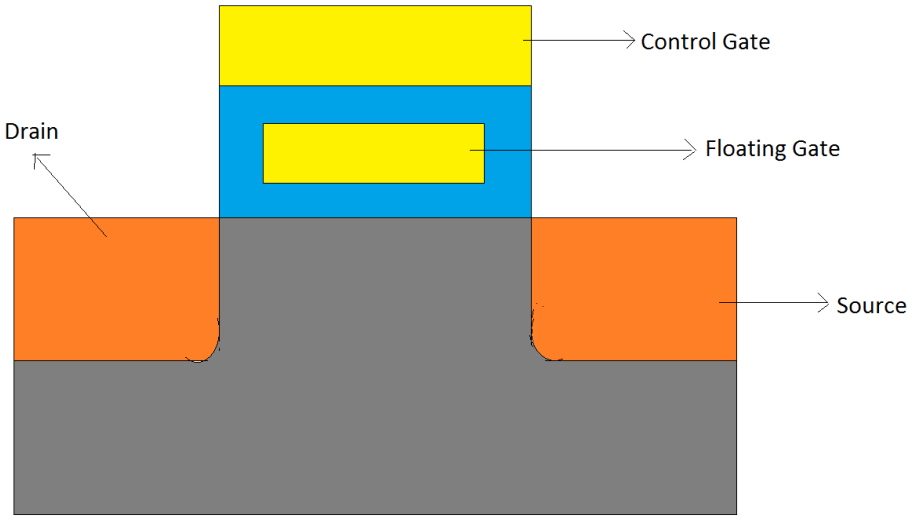


**Figure 3.3: A section of flash memory**

This memory device is made such that the transistors are arranged either in NOR or NAND configuration.

### 3.1.4 Phase change memory

DRAM and FLASH memories have got all the characteristics that a future memory technology requires. Phase change memory (PCM) is a potential candidate which can meet all these characteristics and overcome the scalability problems faced by the flash technology. It is a non-volatile semiconductor memory made up of one transistor and a resistor. The PCM material is placed between top and bottom electrodes of a memory device and belongs to a group called chalcogenides. They exist in amorphous as well as crystalline states at room temperature. It has the ability to be switched many times

between the two states with pronounced electrical and optical properties up to three to six orders of magnitude.

They demonstrate switching phases from low resistance and highly reflective phase called crystalline to a high resistance amorphous phase. This field has attracted many researchers owing to myriad of characteristics which make them suitable in applications like solar cells, data storage devices, laser and imaging in medical fields. These optical properties include wide window of transmission between visible and infrared and high absorption coefficient.

A PCM makes use of the unique behavior of chalcogenide materials of reversible change between amorphous and crystalline states using optical or electrical means. An electric current or laser when passed through a heating element produces heat which heats the material and if rapidly quenched becomes amorphous or when cooled over a long period changes to crystalline. This phenomenon makes use of resistance or reflectance difference between the two states, amorphous phase having high resistance or low optical reflectance and crystalline phase with low resistance or high reflectance. A low voltage is applied to sense the resistance state when reading the cell. To transition from amorphous to crystalline, electrical or optical means are applied. In electrical switching an electric pulse is applied. Starting with a crystalline material, to write involves creating an amorphous mark by applying a high peak electrical pulse to melt the material and then cooling it abruptly. To erase the mark a low peak electrical pulse is administered such that the cell attains only the crystallization point for a long duration thus crystallizing the

material. In optical switching a high energy laser is passed to a crystalline material for a short period to create an amorphous mark. Similarly to erase, a moderate energy laser is passed for a longer period thus converting the amorphous phase to crystalline.

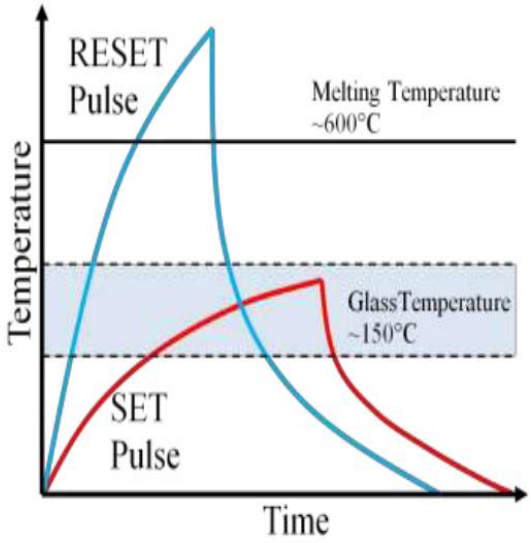


**Figure 3.4: Phase change memory time versus temperature to attain different states**

The two phases are different in their physical characteristics. The amorphous phase has high conductance and reflectance compared to the crystalline phase. In optical recording reading is done by differentiating the reflectance of the two phases using low energy lasers. In electrical data recording, reading is accomplished by use of low electrical pulses to detect electrical conductivity. PRAM faces some challenges as a next generation memory device. These include: decreasing the RESET current, reducing SET times and preventing resistance drift when in amorphous phase. This calls for intensive research to mitigate these shortcomings to enhance the overall performance of a PRAM device.

Figure 3.4 illustrates the whole process of recording data in chalcogenide materials. Figure 3.5 shows the I-V characteristics of a typical PRAM cell. From the figure it is clear that there is a huge contrast between crystalline and amorphous stage for voltages below threshold voltage $V_t$. PRAM has a very high resistance in amorphous RESET phase and the cell will remain at this state for voltages below $V_t$. If the electrical pulse is withdrawn the cell will retain its RESET state. However, if the voltages are above the $V_t$ and the electrical pulse is passed for sufficient time, the PRAM cell switches to SET crystalline phase.

RESET process involves a lot of power consumption because its value has to be equivalent to phase change material's melting temperature. The RESET current is dependent on the device structure, electrical resistivity and thermal conductivity of the material. The SET process takes time for the cell to crystallize and therefore it determines the speed of the device.

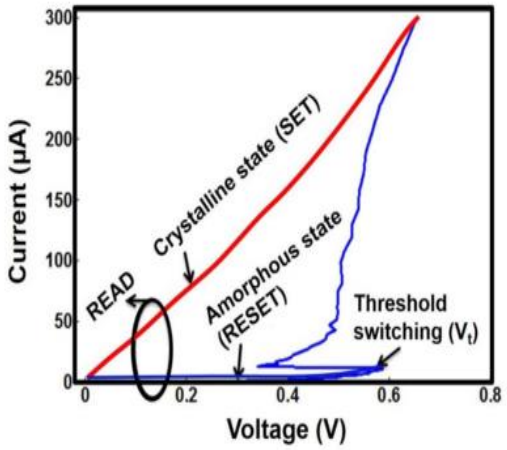


**Figure 3.5: I-V characteristic of a PCM cell (Karpov *et al.*, 2007)**

The I-V plot highlights the switching phenomena for the phase change memory device. From figure 3.5, once the conduction in amorphous phase reaches the threshold voltage $V_t$, it switches to the highly conducting crystalline phase.

Increase in voltage in amorphous phase leads to increase in conductivity. When the voltage reaches the threshold value, the cell goes to switching state as shown by the snap back on the figure 3.5. At this state, the cell can recrystallize if the pulse is withdrawn over a wide range of time. Or retain the amorphous phase if the current pulse is withdrawn abruptly. The crystalline phase shows increase in conductivity as the voltage increases. This is after the voltage reaches 0.5 V as this is the case with semiconductors. This voltage is called the knee voltage beyond which a semiconductor behaves like a conductor.

## 3.2 Deposition Techniques

### 3.2.1 Physical Vapour Deposition

Physical vapour deposition (PVD) process takes place when a material is vaporized from liquid or solid state. It is also known as atomistic deposition process. The atoms then move through vacuum or a low pressure gaseous plasma and adhere to the substrate (Mattox, 1998). This process is commonly used for thin films deposition which range from few to thousands of nanometers. It is also applied for multilayer deposition. The substrates range from a small microscope glass to large glass panels. The deposition rates range from one to ten nanometers per second (Reinhold *et al.*, 1991; Mercus and Foster, 1993; Navinsek and Panjan, 1993; Schulz and Schmucker, 1998).

PVD process can be employed in thin films deposition of elements, alloys and compounds. The PVD processes can be categorized in to vacuum evaporation, sputter deposition and ion planting (Mattox, 1998). Sputtering on the other hand is classified into three types. These are magnetron sputtering, radio frequency sputtering and reactive sputtering.

### 3.2.2 Vacuum Evaporation

This is a technique whereby target source is heated and the vaporized material travels to the substrate with or without little collision from gas molecules on the path. The chamber is evacuated so as to minimize contamination of the vaporant in the deposition chamber. The typical deposition pressure ranges between $10^{-5}$ to $10^{-9}$Torr. The material to be vaporized is heated at the source by passing electrical current through a tungsten wire or by use of high energy electron beam (Mattox, 1998). The substrate is placed at an appropriate distance from the target to prevent effect of radiant heat at the source. Vacuum deposition has got many applications which includes; wear resistant coating, corrosive protective coating, mirror coatings and optical interference coatings (decorative coatings and thin film deposition for research applications).

### 3.2.3 Electron Beam Evaporation Technique

Electric current is fed to the filament. Electrons in the filament escape and are focused by magnets to form a beam. Figure 3.6 illustrates a schematic diagram of electron beam evaporation technique. A filament is heated by an electric current and electrons are released. These electrons are then accelerated using electric potential of approximately 4

keV to the anode at high speed. The electric potential and a magnetic field direct the electrons to a crucible containing the target material. The electron's kinetic energy is converted to thermal energy which heats up the target material. The heat generated is very high. Once the material evaporates, it is consequently deposited on the substrates forming thin films. To measure the thickness of thin films, a quartz crystal is placed inside the chamber such that the vapour also deposit on it. The natural vibration frequency of the crystal, change with increase in layer's thickness. This allows for deposited layer's thickness to be determined.

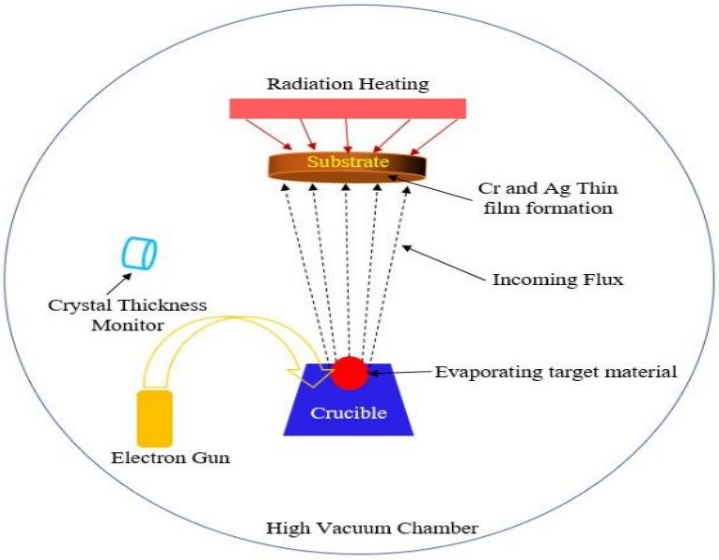


**Figure 3.6: Schematic diagram representing electron beam evaporation technique (Naseem *et al.*, 2020)**

### 3.2.4 Pulsed Laser Deposition

Most materials in their bulk forms exhibit diverse properties compared to the same materials in thin films form. This is true for chacolgenide glasses for phase change

memory application. When in the mission of searching for better materials with superior qualities for phase memory application, structural, optical and electrical study of thin films is paramount. Deposition techniques affect thin film properties.

Laser technology came to limelight in the year 1960 when Theodore H. Man constructed a ruby laser. Smith and Turner (Smith and Tuner, 1965) used the ruby laser in deposition of thin films in the year 1965. This was the genesis of pulsed Laser Deposition (PLD) technique which has since found a myriad of applications in the modern technology world. This has been attributed mainly to its special features such as high power density, coherent, narrow frequency bandwidth, high precision and resolution (Chrisey and Hubler, 1994). However, the PLD technique did not gain momentum immediately after discovery. It's development was slow in comparison to other film growth techniques until ten year later when rapid growth of this technology began (Patel,1964; Geusic *et al.*, 1966). At this juncture, lasers with superior qualities such as higher repetitive rates than the ruby lasers were developed. This made it possible for harmonious evaporation of the material target leading to deposition of stoichiometric films. PLD has been used to synthesis quantum dots (Goodwin *et al.*, 1997), nanotubes (Zhang *et al.*, 1998) and Nano powders (Geohegan *et al.*, 1999) in the recent years.

The PLD process entails directing a high power laser beam on to a target in a vacuum. PLD process is a three stage process. These stages are: vaporization of the material of the target to form a plume, transfer of the plume towards the substrate and deposition of the plume on the substrate forming a thin film. The three stages repeat many times during a

deposition run. The surface of the target absorbs the strong electromagnetic radiations and this result to evaporation of its materials. The target material is vaporized into a plasma plume of excited and energized ions. The plasma plume generated, moves to the substrate and is deposited as a thin film.

Figure 3.7 shows a schematic diagram of a PLD chamber. A pulsed laser is shown directed to a target. The laser vaporizes a little volume of target material which creates a plasma plume. This plume acts as a material flux for thin film growth. During the process, laser energy density and pulse rate are controlled. Through control of pulse rate, the film thickness can be controlled. The PLD is unique in that it retains stoichiometry of the target material. This is attributed to the high heating rates of the target by the pulsed lasers. This ensures total evaporation of the target material. Both the target and the substrate are rotated to ensure uniform films.

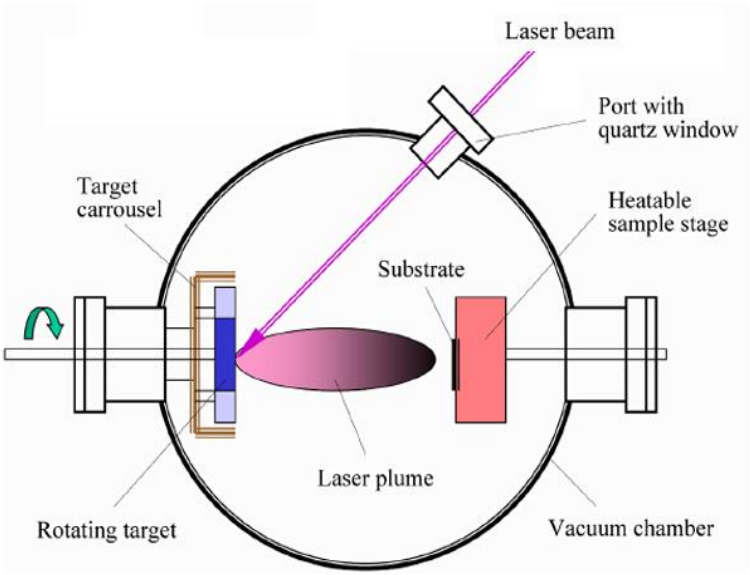


**Figure 3.7: Schematic diagram of PLD chamber (Ogugua *et al.*, 2020)**

There are different lasers used in a PLD. The laser should produce enough power to dislodge materials from the target. The power is approximately $1J/cm^2$ (Chrisey and Hubler, 1994). Different lasers are used for different materials. Generally lasers used in PLD fall in the UV range because most material's strong absorption is in this range. Pulse rates of about 100Hz are used for PLD lasers with 10Hz being used when high quality films are necessary. Some of the commonly used lasers are the solid state lasers and excimer lasers.

PLD has got various advantages over other thin film deposition techniques. These include production of a uniform film. Pulsing of the laser produces a super saturation of the evaporants from the target material. This causes a large number of nucleation cites to be formed on the substrate thus resulting to a uniform film. Secondly they have ability to produce thin films whose stoichiometry is similar to that of the target. This is the main advantage of PLD system compared to other methods. Furthermore these systems allow use of background gases which is very useful especially when dealing with oxides where oxygen is used.

Also PLD systems are equipped with a load lock which makes it possible to insert or remove samples, targets and substrates without having to vent the main chamber. It also has provision for multiple targets which allow growth of multilayer films. This technique has a disadvantage in that the large kinetic energy of some plume species causes re-sputtering and likewise defects in the substrate surface and growing film.

### 3.3 Scanning electron microscopy

This instrument is capable of measuring and analyzing structural characteristics of solid substances. It also has high resolution and can measure up to 2.5 nm. It can measure objects from three dimensions thus providing a rich wealth of information. This method is used for analysis of materials and surfaces. It involves use of highly energetic and focused electron beam. When electrons interact with the atoms at the surface layer, a signal is produced which can give information about the composition of the elements, surface topology and conductivity. During this process, electrons undergo elastic and inelastic scattering. Elastic scattering gives rise to back scattered electrons while inelastic scattering produce effects such as phonon excitation, characteristic X-ray radiation, cathodoluminescence, auger electron production and plasmon production. The signals from the sample are detected by use of suitable detectors from which a lot of information about the sample can be obtained. An electron beam of high energy emanating from a thermionic source is passed through the electromagnetic lens which focuses it to a small spot. The deflector plates deflect beam into two orthogonal directions for it to scan a rectangular portion of the sample. The signal is then amplified and displayed on the cathode ray tube. Energy dispersive X-ray spectrometry takes place when the beam of electrons removes an inner cell electron from the specimen. An electron of higher energy fills this shell and as a result energy is emitted. This is used in the analysis of sample composition.

Backscattered electrons are high energy electrons which are reflected after electron beam interacts with the sample surface through elastic scattering. Elements with high atomic

number and hence heavy, reflect the electrons more strongly compared to the light elements. The image therefore appears brighter in comparison with the low atomic number elements. Therefore the backscattered electrons can be used to differentiate between areas with different elemental composition (Goldstein *et al.,* 1981).

### 3.4 Crystallization Kinetics

Demand for high data transfer rate is increasing tremendously and therefore crystallization rate of phase materials is of paramount importance. Changing of materials to amorphous phase is a relatively faster process. Therefore, crystallization is the process which determines the rate of data transfer. To achieve high data transfer rate, there is need to consider the crystallization process. The operation speed of the PRAM devices depends mainly on the kinetics of crystallization of the amorphous phase. In phase change devices, rate of changing a material to amorphous state is faster compared to that of changing to crystalline state. Therefore research should focus on improving the crystallization time. Crystal nucleation and growth are the two processes which dominate crystallization. We can conclude that increasing the rate of nucleation and growth of crystals leads to increase in data transfer rates (Pandian, 1978).

To investigate crystallization kinetics, thermal analysis method has been applied. This method of analysis is faster and little amount of sample material is needed. In isothermal method of thermal analysis, a material is heated up to temperature higher than its phase transition temperature. On the other hand, non-isothermal method entails heating the

material at constant rates. The latter is also referred to as Kissinger analysis method. This method follows equation 3.1.

$$\ln\left[\frac{\beta}{T_P^{\,2}}\right] = -\frac{\Delta E}{K_B}\left[\frac{1}{T_P}\right] + const \qquad (3.1)$$

Where $T_p$ is the peak temperature and $\beta = \frac{dT}{dt}$ is the heating rate. A graph of $\ln\left[\frac{\beta}{T_P^{\,2}}\right]$ versus $\frac{1}{T_P}$ is a straight line whose slope yields activation energy ($\Delta E$).

### 3.5 X-Ray Diffraction (XRD)

An XRD constitute an X-ray detector, X-ray tube and a sample holder (figure 3.8). A filament in the cathode ray tube (CRT) is heated to give out electrons which are accelerated towards the target. When the target is hit by high energy electrons the inner orbital electrons are injected. The transition of these electrons from high energy levels to low energy levels leads to production of characteristic X-ray spectra. XRD is a technique mainly used to establish structural properties of elements. In this system, an electromagnetic wave whose wavelength is commensurate to the crystal lattice spacing is diffracted by a crystal. The diffraction pattern when analysed give information about the composition of the substance under investigation. A schematic representation of X-ray diffractometer is given in figure 3.8. Diffraction follows Brag law stated as equation 3.2.

$$2dsin\theta = n\lambda \qquad (3.2)$$

where d is the inter-planner spacing, θ is diffraction angle, λ is incident beam wavelength and *n* the order of diffraction.

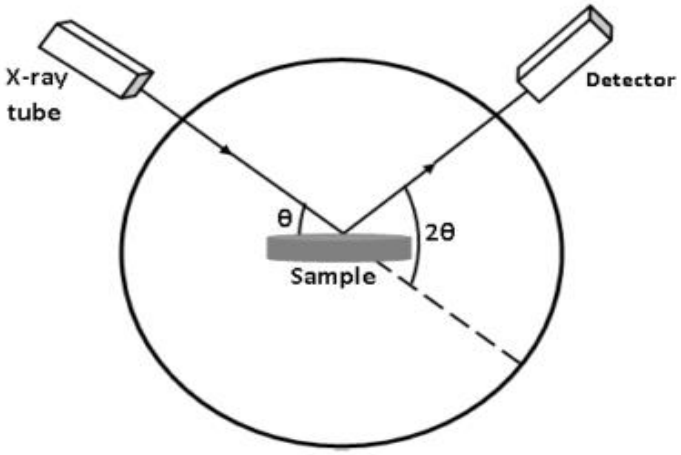


**Figure 3.8: Schematic diagram of X-ray diffractometer**

The material is bombarded by high energy X-rays resulting to diffraction of these rays by atomic lattice planes. When diffracted X-rays differ by a whole number of wavelengths on the way to the detector, they interfere constructively. The resultant XRD peaks characterize the spectrum formed. On the contrary, destructive inference gives rise to a spectrum of zero amplitude peaks. Figure 3.9 demonstrate diffraction of X-rays from two parallel atomic planes. θ is the angle of incidence while 2θ is the measured angle. Constructive interference forms XRD spectrum (Cullity, 1956).

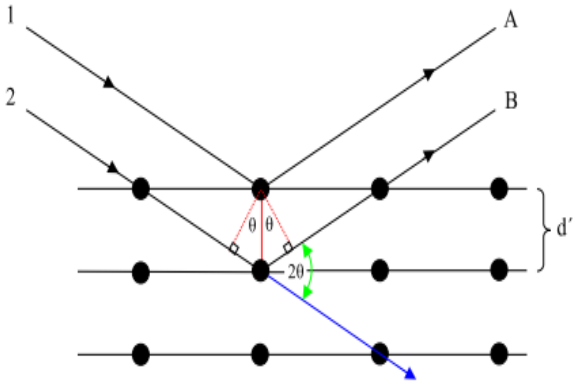


**Figure 3.9: Schematic diagram showing the principle of operation of XRD**

Equation 3.3 describes the path difference *x* which is between the incident ray 1 and 2 when they reach point A and B respectively.

$$x = 2\grave{d}sin\theta \quad (3.3)$$

For constructive interference to take place, the path difference *x* between two X-rays must be equal to $n\lambda$ where *n* is the whole number. Substituting this in equation 3.3, we get equation 3.4 (Gfroerer 2000).

$$n\lambda = 2\grave{d}sin\theta \text{ where } n = 1,2.3\ldots\ldots.. \quad (3.4)$$

Equation 3.4 shows the condition for constructive interference. It is known as Bragg's law. Different values of *n* give different values of $\grave{d}$. Equation 3.4 can be written as equation 3.5 (Gfroerer, 2000).

$$x = 2dsin\theta \quad (3.5)$$

where $d=\frac{\grave{d}}{n}$

### 3.6 Optical Characterization

Light is an electromagnetic radiation with energies ranging from 1.2 meV to 124 eV. It exhibits dual nature in that it behaves as a particle and a wave. As a particle, a photon of light which has got neither mass nor charge interacts with other particles such as electron and atoms electromagnetically. Energy and wavelength of the particle relate to Planck's constant and light speed in vacuum by equation 3.6

$$E = \frac{hc}{\lambda} \quad (3.6)$$

where *h* is Planck's constant, *c* is light speed in vacuum and λ is the wavelength. Just like waves, light undergoes diffraction, refraction and interference. The speed of light is c in vacuum but diminishes in other media. The rate at which this speed reduces is known as the refractive index (n) of that particular material. It is given by the relation 3.7.

$$n = \frac{c}{v} \tag{3.7}$$

where c is light speed in vacuum and v is light speed in a material. When light falls on a material, it is scattered, transmitted or absorbed. The interaction relies on the chemical, physical or structural properties of the material. Intensity and photon's energy plays a major role. Various excitations are produced in a material depending on the photon's energy. For instance photons in the ultraviolet and visible range of spectrum may interact with electrons in the outer shells of atoms elevating them to higher energy levels or create excitons or both. On the other hand, photons in the infrared region of the spectrum may interact with lattice and molecular vibrations and rotations to create phonons. Therefore, by choosing appropriate photon energy, different properties of materials can be investigated. Table 3.1 shows examples of excitations, their characteristics and the techniques that make use of them.

**Table 3.1: Different excitations, their characteristics and techniques that employs them**

| Excitation | Description | Characteristics | Characterization techniques |
|---|---|---|---|
| phonon | Collective lattice vibration | Neutral | Raman, infrared, photoluminescence |

| | | | |
|---|---|---|---|
| Exciton | Describes the bound state of an electron-hole pair due to their mutual coulomb attraction | Neutral, obeys Bose statistics, can bind with impurities, defects and other excitons | Photoluminescence (Szczytko *et al.*,2005), modulation reflectance(Shay and Nahory,1969; Komkov *et al.*, 2009) and transmission |
| Plasmon | Collective motion of charge carriers gas with respect to a oppositely charged rigid background | Neutral | UV-VIS, IR, Raman (Surface enhanced SE, tip enhanced TE) (Moskovits 1985) |
| Polaron | Describes the coupling of electrons or holes and longitudinal phonons | Can bind with other polarons of the same or opposite charge | Absorption (Merschjann *et al.*, 2007) |
| Polariton | Describes the coupling between excitons and phonons | | Raman (SE and TE) (Lopez-Riots, 2012) |

### 3.6.1 UV-VIS-NIR Spectrophotometer

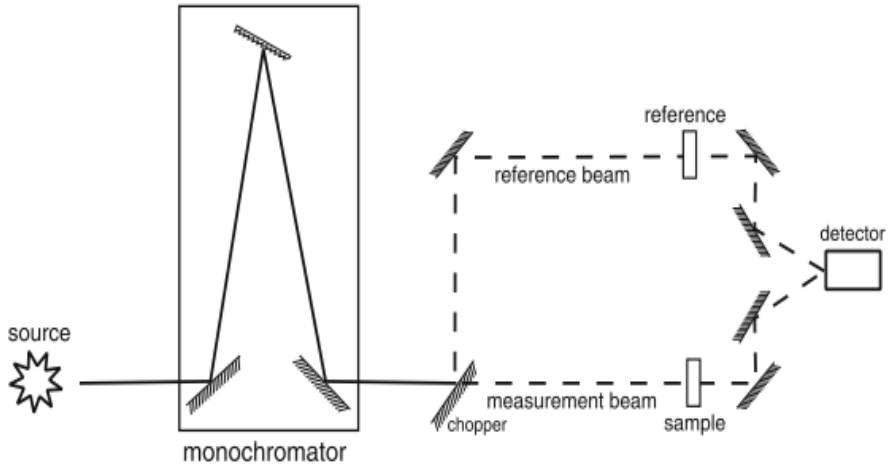


**Figure 3.10: UV-VIS-NIR Spectrophotometer**

The UV-VIS-NIR Spectrophotometer (figure 3.10) is used to determine the intensity of reflected, transmitted or absorbed light. These instruments come in a variety ranging from cheap single beam model to high-cost double beam with numerous sources of light and detectors. The typical spectrophotometer comes with more than one sources of light, diffraction grating based monochromator, sample chamber and single or many detectors.

Figure 3.10 represents a schematic representation of a two beam spectrophotometer. The instrument is capable of performing measurement on different types of samples ranging from liquid solutions, solid thin films and powders. The measurements include transmittance, reflectance and absorbance. Those spectrophotometers equipped with dual beams measure a reference sample at the same time with the sample under test.

### 3.6.1.1 Transmittance

This quantity is measured using a spectrophotometer. It entails measuring the quantity of incident light power that passes through a material under test as a function of wavelength of light. In percentage, it can be expressed as shown in equation 3.8.

$$T = \frac{PT}{PO} \times 100 \qquad (3.8)$$

where T is transmittance, PO is incident light power and PT is power of light which pass through the material sample under test. To get the system base line, a known sample is measured. To obtain the quantity of the dark current, the path of light is blocked using an opaque object. These measurements are done at the beginning of every measurement because these quantities may change with time during use of the instrument. In case of bulk samples, baseline is collected by doing measurement without a sample. For solvents or samples with a substrate, a clean substrate or pure solvents are used to get the baseline.

On measuring the sample spectrum, the detector's dark current is subtracted. This raw spectrum is then divided by the baseline from which the detector dark current has been subtracted also as shown in equation 3.9.

$$T = \frac{To - D}{B - D} \tag{3.9}$$

where T is the absolute transmittance, To is the raw spectrum, B is the baseline and D the detector's dark current.

This method takes care of errors due to components on the path of the spectrophotometer, substrates and solvents. It does not cater for errors due to fluctuations of the source and other systematic errors. To mitigate the errors, instruments are equipped with dual beams. These are the sample beam and reference beam. The spectrum measured is as a result of a ratio of the two beams measured simultaneously where powers of light of sample beam is divided by powers of light of reference beam. This is illustrated in equation 3.10.

$$T = \frac{To - D}{B - D} = \frac{\frac{PS}{PR} - \frac{DS}{DR}}{\frac{BS}{BR} - \frac{DS}{DR}} \tag{3.10}$$

where PS is the power from the sample beam, PR is the power from the reference beam, DS is the detector dark current of the sample beam, DR is the detector dark current due to reference beam, BS is the baseline power due to sample beam and BR is the baseline power. A dual beam spectrophotometer has got advantage over the single beam in that it is capable of compensating for short term variations of the intensities of light sources and

efficiencies of components common to both beams. In most times there is change of light intensity and changes of detector efficiencies with change in temperature.

#### 3.6.1.2 Reflectance

The UV-VIS-NIR spectrophotometer is also used in measurement of sample reflectance. In this measurement, the beam is modified in such a way that light that falls on the detector is the one reflected by the sample. The two modes of measuring reflectance are diffuse and specular. In diffuse reflectance light reflected in all directions from the sample is collected, while in specular reflectance, only light reflected at an angle similar to the incidence angle is collected.

Specular reflectance is used when dealing with measurements of highly polished surfaces. A standard mirror of known reflectance is used to collect the base line without any other sample on the beams. To determine the contribution of the substrate to the spectrum, a clean substrate is used to measure the reflectance. The measurement is repeated with a sample on the substrate. This way we can quantify the substrate contribution to the final spectrum.

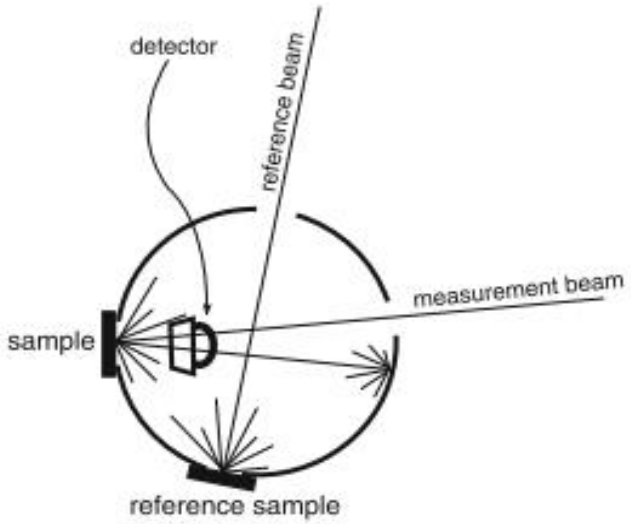


**Figure 3.11: Schematic diagram representing diffuse reflectance based on integrating sphere**

Diffuse reflectance (figure 3.11) is used when dealing with rough surfaces. Reflection from these surfaces is scattered in all directions and not very much related to the angle of incidence of light. This method is used for powder samples, nanostructured materials and ceramics. The method is also used for reflective surfaces which distort incident beam for instance the curved mirrors. A special designed mirror or integrating sphere is used to collect the reflected light. The sample reflectance is then compared with a standard known diffuse reflectance. Integrating spheres are coated internally with a high reflective coating. The disadvantage of this sphere is the high loss which makes measurement of low reflectance challenging.

### 3.6.2 Kubelka-Munk Equation

Generally two types of reflections take place when an infrared radiation is focused on a solid surface. There is a radiation which reflects directly off the sample surface which obeys the laws of reflection. The second type of radiation is diffuse which emerges from the sample in all directions. An optical system corrects the scattered diffuse radiation and directs it to an infrared detector from where optical properties are deduced. This theory was determined by Kubelka and Munk in the year 1931. The model correlates concentration of the sample to the measured infrared intensity. The function is given in equation 3.11.

$$F(R)=\frac{(1-R)^2}{2R}=\frac{K}{S} \tag{3.11}$$

where R represents absolute reflectance, K molar absorption and S scattering coefficient.

The sample is ground to uniform fine powder particles to ensure quality measurements given that the scattering coefficient is a function of particle size.

### 3.7 Energy dispersive X-ray spectroscopy

Energy dispersive X-ray spectroscopy (EDS) is a technique used for analysis of elemental composition of a sample. The analysis involves the interaction of electromagnetic radiations and the sample material. The resulting X-rays emitted are analysed to give information about the sample elemental composition. This technique works on the principle that each element has an atomic structure which is unique which makes it possible for each element to emit unique X-rays. The X-rays make the atomic structure of

the element to be uniquely identified from others. A high energy beam of X-rays is directed to a sample under test in order to emit characteristic X-rays. An atom has got electrons at ground state in the inner orbits when at rest. The high energy X-ray beam directed onto a sample may eject an electron which is at ground state in the inner shell. An electron from a higher energy outer shell may move to fill the hole in the inner shell thus emitting energy in form of characteristic X-rays. The energy of the X-rays can be measured to give details of the constituent of the sample. The EDS systems can exist as stand-alone and others are incorporated in TEM and Scanning Electron Microscope (SEM).

### 3.8 Photoluminescence

Luminescent materials are those that emit electromagnetic waves in the ultraviolet, visible or infrared regions of the electromagnetic spectrum when energy is incident on them. Luminescence materials are classified in accordance to the excitation method. Luminescence excited by electric current is referred to as electroluminescence and the one caused by bombardment of high energy electrons is known as cathodoluminescence. The one due to excitation of electrons after absorption of a photon is known as photoluminescence.

Luminescence due to thermal energy on a semiconductor material is called thermoluminescence (Pillai, 2010; Sharma, *et al.*, 2011). Our focus on this study is photoluminescence. Photoluminescence can be classified as intrinsic and extrinsic. Intrinsic photoluminescence is due to inherent defects in the crystal structure (Boggs and

Krinsley, 2006). On the other hand, extrinsic photoluminescence is caused by impurities introduced in the crystal structure.

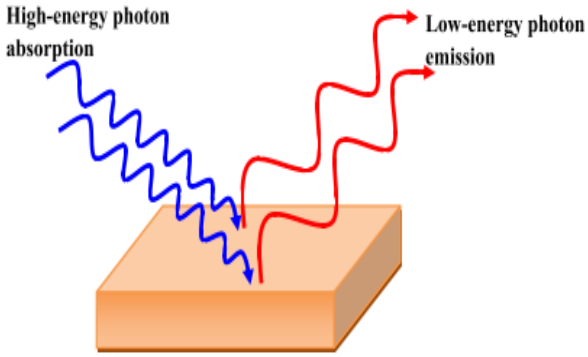


**Figure 3.12: Schematic diagram illustrating photoluminescence**

Figure 3.12 shows a semiconductor material absorbing a high energy photon and subsequently emitting a low energy photon in a photoluminescence process. Photoluminescence can further be divided into two depending on the duration of the decay lifetime. These categories are fluorescence and phosphorescence. Emission of light when a material is subjected to excitation radiation is known as fluorescence. On the other hand the light emission as sensed by human eye after excitation is withdrawn is referred to as phosphorescence. In fluorescence materials, light emission ceases immediately the excitation is withdrawn (Ball and Moore, 1979). The decay times for fluorescence materials are less than 10ns, whereas for phosphorescence it is above 100ns. Fluorescence process is independent of temperature while phosphorescence is temperature dependent. Additionally phosphorescence is due to shallowly trapped charged carriers (Chen and Mckeever, 1997).

In PL, an electron is excited first from its ground state by absorbing a photon of light to a higher energy state. The incident monochromatic beam of photon is partly absorbed, reflected and transmitted by the material. The excited electrons move to conduction band or to defect states within the band gap. The particle drops back to ground state and emits a photon. With excited light held constant, different frequencies of emitted light are measured and this constitutes emission spectrum (Valew, 2002; Lakuwicz, 1983; Pesce *et al*., 1971).

Figure 3.13 illustrates fluorescence and phosphorescence types of emission. In figure 3.13(a), the electron is excited from ground state (gs) to excited state (es) after absorption of light energy. Fluorescence takes place during the electron transition from es to gs through the path indicated 2. In figure 3.13(b), the electron is excited from gs to es through absorption of light energy. However the electron follows transition 3 to a metastable state (ms) which may be due to defects. This electron will remain in this state until it gains enough energy to es through path 4. It will then relax to ground state displaying phosphorescence emission.

Photoluminescence refers to the spontaneous emission of light from a material when optically excited. One chooses the excitation energy to probe different parts of a material. The emission spectra produced have many useful applications such as discerning of impurity levels, quality of surfaces and interfaces and to gauge alloy disorders. It is a fast technique which requires very minimal manipulation of the material under test.

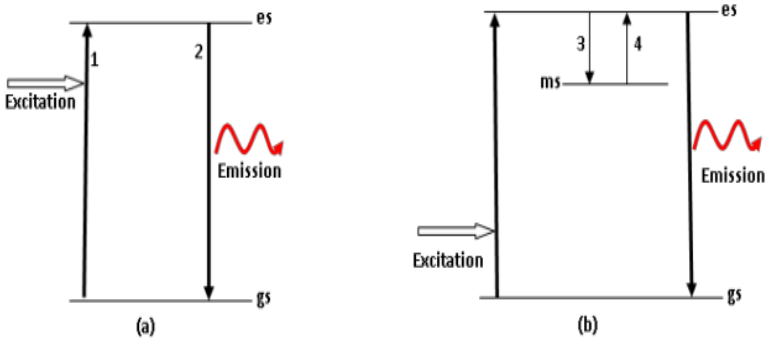


**Figure 3.13: Schematic diagrams representing (a) fluorescence and (b) phosphorescence emissions**

Electronic excitations occur in a sample material when a light photon of sufficient magnitude falls on it. These excitations take place when the photons of energy are absorbed by the material. The excitations finally relax and electrons fall to lower energy state. The emitted light which accompanies relaxation is referred to as the photoluminescence (PL). The PL spectrum gives information of the transition energy which can be applied to determine the energy level. PL intensity provides information about the rates of recombination which results from radiations and non-radiations. PL is a simple, versatile technique and does not destroy the sample. Despite the advantages, it has a shortcoming in that the sample under test must emit light. The choice of excitation energy is paramount. Different excitation energies probe different regions. Lasers are usually employed as sources of excitations due to the fact that they are monochromatic and readily focused. HeNe and diode laser are mostly used for basic measurements. Optical transitions give knowledge about energy level and structure of material. A state which radiates gives a unique peak in a PL spectrum. The PL spectrum can be used to identify discrete states and also to determine composition of a semiconductor alloy.

### 3.9 Differential Scanning Calorimetry

Differential Scanning Calorimetry (DSC) technique was applied for thermal studies (Kasap *et al.,* 1999). DSC operates through monitoring heat effects as a result of chemical reactions and phase transitions. It records the difference in flow of heat through a sample and a reference as a function of temperature. Activation energy of crystallization is determined from heating rate dependence of peak crystallization temperature $T_p$. Glass activation energy is energy absorbed by atoms to move from one metastable state to another in the glassy region (Imran *et al.,* 2001). The energy is used in motion of molecules and rearrangement of atoms within the glass transition.

### 3.10 Activation Energy

Activation energy of crystallization is derived by employing modified Kissinger equation (Matusita and Sakka 1979; Macfarlane *et al.,* 1984; Suri *et al.,* 2006). Phase transition temperature of a material is dependent on molecular weight, bond energy, type of structure and co-ordination number (Rabinal *et al.,* 1995). The amorphous glassy solid state undergoes slow relaxation kinetics which is attributed to relatively high viscosity. This hinders the local arrangement of the bonds and displacement of atoms. The thermal relaxation depends on the heat treatment of the material and is faster at values near the glass transition temperature. Therefore the glass transition temperature is associated with the structural rearrangement which needs activation energy (Rabinal *et al.,* 1995; Mehta and Kumar, 2005).

### 3.11 X-ray Photoelectron Spectroscopy

The X-ray photoelectron spectroscopy (XPS) technique involves irradiating a sample material with mono energetic soft X-rays in a vacuum environment and analyzing the emitted electrons. Obtained spectrum displays the electrons emitted in a small fixed energy interval versus kinetic energy. Photons from X-rays act on the atoms on the sample's surface by photoelectric effect where electrons with enough energy to overcome work function escape. The kinetic energy of emitted electrons is estimated by equation 3. 12.

$$E_k = h\nu - E_B - \Phi \qquad (3.12)$$

where $h\nu$ represents energy of incident photon, $E_B$ the binding energy of the orbital from which electron originates and $\Phi$ the work function of the material. Only electrons whose value of binding energy is less than photon energy get emitted. The photoelectrons which reach sample surface without collision form defined core peaks in the spectra. The elastically scattered electrons form background at higher binding energy than peaks on which photoelectron peaks build.

The depth of the sample from which electrons can escape without being scattered elastically is in the order of 10-50Å, hence X-ray spectroscopy is a surface-sensitive technique. The depth of sampling is calculated from the average distance travelled by electron before inelastically colliding and emission angle to the surface. This distance is referred to as mean free path. The sample depth is given by equation 3.13.

$$d = \lambda \cos\alpha \qquad (3.13)$$

Due to surface sensitivity of XPS technique, slight contamination of the sample surface may have adverse effects on the spectra. Therefore the experiments should be carried out in a contaminant free environment. The emitted photoelectron's binding energies are characteristic of the elements irradiated. These energies give information about the chemical states of the elements. Identification of elements is possible since no two elements have same binding energy. Electronic structure of elements changes when they bond to form compounds. This brings shift in binding energy, commonly referred to as chemical shift.

### 3.11.1 Functions of Different Parts of XPS

#### 3.11.1.1 Spectrometer

A spectrometer consists of sample analysis chamber, X-ray excitation source, electron energy analyser and a detector. In addition it also has sample insertion probe, ion etching gun, sample treatment chamber and quadrupole mass spectrometer for residual gas analysis.

#### 3.11.1.2 Vacuum System

Due to surface sensitivity of XPS, ultra-high vacuum environment is paramount. Contamination of surface prevents the signal from reaching the sample's surface. In this study, two liquid nitrogen rotary pumps were used. One pump is used for roughing and the other as a backup for the main ultra-high vacuum pump. One of the diffusion pumps is used to evacuate the analysis chamber and the other to reduce pressure in the sample treatment chamber.

### 3.11.1.3 Sample Insertion Lock and Probe

A probe is long and highly polished. It also has cooling and heating facilities. To introduce samples into the spectrometer, they are attached to the end of the probe. A probe is introduced to the analysis chamber by an insertion lock after which it is pumped out by rotary pumps. The sample probe is inserted such that the sample surface is in line with ion etching gun for cleaning the surface. After cleaning the sample surface, it is aligned with X-ray gun for analysis. The probe can rotate such that angular dependence analysis can be performed. Figure 3.14 represents a schematic diagram of a spectrometer.

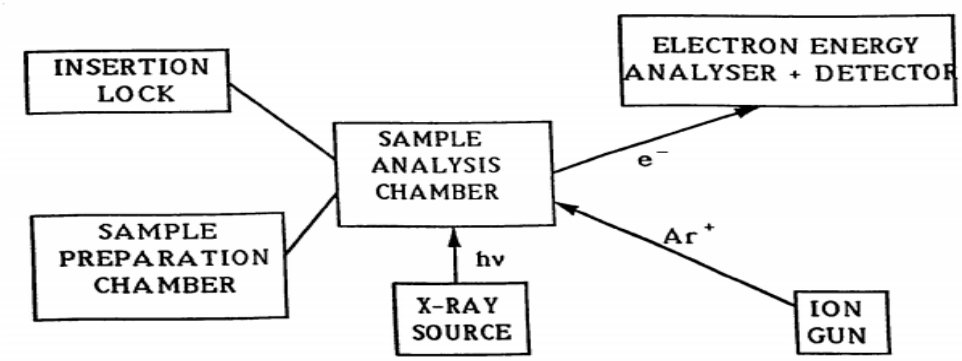


**Figure 3.14: A schematic diagram of spectrometer**

# CHAPTER FOUR

# MATERIALS AND METHODS

## 4.1 Introduction

This chapter outlines the experimental techniques employed for preparation, characterization and measurements of $In_2Se_3$: X% Bi bulk and the thin films samples. The powder samples were synthesized using melt-quenching technique. Pulsed laser deposition (PLD) technique was used for thin film preparation. The X-ray photoelectron spectroscopy (XPS) was applied in determination of chemical composition of In-Se-Bi thin films. The phase of both the bulk and thin film samples was confirmed by use of X-ray diffraction (XRD) technique. Actual constituent of the samples was determined using energy dispersive spectroscopy (EDS) technique. Investigation of the sample's surface morphology was carried out by Field Emission Scanning microscopy (FE-SEM). Resistivity of thin film samples was measured using four point probe method.

## 4.2 Synthesis of In-Se-Bi alloys

Pure selenium, bismuth and indium were obtained from sigma Aldrich Company (99.999% pure). The substances were weighed with an electronic balance according to their atomic percentages. After weighing, they were mixed before sealing them in quartz ampoules in vacuum. Indium and selenium were maintained at the ratio 2:3 for all measurements. Bismuth was added in 0, 2, 4, 6, 8 and 10 % to $In_2Se_3$ obtained. Table 4.1 and 4.2 show how the various quantities were determined for the alloy formation.

**Table 4.1: Stoichiometric weights of different samples of In and Se alloy for synthesis 20g of the alloy.**

| Alloy | Element | % | Atomic weight (a.m.u) | actual weight(g) |
|---|---|---|---|---|
| $In_2Se_3$ | In | 40 | 114.82 | 9.8448 |
| | Se | 60 | 78.96 | 10.1552 |

**Table 4.2: Stoichiometric weights of different samples of $In_2Se_3$: X% Bi alloy for synthesis of 20g of the alloy.**

| Alloy | Element | % of Bismuth in $In_2Se_3$ | Actual weight (g) |
|---|---|---|---|
| $In_2Se_3Bi_{(x=0)}$ | $In_2Se_3$ | 0 | 20.00 |
| $In_2Se_3Bi_{(x=0.02)}$ | Bi | 2 | 0.86 |
| $In_2Se_3Bi_{(x=0.04)}$ | Bi | 4 | 1.64 |
| $In_2Se_3Bi_{(x=0.06)}$ | Bi | 6 | 2.37 |
| $In_2Se_3Bi_{(x=0.08)}$ | Bi | 8 | 3.04 |
| $In_2Se_3Bi_{(x=0.1)}$ | Bi | 10 | 3.66 |

### 4.3 Melt-quenching technique

Alloys used in this research were prepared by melt-quenching technique. They fall in a group known as amorphous semiconductors and have myriad of applications in the electronic world (Agarwal *et al.*, 1991; Mehta *et al.*, 2005; Ates *et al.*, 2008). The most convenient and commonly used technique for alloy formation is melt-quenching. After mixing the samples, they were put in a quartz tube and sealed before being heated in an electric furnace to a temperature of 1200$^{o}$C. The ampoules were heated for 20 hours and were rocked frequently to make the melt homogeneous during the heating process. Melting was carried out in an electric furnace shown in figure 4.1.


**Figure 4.1: Furnace used for melt quenching at college of Science, Engineering and Technology, Department of Physics of the University of South Africa (UNISA) in Johannesburg, South Africa.**

During quenching, the liquid material does not have the conditions for formation of crystals. The rapid cooling of the melts makes it unfavorable for nucleation and growth which cause crystallization. The quenching was done in liquid nitrogen in order to obtain glassy alloys. After quenching, the bulky material was separated from quartz ampoules by breaking it. The resulting alloys were crushed into fine powder using mortar and pestle. XRD technique was used to verify the glassy nature of the alloy.

### 4.4 Thin film deposition of In-Se-Bi

PLD technique was utilized to deposit thin films. The targets were the powder of In-Se-Bi alloy and glass substrates were used. Before deposition the substrate surfaces were cleaned. This is because thin films readily adhere to clean surfaces. Contaminated surfaces by grease or other foreign impurities can make thin films to crack or peel. The following procedure was followed during cleaning of substrates

1) Soaked in solution of detergent

2) Ultrasonically agitated in distilled water for ten minutes.

3) Cleaned with acetone for ten minutes ultrasonically

4) Rinsed with distilled water

5) Cleaned with ethanol for 10 minutes ultrasonically

6) Vapour dried for about 30 minutes

PLD is a simple deposition technique that consists of a target and substrate holders enclosed in a vacuum. Target material is vaporized using a high power laser and then

deposited on the substrate. This method has over the years posed advantages such as congruent evaporation, flexibility, fast response and high speed of plume. The deposition parameters were: - laser energy 35 mJ, laser wavelength 266 nm, distance from target to substrate 4.5 cm, laser repetition rate of 10Hz and argon pressure of 50 mtorr. KrF-excimer laser was used for irradiation by focusing a beam such that a fluence of 2 J/cm$^2$ falls on the target. The target was rotated and the laser focus moved across it in order to achieve a homogeneous film. The thin films deposition was carried out at the Department of Physics, University of Free State, South Africa.

**4.5 Photoluminescence measurements**

Photoluminescence studies were performed with aid of Horiba Jobin Yvon Flourog 3 photoluminescence spectrometer, at the college of Science, Engineering and Technology in the Department of Physics of the University of South Africa (UNISA) in Johannesburg. The material sample under test was excited optically and therefore no electrical contacts and junctions were required. The emitted photon energies represent different energy states which are produced by defects or impurities incorporated in the crystal lattice. Consequently a PL spectrum gives information in relation to nature of defects in a material and type of impurities present.

In order to measure an excitation spectrum, the sum of light emitted at all frequencies as a function of monochromatic incident light is recorded. The source of excitation for a PL system is either a laser beam or UV light. Both sources were used in the course of this work. In this study, spectra were measured by placing an excitation source at 90$^o$ to the

detector. The excitation radiation is from xenon lamp and wavelength was varied. A photomultiplier tube (PMT) and a lock in amplifier were used as a detector.

The detector gives luminescence emission spectrum at the output. This spectrum represents the luminescence intensity over a range of wavelengths at fixed excitation wavelength. Figure 4.2 represents a schematic diagram of a PL system.

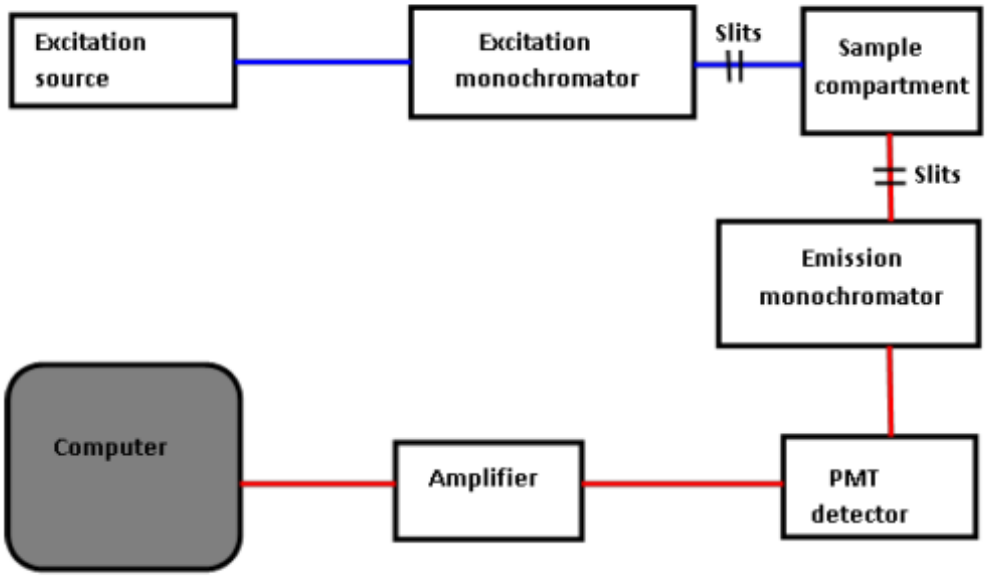


**Figure 4.2: Schematic representation of a PL system**

One monochromator selects the excitation wavelength and luminescence is shown through a second monchromator which is placed at $90^{o}$ to the incident light in order to reduce the intensity of scattered light reaching the detector.

### 4.6 Field emissions scanning electron microscopy

Morphological studies of the samples were carried out using Field emissions scanning electron microscope (FE-SEM). The technique typically operates by bombarding the sample surface with focused beam of high energy electrons. These electrons interact with sample material's atoms to produce different signals which are detected. The signals give details concerning the sample's surface which include external texture, structure, orientation and chemical composition.

High energy beam of electron strike the sample and gives off secondary electrons from the sample surface. These electrons are then collected by a secondary detector which converts them into a voltage. This voltage is first amplified before being passed on to the grid of the cathode ray tube causing the spot of light intensity to change. The image is composed of many spots of light of varying intensity which gives the topography of the sample. The narrow electron beam of SEM makes its images to have a wide field giving a three dimensional appearance. This is very crucial for the analysis of structural characteristics of a sample surface.

A schematic diagram of SEM is shown in figure 4.3. Back scattered and secondary electrons give signals which are used in the surface imaging. Characteristic X-rays are used to analyze the elemental composition of the sample. Electron beam can also produce cathodoluminescence which can be analyzed to give cathodoluminescence spectra (Poelman and Smet, 2014; Smet *et al.*, 2013). These signals are described in details in an earlier work (Egerton, 2005).

Samples of the right size are put in a specimen chamber where they are mounted on a specimen stub. Metals sample require only cleaning and mounting on the stub. Nonconductive samples charge when being scanned. This happens in the secondary electron imaging mode and can cause faults in the SEM. To prevent this, the samples are coated with a very thin electrically conducting film especially gold (Ardenne, 1937).

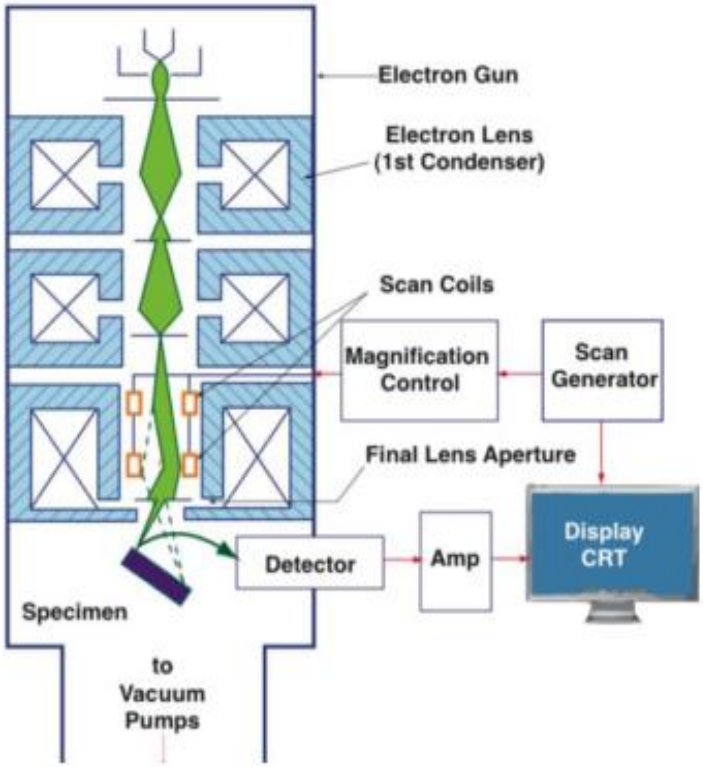


**Figure 4.3: Schematic diagram representing scanning electron microscope (Goldstein *et al.*, 2003)**

### 4.7 Electrical properties

The I-V characteristic of thin films was studied with the help of current-voltage measurement system at room temperature. Measured data was retrieved from a computer

interfaced with Keithley 237 source meter. Current-voltage (I-V) measurements were performed to determine the resistivity of various In-Se-Bi samples. In order to perform the I-V characterization, an aluminium box which is shielded was used to hold the samples in order to protect them from electrical interferences. The aluminium box has a connector to interface the sample with keithley source meter. When voltage is applied, current flows through the In-Se-Bi sample. The current which flows through the sample in absence of any irradiation is known as the dark current. The experiment was conducted at room temperature and on a vibration free table.

The voltage was varied between -10 to 10V. The resistivity (ρ) of the films is related to thickness ω, voltage (V) and current (I) by equation 4.1 (Smits, 1958).

$$\rho = \frac{V\pi}{I\ in\ 2}\omega \tag{4.1}$$

From the slope of current-voltage curve, resistivity was evaluated.

### 4.8 Optical properties

Optical characterizations were carried out by use of UV-Visible spectrophotometer (1050 LAMBDA) shown in figure 4.4. The reflectance, transmittance and absorbance of the samples were measured in the wavelength range of 250-2500nm. These measurements were performed at room temperature. The data obtained was used to determine the optical properties among them being optical band gap ($E_g^{opt}$) as well as the thickness of deposited thin films. The transmission spectrum was simulated using scout software to determine the film thickness.

There is no material which is completely transparent in all optical frequencies. There is always some region of absorption. When light is shone on a thin film, some of its energy is absorbed, some reflected and the rest transmitted. For bulk glassy alloys, absorption is used to study their optical properties. However, transmission is applied in the study of optical properties of thin films.

Optical characteristics of amorphous thin films differ widely with the crystalline counterparts. This is attributed by the fact that amorphous materials have got a short range order. They also have high density of defects which arise from the broken bonds.

**Figure 4.4: UV-Visible Spectrophotometer (1050 LAMBDA) at College of Science, Engineering and Technology, Department of Physics of the University of South Africa (UNISA) in Johannesburg, South Africa**

### 4.8.1 Band gap determination

The diffuse reflectance spectrum was employed in the band gap determination. The spectrum was transformed by Kubelka-Munk function equation 3.11 which can be rewritten as equation 4.2.

$$F(R) = \frac{(1-R)^2}{2R} \tag{4.2}$$

where F(R) represents reflectance factor which is transformed from reflectance R, according to Kubelka-Munk. To obtain the value of R, the system's background obtained using $Ba_2SO_4$ is subtracted from reflectance of the sample (Morale *et al.*, 2007). To obtain the band gap energy, the Tauc's relation is restructured using Kubelka-Munk, to get equation 4.3

$$[F(R)h\nu]^n=C(h\nu-E_g) \quad (4.3)$$

where hν denotes the photon energy and C is a proportionality constant (Morale *et al.*, 2007). A graph of $[F(R)h\nu]^n$ versus hν was plotted. A tangent was then fitted at the point of inflection. The band gap of the material was determined at the point where the tangent intersected the hν (Davis and Mott, 1970). The samples had a direct band gap and therefore n was equal to $\frac{1}{2}$.

**4.9 X-ray diffraction**

X-ray diffraction (XRD) is the most commonly applied method to characterize the crystalline structure of materials. The bulk samples were crushed to fine powder and XRD measurements done to ascertain whether they are in amorphous or crystalline state. The XRD pattern was taken using Rigaku smart lab X-ray diffractomer (radiation used was Cu-Kα, λ=1.540598 Å, 40KV and 25mA) (figure 4.5). Data acquisition was made in $2\theta$ range from $5^o$ to $90^o$ with step size of $0.05^o$. XRD analysis was also performed on the as-deposited and annealed thin films to check whether they were amorphous or crystalline.


**Figure 4.5: X-ray diffractometer (Rigaku smartlab)**

### 4.10 Crystallization kinetics

In this study, non-isothermal calorimetric studies were applied at different rates of heating to evaluate the kinetic parameters. DSC technique was used for thermal analysis from which thermal parameters were acquired. The study was carried out using DSC plus from Rheometric scientific company, UK. It has a temperature precision of ±0.1K and error of approximately ±1K for the measured values. This technique monitors the effects of heat as a result of phase transitions and chemical reactions with respect to temperature. The difference in the flow of heat in the sample and a reference is recorded as a function of temperature. Calorimetric studies were done on $In_2Se_3$: X% Bi bulk samples under non-isothermal conditions at heating rates of 5, 10, 15, 20 and 25 K/min. The calorimetric equipment was calibrated with standard materials initially before placing 20 mg of the

sample in aluminium pans for scan at constant heating rate. This was repeated for all heating rates. The runs were done in nitrogen gas atmosphere to prevent oxidation.

### 4.11 X-ray Photoelectron Spectroscopy

PHI 5000 Versa probe X-ray Photoelectron Spectroscopy (XPS) model was used in this research. The sample was irradiated by photons of known energy, which gave rise to the photoelectric effect. A fraction of electrons generated close to the surface left the sample into the vacuum under the analysers slit of the spectrometer, which was capable of measuring the electron current which corresponds to the number of electrons per unit time, as a function of their energy. Intensities versus energy plots were realized and they denote the XPS spectrum.

The energy of the emitted electrons was analyzed. The binding energy of electron is a specific characteristic which identifies an electron in relation to parent electron and atomic energy level. Each element has specific XPS peaks at particular binding energy. This way the elements in a sample were identified.

# CHAPTER FIVE

# RESULTS AND DISCUSSION

## 5.1 Introduction

This chapter outlines the findings for various experiments and discussion of the results. Electrical, optical, structural and morphological characteristics of both bulk and thin films of the synthesized/deposited samples have been reported and discussed. Photoluminescence, reflectance and transmittance spectra are represented. From XRD data, crystalline and amorphous phases of the sample under test have been identified. SEM images show the surface morphology of the samples. Elemental mapping and chemical state of elements are exhibited from EDS and XPS measurements, respectively. Electrical resistivity values were obtained using four point probe method.

## 5.2 Photoluminescence measurements

Photoluminescence measurements were carried out for powder samples as well as thin films. These measurements were done to both as-deposited and annealed samples.

### 5.2.1 The PL spectra of as –deposited powder samples of $In_2Se_3$: X% Bi

The PL spectra of the as-deposited powder samples of $In_2Se_3$: X% Bi is shown in figure 5.1. Samples were excited at 380nm and respective emissions observed in the wavelength range of 370 nm to 600 nm at room temperature.

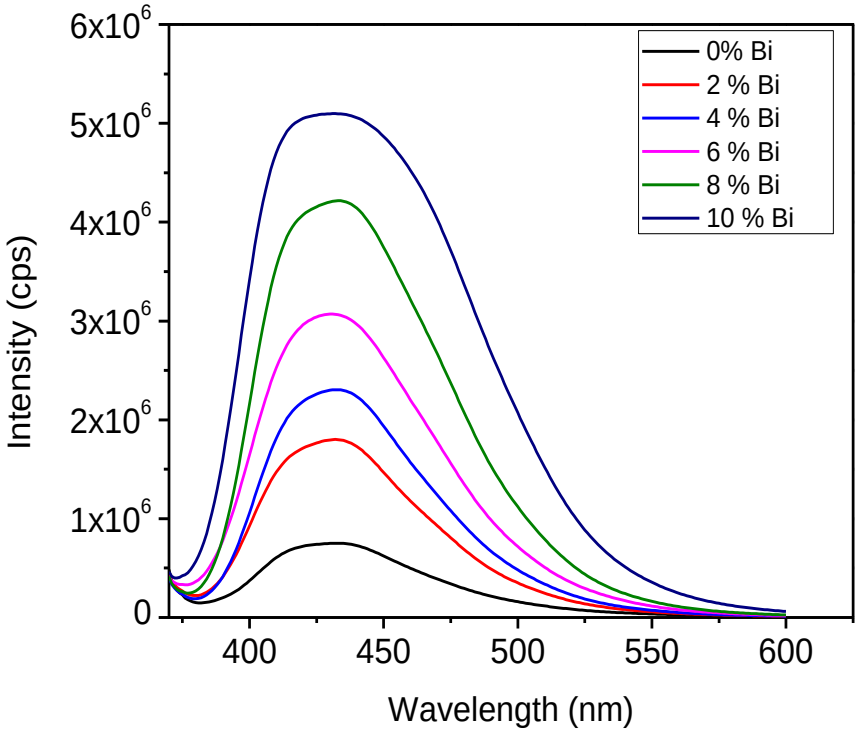


**Figure 5.1: The PL emission spectra of as-deposited powder of $In_2Se_3$: X% Bi**

The figures 5.1 represent the photoluminescence spectra of the as synthesized powder samples of $In_2Se_3$: X% Bi alloy. The figure clearly depict there is increase in intensity as percentage bismuth increases. The significantly higher PL intensity of the samples with high percentage of bismuth compared to those with low bismuth percentage suggests higher PL efficiency. Another observation is a shift of peak position towards lower wavelength with increase in bismuth content. The peak intensity and the corresponding wavelength where the luminescence intensity is maximum are listed in table 5.1.

**Table 5.1: Effect of variation of percentage bismuth on the wavelength for maximum intensity and the emission intensity**

| No. | %Bismuth | Emission peak wavelength λ (nm) | Peak Intensity(cps) |
|---|---|---|---|
| 1 | 0 | 433.62 | 752860.47 |
| 2 | 2 | 432.71 | 1799938.56 |
| 3 | 4 | 431.51 | 2304683.23 |
| 4 | 6 | 430.19 | 3066561.99 |
| 5 | 8 | 428.98 | 4222419.44 |
| 6 | 10 | 426.92 | 5104587.66 |

Table 5.1 shows the effect of the variation of bismuth percentage on wavelength for maximum intensity and the emission intensity. It is observed that the wavelength for maximum intensity decreases while the intensity of the emission spectra of In-Se-Bi samples increases with increase in percentage of Bismuth respectively. This is graphically illustrated by figures 5.2(a) and (b) respectively.

The emission peaks shifts towards the higher energy region with increase in bismuth concentration as illustrated in figure 5.2(a). The peak intensity increases with increase in bismuth percentage as demonstrated in figure 5.2(b). This may be as a result of increase in emission states that increase with increase in bismuth percentage. The photoluminescence spectra of the sample exhibit one peak. A blue shift occurs as the wavelength reduces from 433.62 nm to 426.92 nm. The existence of emission peak is due to band energy emission of $In_2Se_3$: X% Bi alloy.

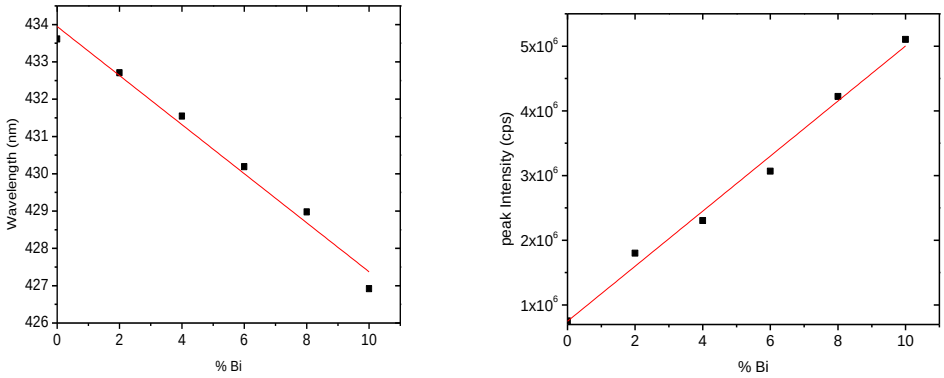


(a) (b)

**Figure 5.2: Illustration of variation of emission peak position and peak intensity with bismuth percentage, figures (a) and (b) respectively for as-deposited powder samples**

### 5.2.2 Photoluminescence spectra of the annealed powder samples of $In_2Se_3$: X% Bi alloy.

Figure 5.3 represent the photoluminescence spectra of the annealed powder samples of $In_2Se_3$: X% Bi alloy. The peak intensity is higher for these samples compared to the as-deposited samples (see figure 5. 1). This demonstrates an enhancement in PL intensity with thermal annealing for $In_2Se_3$: X% Bi alloy. This may be attributed to increasing crystallinity and decreasing structural disorder.

Peak emission values for samples with different percentages of bismuth are tabulated in table 5.2. From table 5.2 it is evident that the emissions peaks shifts towards the higher energy region with increase in bismuth concentration as illustrated in figure 5.4. The

noted enhancement in PL intensity after annealing at 500$^{o}$C can also be attributed to improvement in structure due to elimination of non-radiative defects.

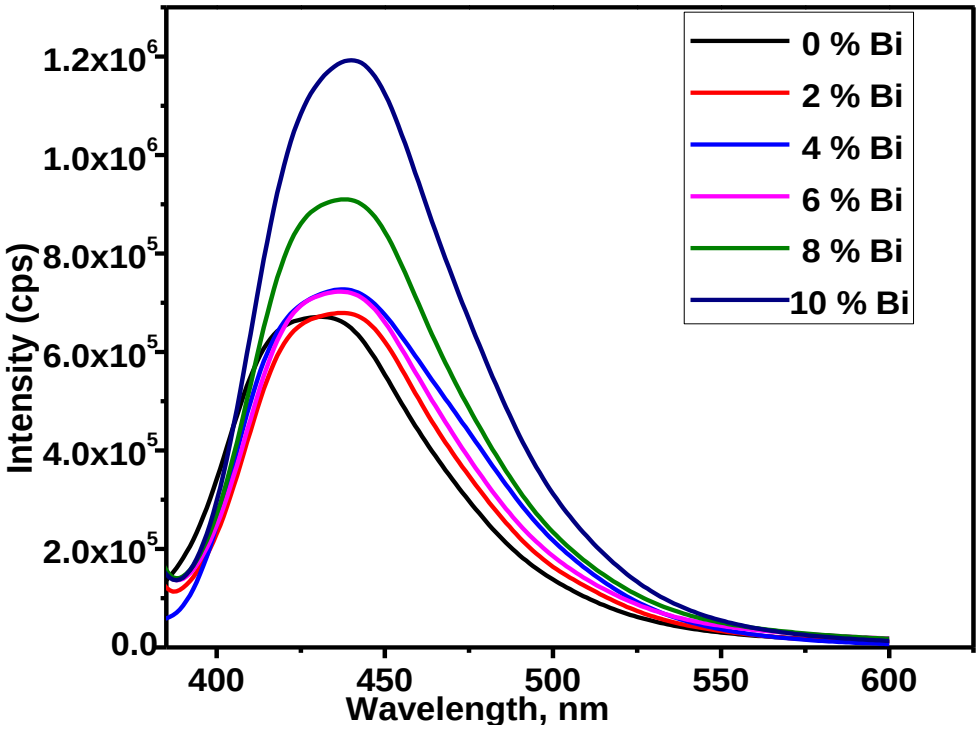


**Figure 5.3: Photoluminescence spectra of the annealed powder samples of $In_2Se_3$: X% Bi**

**Table 5.2: Emission peak position for annealed samples with various Bismuth percentage**

| Percentage Bismuth | 0 | 2 | 4 | 6 | 8 | 10 |
|---|---|---|---|---|---|---|
| Emission peaks position wavelength λ | 431.74 | 431.14 | 430.84 | 430.74 | 430.56 | 430.18 |

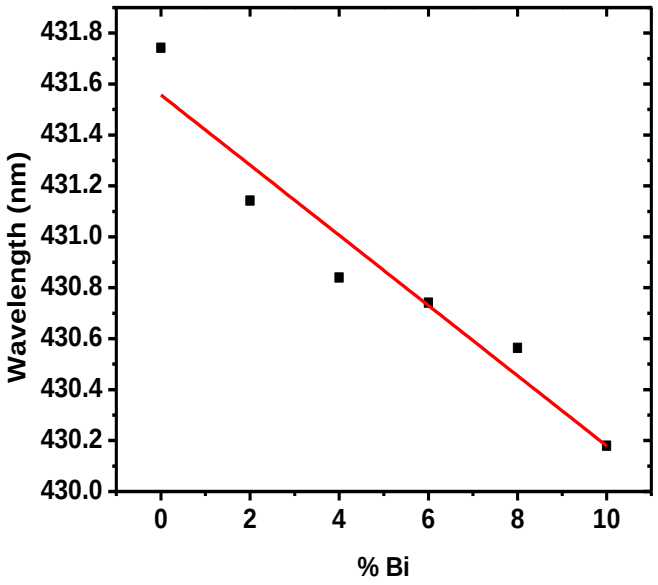


**Figure 5.4: Effect of variation of percentage bismuth on emission peak position**

Values from Table 5.2 were used to plot figure 5.4. It was noted from figure 5.4 that the shift in the emission peak position for annealed samples is not very pronounced compared to that of the as-deposited samples. The peaks for annealed samples were sharper as compared to the as-deposited samples. It was noted that thermal annealing improved the photoluminescence. There was also high emission intensity with annealing.

This might have been contributed by the fact that annealing enhances crystallinity of the samples. This is due to the fact that photoluminescence intensity increases with the improvement in the crystallinity of the material.

### 5.2.3 PL spectra of $In_2Se_3$: X% Bi thin films

The PL spectra of as prepared thin films deposited in the range of 350 to 600nm are shown in figure 5.5.

**Emission peaks appear between 365 and 450 nm range. The PL intensity increases with increase in bismuth percentage.**

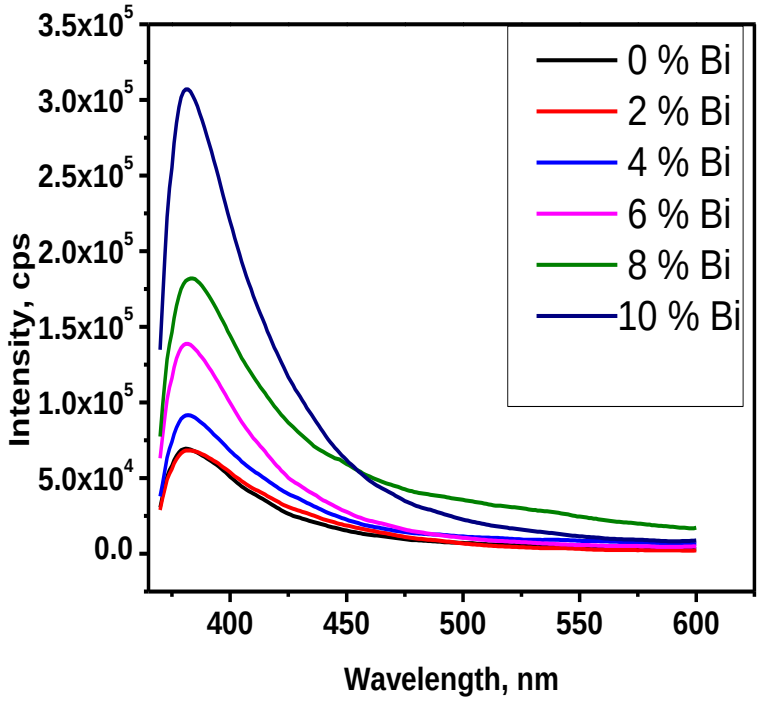


**Figure 5.5: PL spectra of as-deposited $In_2Se_3$: X% Bi thin films**

### 5.2.4 PL spectra for annealed thin film samples of $In_2Se_3$: X% Bi alloy.

Figure 5.6 represent the photoluminescence spectra for annealed thin film samples of $In_2Se_3$: X% Bi alloy. The evolution of the photoluminescence of the annealed films was studied.

Compared with the as deposited films, there was enhancement with increase in bismuth which could be attributed to improved crystallinity due to elimination of non-radiative defects. Emission increases with percentage bismuth.

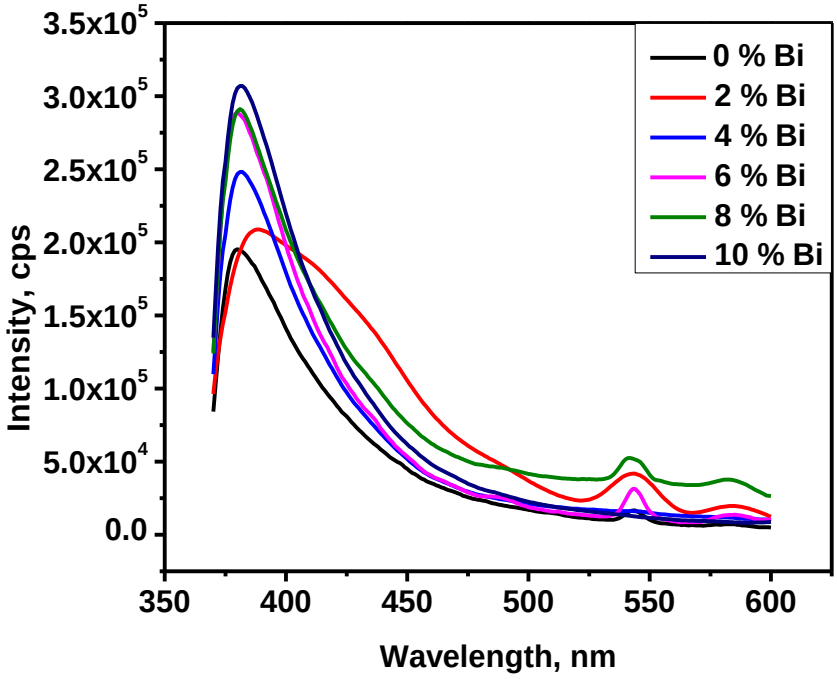


**Figure 5.6: PL spectra for annealed thin film samples of In-Se: X% Bi alloy.**

The photoluminescence emission intensity increases with improvement with crystallinity as a result of annealing. However, at about 453nm wavelength, there is emergence of a peak for 0, 4, 6 and 8% bismuth sample. This depicts that thermal annealing not only

allowed crystals to grow and improved the film's internal crystallization but also highlighted the existing defects in the thin film. As a result the PL spectrum produced a visible emission peak.

### 5.3 X-ray diffraction analysis

To investigate the effect of bismuth on glass formation, XRD measurements were done on the as-synthesised and annealed powder samples. This was repeated for as prepared and annealed thin film samples. For amorphous materials, every atom scatters the X-ray radiations which fall on them hence the absence of prominent XRD peaks and the atoms lack any order. For crystalline materials, the scattered X-rays interfere constructively and form clear prominent peaks when the Bragg's condition is satisfied.

#### 5.3.1 XRD diffractograms for as- synthesized $In_2Se_3$: X% Bi powder samples

Figure 5.7 shows XRD spectra for as synthesized $In_2Se_3$: X% Bi samples which indicates an amorphous state for the synthesized samples. The amorphous nature of the sample is deduced from the non-existence of sharp peaks in the XRD spectra. However, upon annealing the samples turned to crystalline as evident from figure 5.8 where the spectra are characterized by sharp peaks.

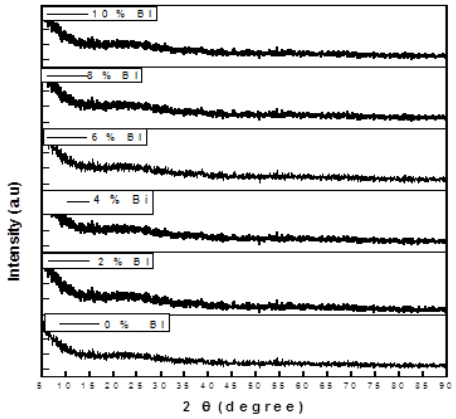


**Figure 5.7: XRD spectra of as synthesized $In_2Se_3$: X% Bi powder samples**

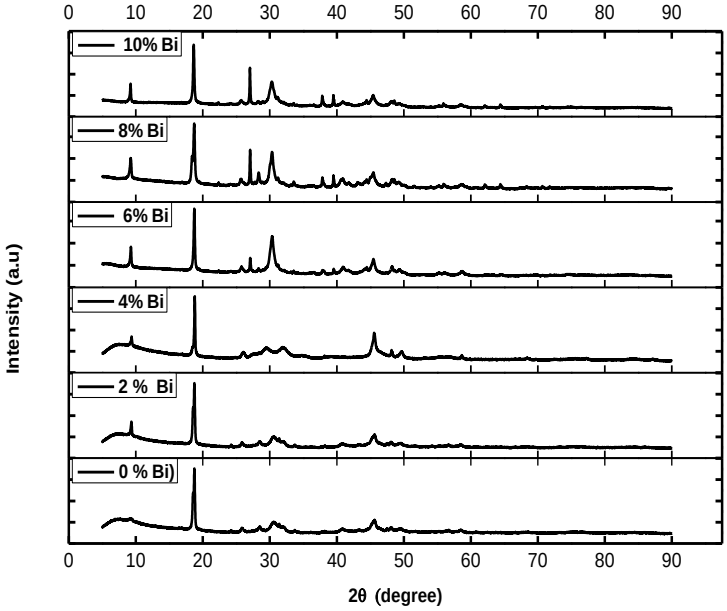


**Figure 5.8: XRD spectra of annealed powder $In_2Se_3$: X% Bi samples**

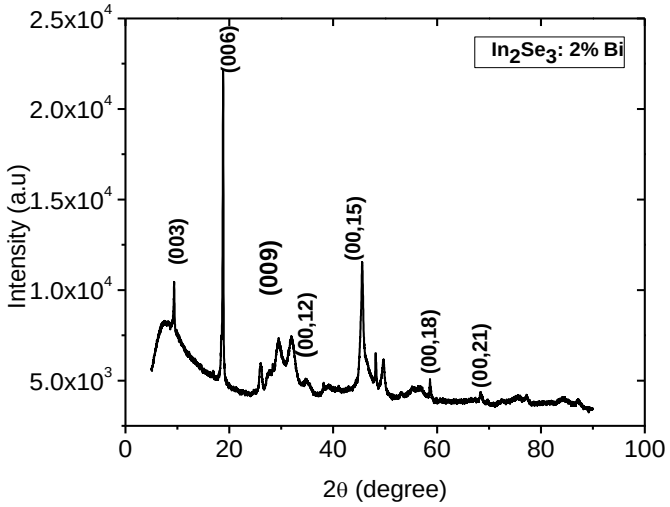


**Figure 5.9: XRD spectrum of $In_2Se_3$: 2% Bi annealed samples with peaks indexed**

From the XRD spectrum in figure 5.9, the appearance of more than one peak indicates that the sample is polycrystalline. Also the structural peaks become sharper with increase in percentage bismuth implying the samples get more crystalline. XRD patterns for all the measured samples have the following peaks;- 003, 006, 009, 0012, 0015, 0018, 0021 and 0024 as shown in figure 5.9. The most prominent peak in all samples is 006 and others are minor peaks. This is the characteristics of hexagonal structure of β-$In_2Se_3$ (Nilanthy *et al.*, 2016). There were no peaks related to bismuth indicating that bismuth was incorporated into indium selenide crystal lattice.

### 5.3.2 XRD study for $In_2Se_3$: X% Bi thin film samples

Figure 5.10 shows XRD spectra for the as deposited $In_2Se_3$: X% Bi thin films. The as-deposited thin films were also found to be amorphous. Figure 5.11 shows XRD spectrum for $In_2Se_3$: 8% Bi thin film which had been annealed at 300$^o$C in argon ambient to prevent oxidation. The spectrum exhibits sharp prominent peaks an indication of

crystalline sample. Thus the thin films changed the phase from amorphous phase to crystalline upon annealing. Again no diffraction peaks related to bismuth are observed in the spectra indicating $Bi^{3+}$were incorporated in $In_2Se_3$ crystal lattice.

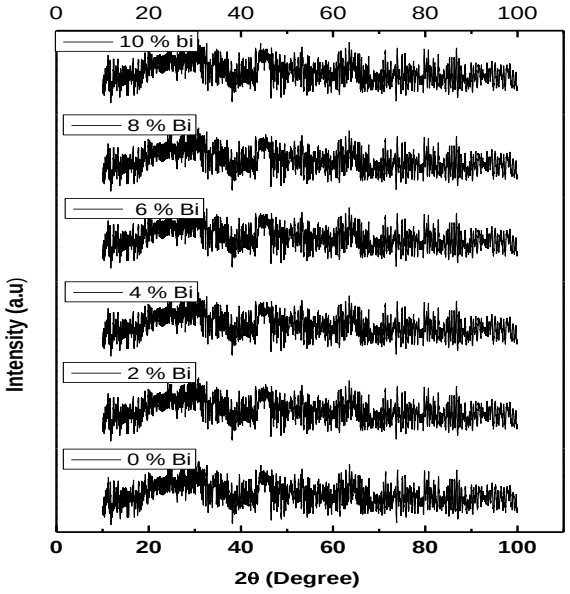


**Figure 5.10: XRD spectra for $In_2Se_3$: X% Bi as deposited thin film samples**

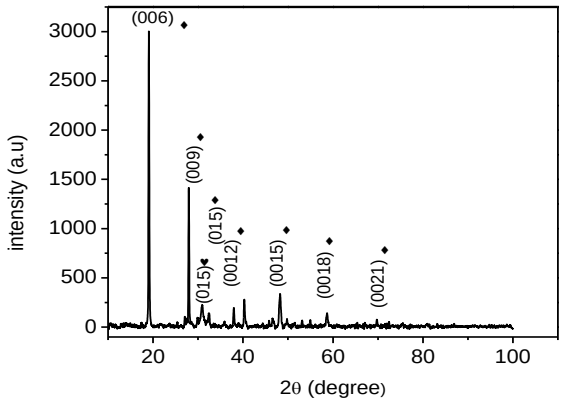


**Figure 5.11: XRD spectrum for $In_2Se_3$: 8% Bi thin film annealed at 300$^o$C**

It is clearly evident that XRD peaks become sharp after annealing implying change of phase from amorphous to crystalline.

### 5.4 Determination of film thickness for as-deposited thin film samples

**Table 5.3: Thickness of the $In_2Se_3$: X% Bi thin film samples.**

| **Stoichiometry** | **Film thickness (nm) ($\pm$0.005)** |
|---|---|
| $In_2Se_3$: 0% Bi | 185.09 |
| $In_2Se_3$: 2% Bi | 213.79 |
| $In_2Se_3$: 4% Bi | 191.00 |
| $In_2Se_3$: 6% Bi | 186.49 |
| $In_2Se_3$: 8% | 189.89 |
| $In_2Se_3$: 10% | 208.38 |

The thickness of the as deposited films was determined using Alpha-Step IQ Surface profiler with a vertical resolution of 0.012Å and vertical range of 100 Å-0.4 mm. The profiler compared the thickness of a blank glass slide with that having a film. Thin film thickness measured values are illustrated in table 5.3. From these values, film thickness range between 186.49 to 213.79 nm. This implies the thin films deposited were in the nanoscale range.

## 5.5 Optical studies

The study of optical properties of chalcogenide materials helps a great deal in understanding the optoelectronic nature of the material (Allais and Gandais, 1991; Bhargava, 1997). The properties are attributed to the interaction of incident photons and the semiconductor material. For optical parameters determination of the ternary In-Se-Bi material, both transmittance and reflectance in the spectral range 250-2500nm were measured. Among the parameters obtained include optical band gap ($E_g$) and film thickness.

### 5.5.1 Reflectance for the as synthesized powder samples of $In_2Se_3$: X %Bi

Figure 5.12 represents graphs of percentage reflectance versus wavelength for as synthesized powder samples. The plots exhibit almost a straight line in the high energy absorption region. When this region is extrapolated to zero of abscissa, band gap values can be determined at the intercept on the x axis (Quan, 1987, Damodardas and Karunakaran, 1983).

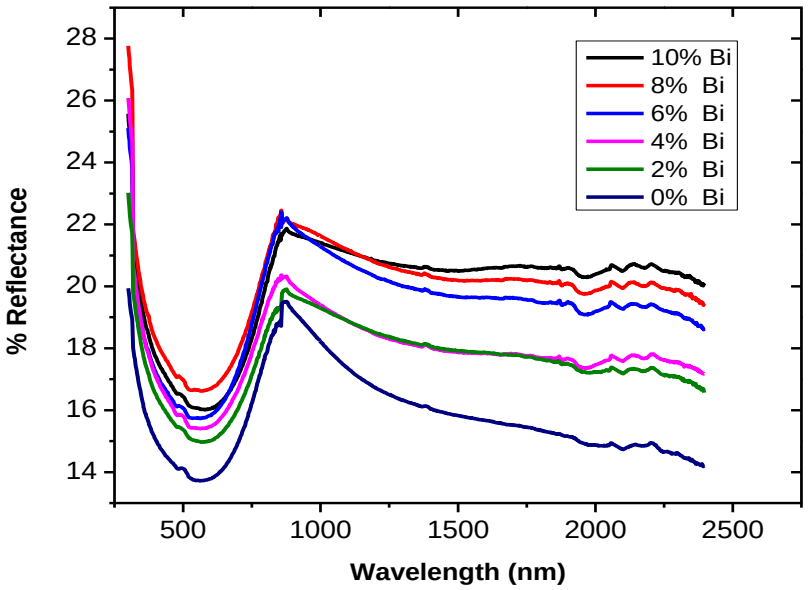


**Figure 5.12: Percentage reflectance versus wavelength for the as synthesized powder samples of $In_2Se_3$: %X Bi**

From figure 5.12 it is observed that reflectance initially reduces to a minimum before increasing to a maximum then reduces as the wavelength is increased for all samples. An enhanced reflectance is noted for all samples with Bismuth. At higher wavelength above 1000 nm an increase in reflectance is evident with increased Bismuth percentage but this is not explicit at lower wavelengths.

A sharp decline in reflectance is observed for $In_2Se_3$: 0% Bi starting at 862 nm which can be attributed to strong absorption. After adding bismuth in the percentages of 2, 4, 6, 8 and 10, the absorption edge suffered a gradual blue shift and in addition the reduction in the reflectance at higher wavelengths is gradual.

### 5.5.2 Reflectance spectra for annealed $In_2Se_3$: X% Bi samples

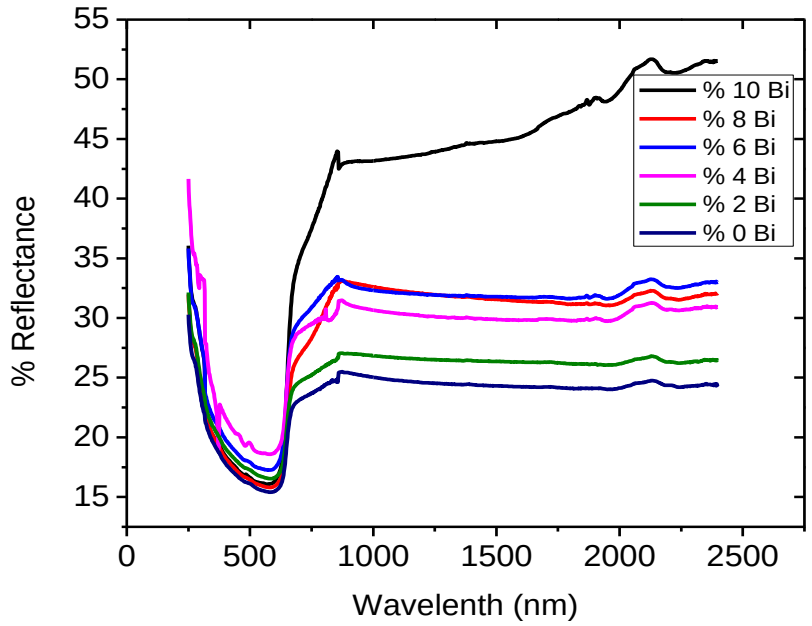


**Figure 5.13: Reflectance spectra for annealed $In_2Se_3$: X% Bi samples**

Figures 5.13(a-f), represents reflectance for annealed samples of $In_2Se_3$: X% Bi. Compared to the as prepared samples, reflectance is higher. Again just like the as prepared samples, percentage reflectance increase with percentage bismuth. It has been reported from earlier studies that there is influence of composition of elements on the optical properties (Zahed *et al.,* 2000). There is a great contrast between undoped and doped samples. This clearly shows that addition of bismuth has a significant influence on the indium selenide alloy for semiconductor memory application.

### 5.5.3 Band gap for as synthesized powder samples of $In_2Se_3$: X% Bi

The reflectance spectra were analysed by use of Kubelka-Munk relation where reflectance was converted to kubelka-Munk function. Figure 5.14 represents Kubelka-

Munk curves for $In_2Se_3$: X% Bi for X= 0, 2, 4, 6, 8 and 10% Bi. This involves plotting of $(k*h\nu)^2$ versus hν, where the x-axis intercept by extrapolation of the linear part of the plot yields band gap of the material.

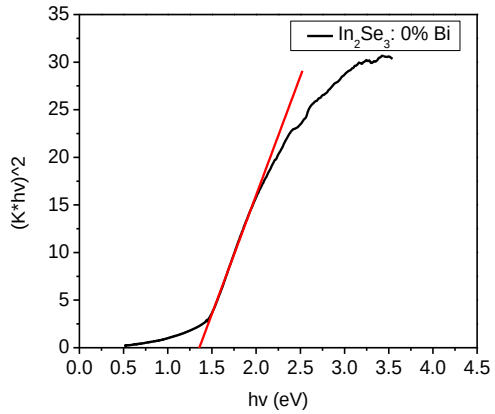


(a)

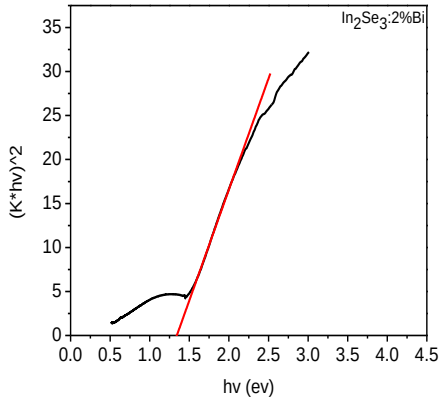


(b)

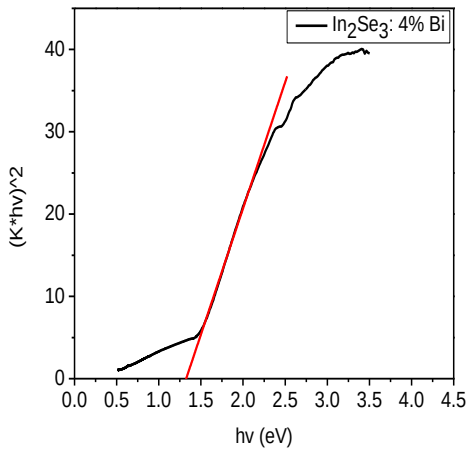


(c)

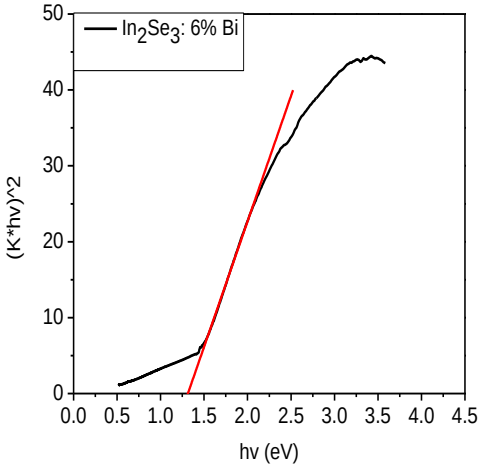


(d)

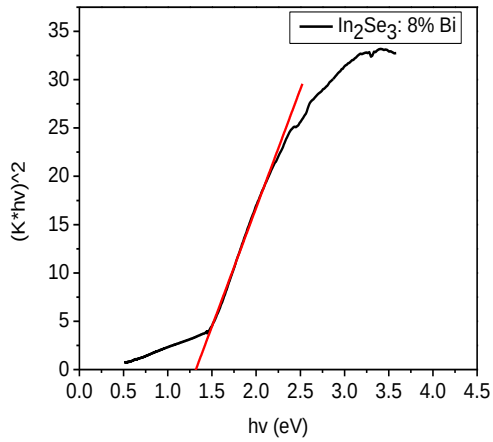


(e)

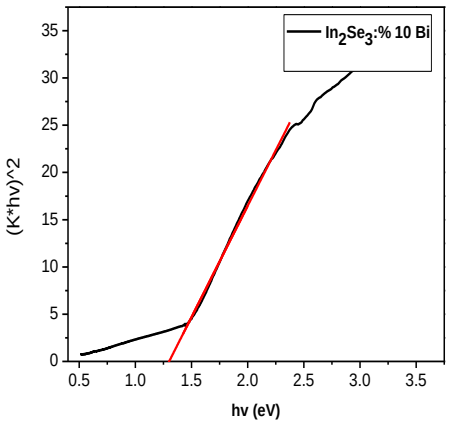


(f)

**Figure 5.14 (a-f): Plot of $(k*h\nu)^2$ versus hv for as synthesized samples of (a) $In_2Se_3$: 0% Bi (b) $In_2Se_3$: 2% Bi (c) $In_2Se_3$: 4% Bi (d) $In_2Se_3$: 6% Bi (e) $In_2Se_3$: 8% Bi (f) $In_2Se_3$: 10% Bi**

Band gap values for $In_2Se_3$: X % Bi are tabulated in table 5.4.

**Table 5.4: Determined band gap energies for as prepared powder samples of $In_2Se_3$: X % Bi (for X= 0, 2, 4, 6, 8 and 10%)**

| % Bi | 0 | 2 | 4 | 6 | 8 | 10 |
|---|---|---|---|---|---|---|
| Band gap in eV ($\pm$0.005) | 1.36 | 1.35 | 1.33 | 1.32 | 1.31 | 1.30 |

Figure 5.15 shows a curve drawn from band gap values in table 5.4. It is clearly shown that bad gap energy decreases with increase in percentage bismuth.

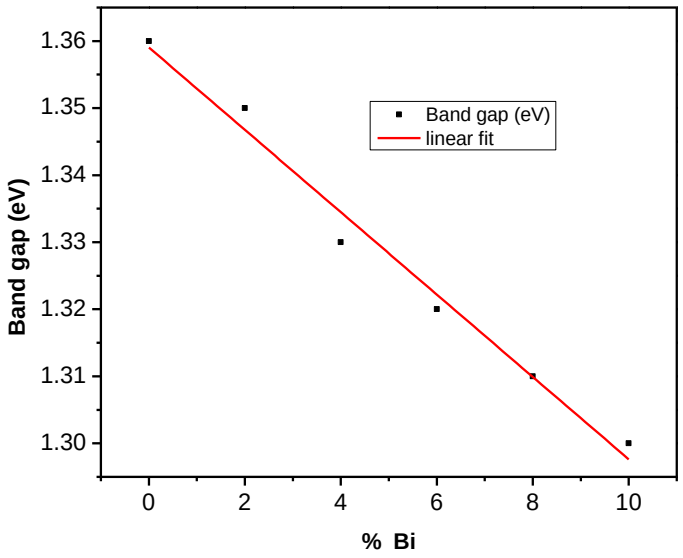


**Figure 5.15: Curve presenting variation of bad gap energy versus percentage bismuth**

### 5.5.4 Band gap for annealed powder samples of $In_2Se_3$: X% Bi

Band gap energies for annealed powder samples were determined. Figure 5.16 presents Kubelka-Munk plots for $In_2Se_3$: X% Bi for X= 0, 2, 4, 6, 8 and 10% Bi.

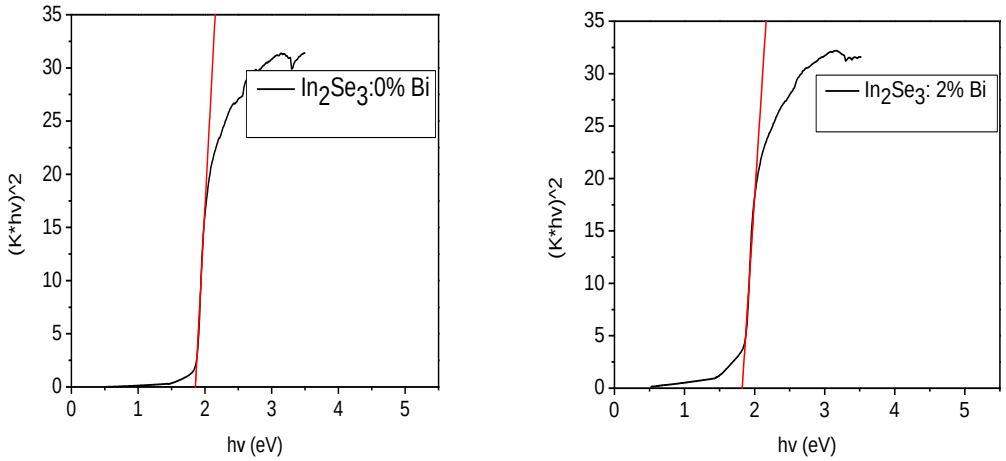


(a) (b)

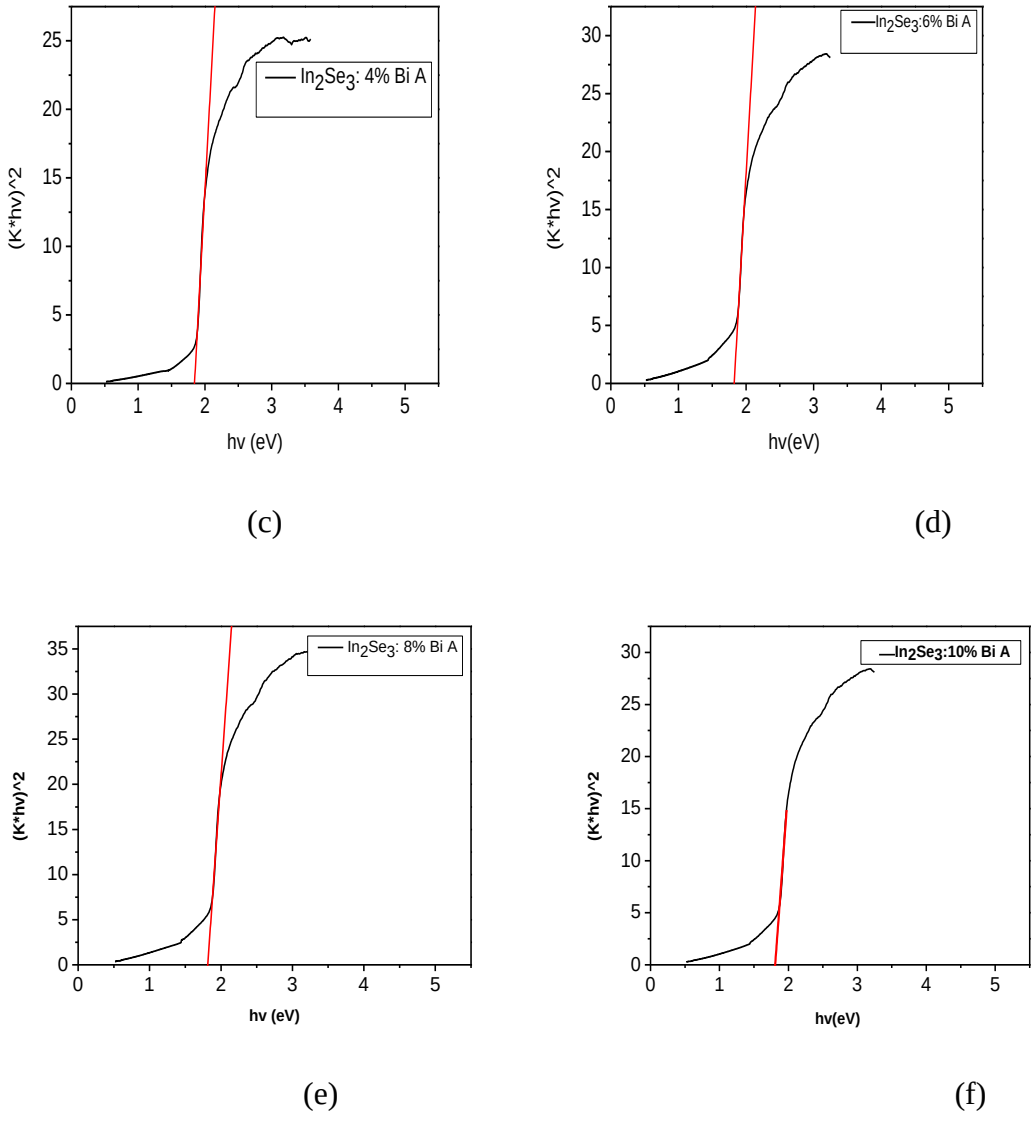


(c) (d)

(e) (f)

**Figure 5.16 (a-f): Plot of $(k*h\nu)^2$ versus hν for annealed powder samples of (a) $In_2Se_3$: 0% Bi (b) $In_2Se_3$: 2% Bi (c) $In_2Se_3$: 4% Bi (d) $In_2Se_3$: 6% Bi (e) $In_2Se_3$: 8% Bi and (f) $In_2Se_3$:10% Bi**

Figure 5.16 illustrates how band gaps for the annealed samples are obtained. These values are tabulated in table 5.5. The range is between 1.85 eV to 1.79 eV.

**Table 5.5: Determined band gap energies for annealed powder samples of $In_2Se_3$: X% Bi (for X= 0, 2, 4, 6, 8 and 10%)**

| % Bi | 0 | 2 | 4 | 6 | 8 | 10 |
|---|---|---|---|---|---|---|
| Band gap in eV (± 0.005) | 1.85 | 1.84 | 1.83 | 1.82 | 1.80 | 1.79 |

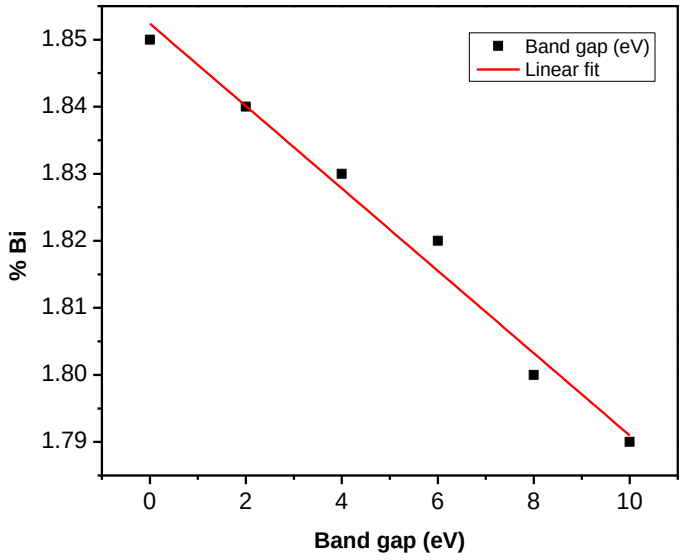


**Figure 5.17: Plot of percentage bismuth versus band gap energy for annealed samples of $In_2Se_3$: X% Bi**

The optical band gap values for annealed $In_2Se_3$: X% Bi (X = 0, 2, 4, 6, 8 and 10) Bi thin films were determined. From the table 5.5, optical band gap decreased from 1.85 eV to 1.79 eV with increase in bismuth percentage from 0-10% as shown in figure 5.17. This may be due to the fact that addition of bismuth led to production of localized states near the conduction band edge (Sharmal *et al.*, 2012). Therefore conduction is as a result of electrons hopping into the localized states near the conduction band edges after

excitation. Band gap monotonically decreases with increase in % bismuth. This may occur due to defect density, large density of dislocations and barrier height change owing to size of grain in polycrystalline thin film. The defects may act as donor defect states or acceptor defect states in semiconductors depending on the band gap energy values. With thermal annealing energy of about 300K, electrons are likely to be excited from valence band to donor states or from donor states to conduction band.

Band gap energy values for as prepared and annealed samples are listed in tables 5.4 and 5.5 respectively. It can be deduced that band gap values decreased with percentage of bismuth. In this case decrease in band gap values with bismuth addition may be attributed to reduction in disorder and increase in density of defect states (Khan *et al.,* 1997). Similar results were reported by early researchers (Mehra *et al.,* 1997 and Kambo *et al.,* 2002).

Bismuth has been reported to create localized states in band gap (Barreau *et al.,* 2001). For the annealed films which likewise showed reduction in band gap with addition of percentage bismuth, may be as a result of rearrangement of localized defects states, D+ and D- (Mott *et al.,* 1975). When a sample of material is illuminated in non-equilibrium condition, electrons and holes are generated and $D_0$ centres. There are charged defect centres D+ and D- which can be trap centres for the generated electrons and holes due to illumination. Most of the excess holes and electrons are trapped by these charged defect centres. This follows the reactions $D^+ + e = D_0$ and $D^- + H = D_0$. When illumination stops, density of $D_0$ reduces due to recombination. This follows the reaction $2\ D_0 = D^+ +$

D-. $D_0$ centre is converted to D+ and D-. The reactions which entail trapping and recombination greatly affect photoconductivity of materials. Recombination involves tunneling of band tail electrons to neutral dangling bonds $D_0$ and holes diffusion in tail states recombining with D-. Addition of bismuth content to a material leads to creation of defect centres which could lead to creation of more localized defect states. The localized defect states act as trapping centres. This leads to conclusion that charge carrier concentration increases as the bismuth increases hence enhanced conductivity.

### 5.6 Transmittance spectra for $In_2Se_3$: X% Bi as-deposited thin films

Optical transmittance measurements were recorded in the wavelength range from 250 to 2500nm. Figures 5.18 (a-f) represents transmittance spectra for as-deposited $In_2Se_3$: X% Bi thin films.

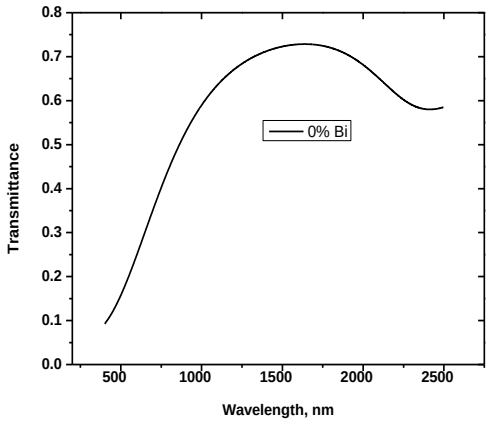


(a)

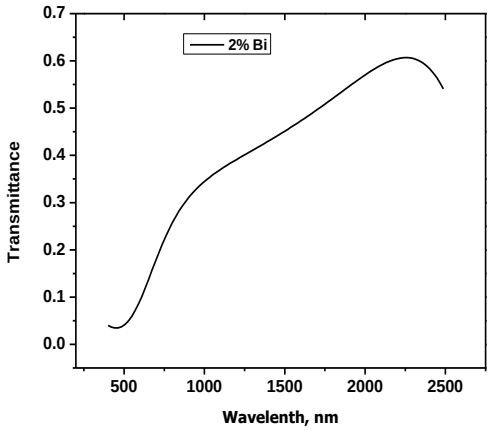


(b)

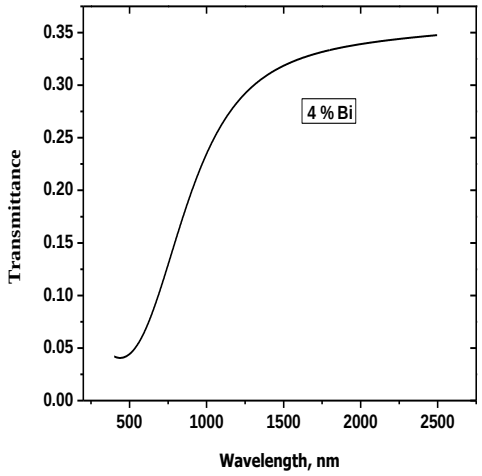


(c)

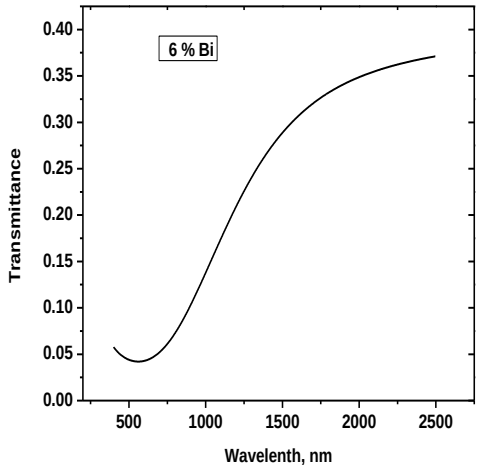


(d)

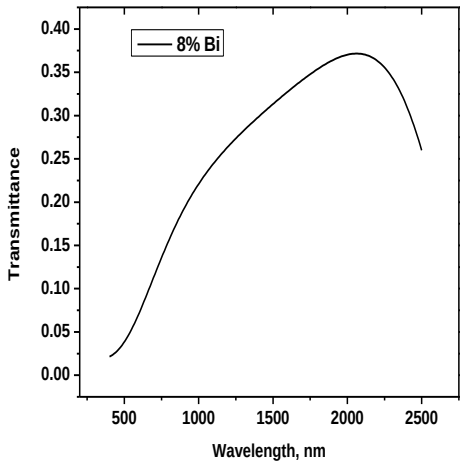


(e)

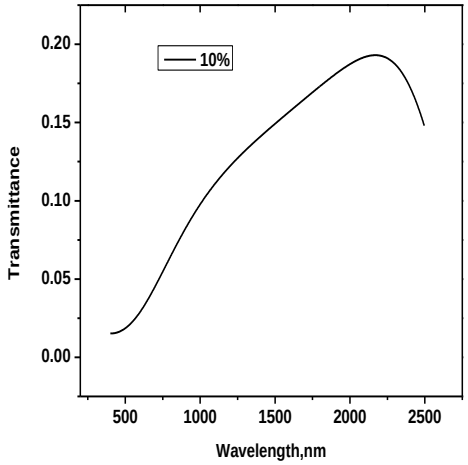


(f)

**Figure 5.18(a-f): Transmittance spectra for $In_2Se_3$: X Bi% (X = 0, 2, 4, 6, 8, 10) for as-deposited thin films.**

From figure 5.18(a-f), transmittance spectra for as deposited thin films, has got three distinct regions. These are high absorption region, exponential edge region and weak absorption tail region. Band to band transition cause the high absorption region followed

by Urbach tail. Defects and impurities give rise to the weak absorption tail. The exponential edge is due to structural randomness which characterizes glassy materials. The high absorption region is the one which determines the band gap. Transmittance in this research was used to determine the film thickness values which were compared with measured values.

### 5.6.1 Film thickness analysis

Using Scout software, experimental and simulated transmittance curves were compared. At the point where simulated and experimental curves were in good agreement, film thickness values were derived from fit parameters. The measured film thickness values were compared with those obtained from simulation using Scout 2.4 version software models. The transmittance curves for experimental and simulated data are illustrated in figure 5.19(a-f). The good correlation between simulated and experimental curves implies that the fit parameters describe the sample adequately.

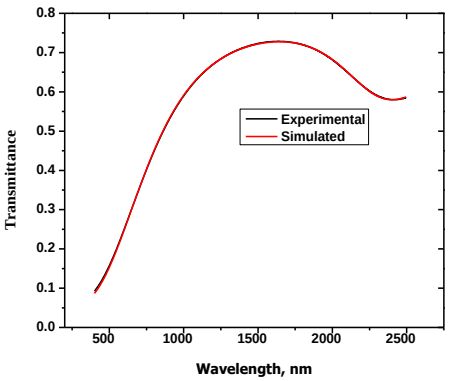


(a) 0% Bi

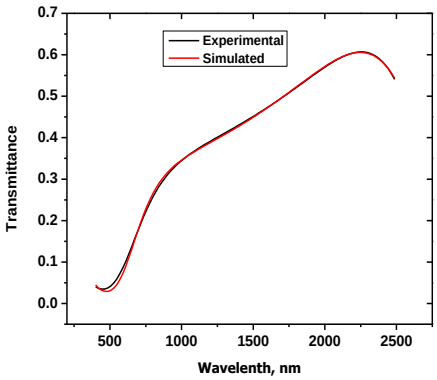


(b) 2% Bi

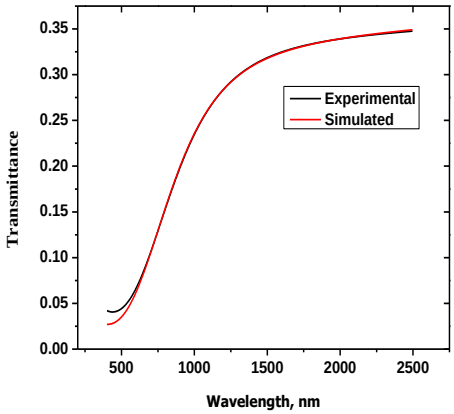


(c) 4% Bi

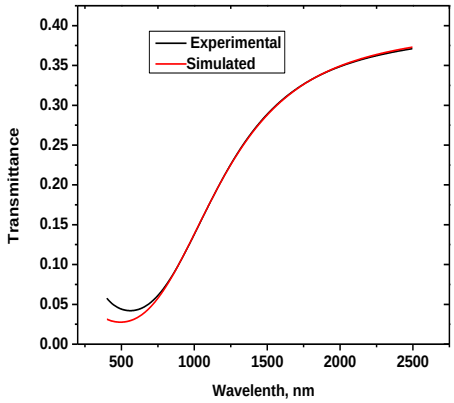


(d) 6% Bi

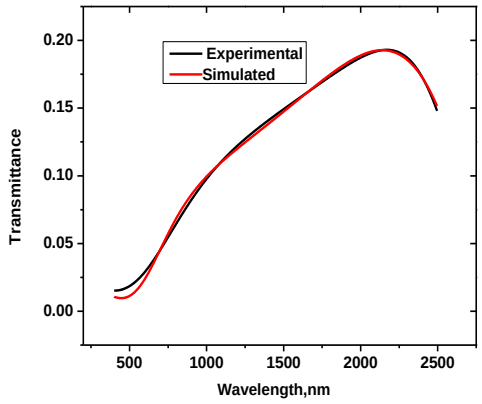


(e) 8% Bi

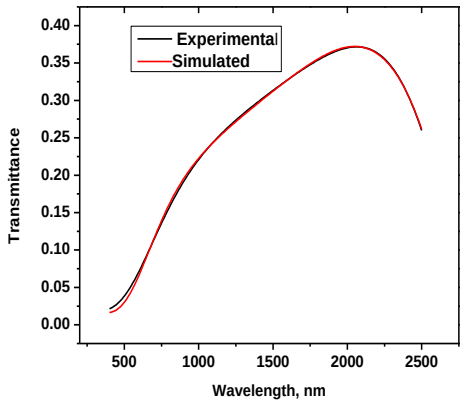


(f) 10% Bi

**Figure 5.19(a-f): Experimental results versus simulated results for transmittance curves for $In_2Se_3$-X% Bi thin film samples**

**Table 5.6: Comparison of measured and simulated values of thin films thickness**

| Bi concentration in $In_2Se_3$ | Simulated film thickness (nm)(±0.05) | Measured film thickness (nm)(±0.005) | Percentage difference |
|---|---|---|---|
| 0% | 185.1 | 185.09 | 0.005 |
| 2% | 213.8 | 213.79 | 0.004 |
| 4% | 191.0 | 191.00 | 0.00 |
| 6% | 186.5 | 186.49 | 0.005 |
| 8% | 189.9 | 189.89 | 0.005 |
| 10% | 208.4 | 208.38 | 0.01 |

Figure 5.19(a-f) presents the fittings of experimental and simulated data for as deposited $In_2Se_3$: % Bi (X= 0, 2, 4, 6, 8 and 10) thin films. There was good agreement between experimental and simulated data for all the samples. Table 5.6 presents the comparison between simulated and measured values of thin films thickness. From the figures of percentage difference determined, the measured and simulated values were very close thus showing good agreement.

### 5.7 Electrical characteristics

Current versus voltage (I-V) curves for $In_2Se_3$: X% Bi were plotted as shown in figures 5.20 (a-f). A linear fit was plotted on the I-V curves. The slope yielded resistivity of the samples.

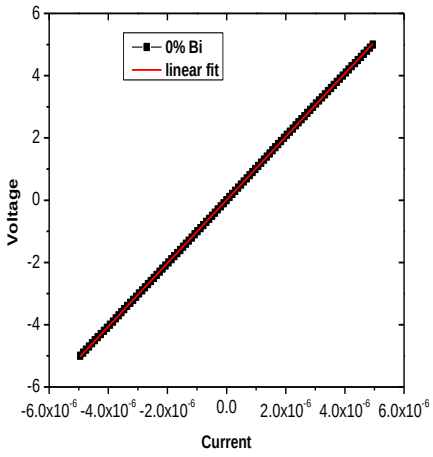
0% Bi
linear fit
Voltage
Current
6
4
2
0
-2
-4
-6
-6.0x10-6 -4.0x10-6 -2.0x10-6 0.0 2.0x10-6 4.0x10-6 6.0x10-6

(a)

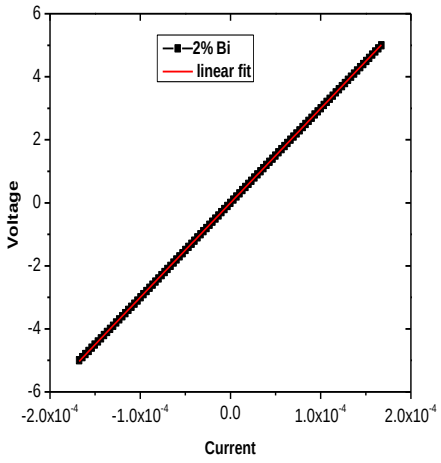
2% Bi
linear fit
Voltage
Current
6
4
2
0
-2
-4
-6
-2.0x10-4 -1.0x10-4 0.0 1.0x10-4 2.0x10-4

(b)

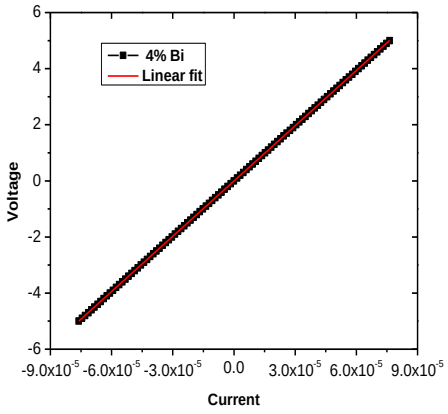
4% Bi
Linear fit
Voltage
Current
6
4
2
0
-2
-4
-6
-9.0x10-5 -6.0x10-5 -3.0x10-5 0.0 3.0x10-5 6.0x10-5 9.0x10-5

(c)

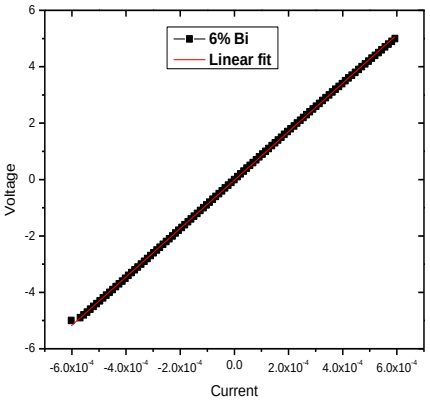
6% Bi
Linear fit
Voltage
Current
6
4
2
0
-2
-4
-6
-6.0x10-4 -4.0x10-4 -2.0x10-4 0.0 2.0x10-4 4.0x10-4 6.0x10-4

(d)

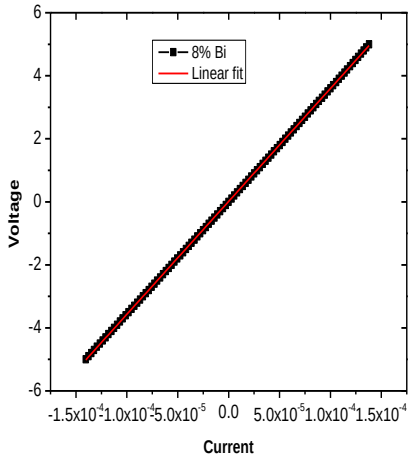


(e)

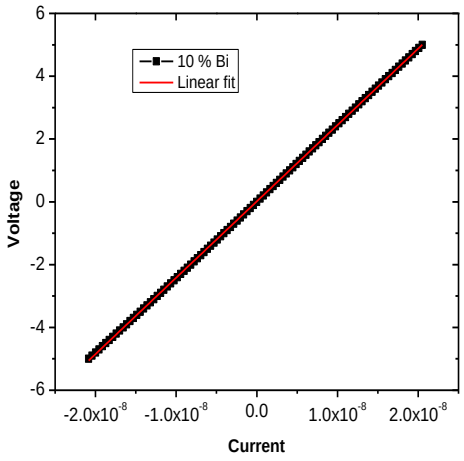


(f)

**Figure 5.20(a-f): I-V curves for as deposited $In_2Se_3$: X% Bi (for X= 0, 2, 4, 6, 8, and 10)**

Resistivity values determined from equation 4.1 are listed in table 5.6.

**Table 5.6: Thin film resistivity values**

| Sample (X%Bi) | 0 | 2 | 4 | 6 | 8 | 10 |
|---|---|---|---|---|---|---|
| Resistivity (MΩcm) (±0.005) | 85.19 | 72.55 | 56.83 | 30.83 | 29.03 | 22.96 |

From table 5.6, it is clear that the resistivity of all thin films decrease with increasing bismuth concentration. This may be accredited to increase in carrier concentration with increase in bismuth. From figures 5.26 (a-f), it can be deduced that dark conductivity of

the samples increases with increase in bismuth. This may be due to shifting of Fermi level to conduction band.

### 5.8 Field emission scanning electron microscopy analysis

Field emission scanning electron microscopy (FESEM) analysis was carried out on both powder and thin film samples. This applied to as prepared and annealed samples.

#### 5.8.1 SEM images for as-synthesized $In_2Se_3$: X% Bi powder samples

SEM micrographs showing the typical particle morphology are shown in figure 5.21(a-e). These images show that the bulk samples of the alloy are made up of an agglomeration of particles with no regular shape.

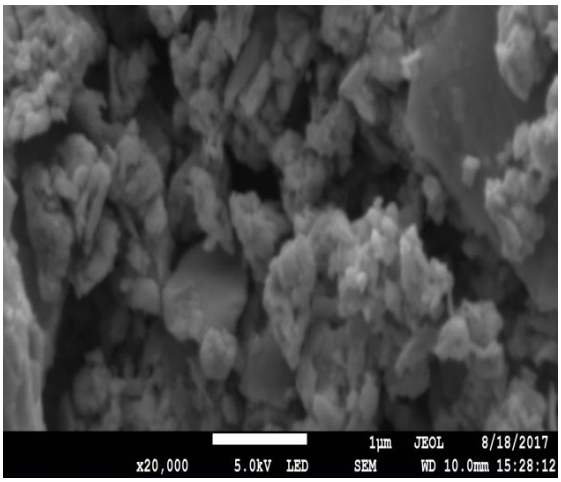


(a). $In_2Se_3$-0%Bi

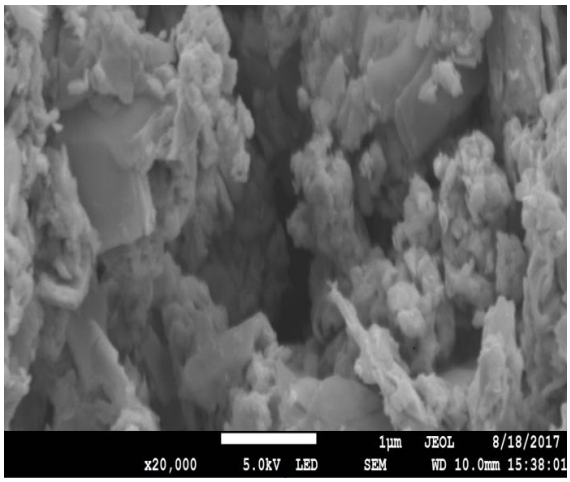


(b). $In_2Se_3$-2% Bi

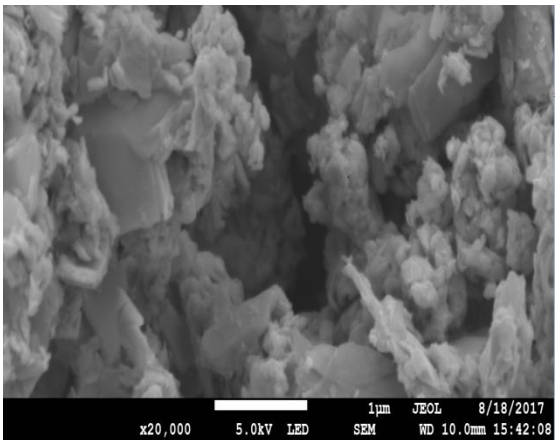


(c). $In_2Se_3$-4% Bi

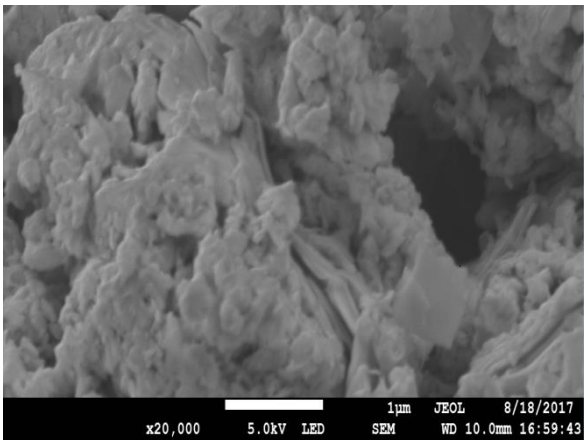


(d). $In_2Se_3$-8%Bi

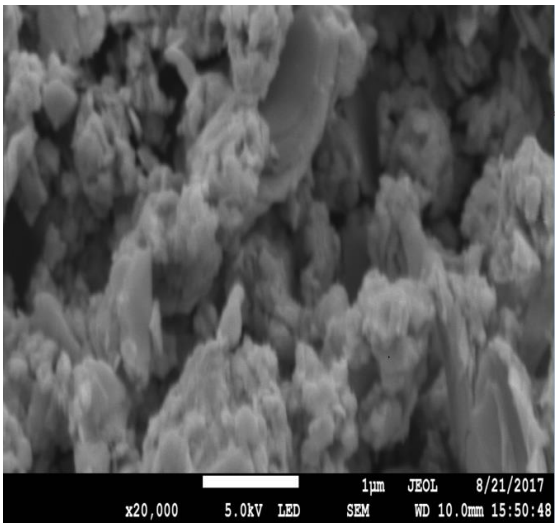


(e). $In_2Se_3$-10% Bi

**Figure 5.21 (a-e): SEM micrographs for as synthesised powder samples of $In_2Se_3$: X% Bi**

### 5.8.2 SEM images for annealed $In_2Se_3$-X% Bi powder samples

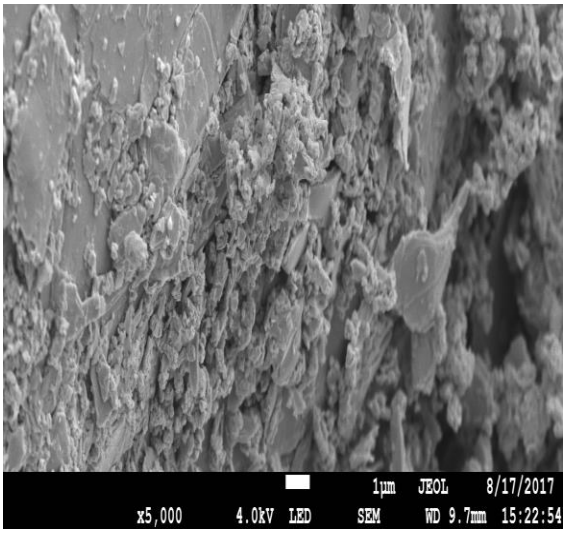


(a). $In_2Se_3$-0% Bi

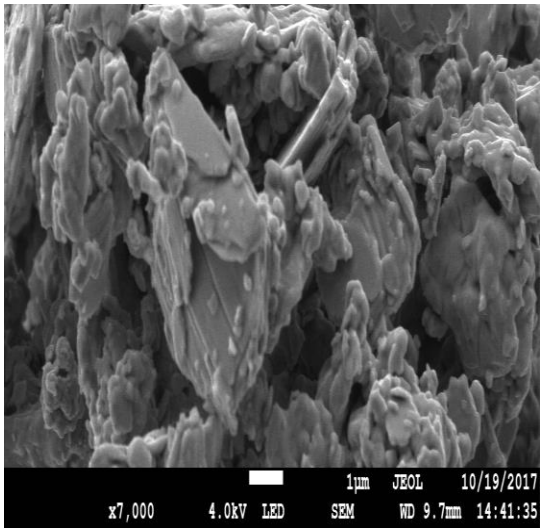


(b). $In_2Se_3$-2% Bi

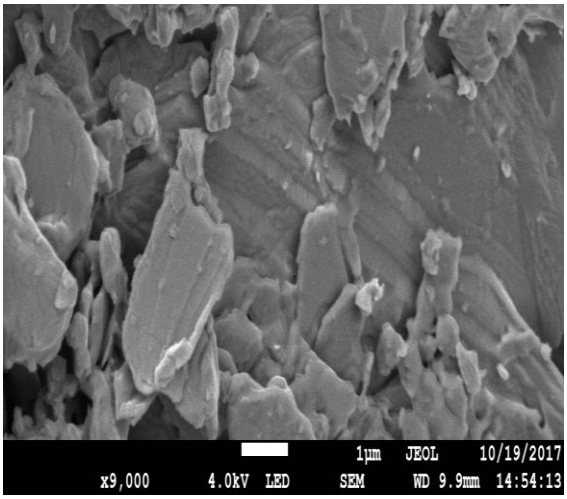


(c). $In_2Se_3$-4% Bi

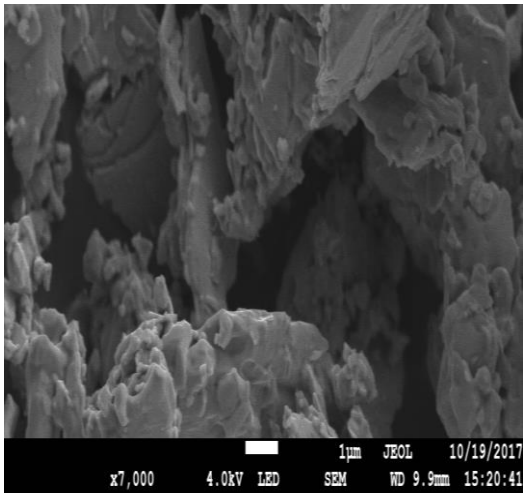


(d). $In_2Se_3$-6% Bi

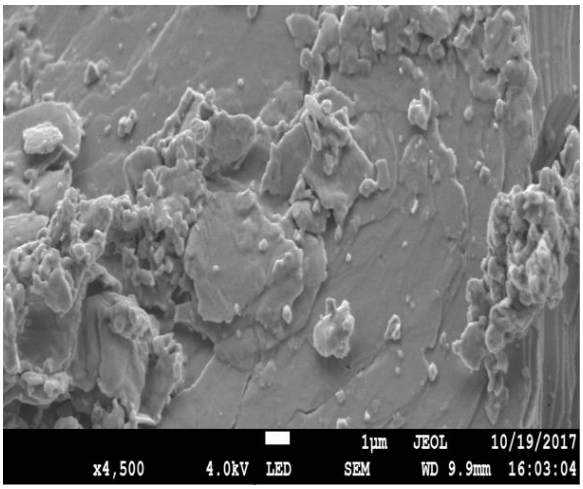


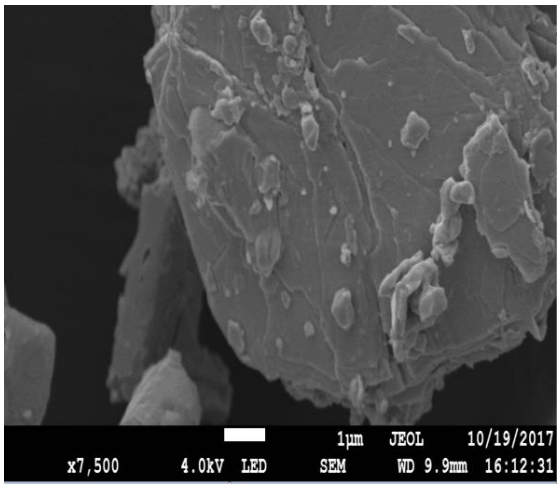


(e). $In_2Se_3$-8%Bi (f). $In_2Se_3$-10%

**Figure 5.22 (a-f): SEM images for annealed powder samples of $In_2Se_3$: X% Bi**

The SEM images in figure 5.22 exhibits that bulk powder samples were made up of an agglomeration of platelets and flakes like nano particles. There was evidence of hollows and pores on the surface as a result of gases that evolved during combustion. It can be deduced that there is change in phase of the materials as a result of crystallization. Similar results were reported elsewhere (Alvi, 2014).

### 5.8.3 Energy dispersive spectroscopy (EDS) spectra for as synthesized $In_2Se_3$: X% Bi samples

To study the chemical composition of the samples, energy dispersive spectroscopy (EDS) was employed.

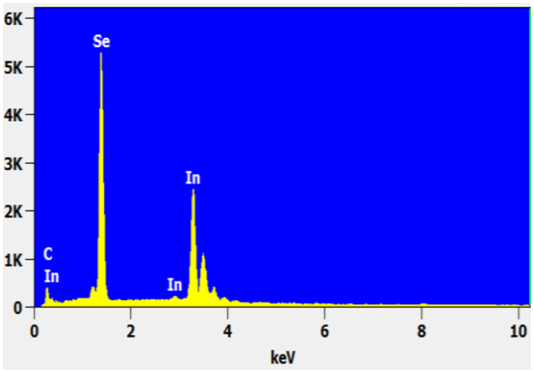


(a). $In_2Se_3$-0% Bi

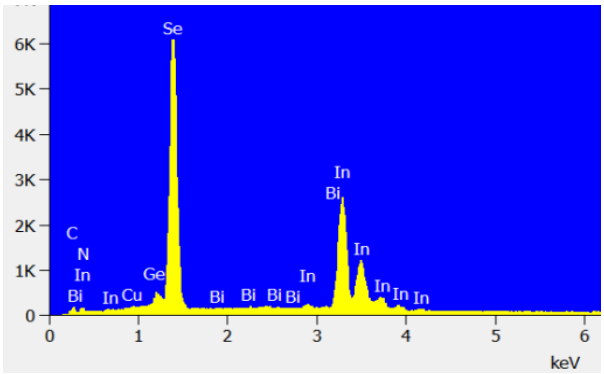


(b).$In_2Se_3$-2% Bi

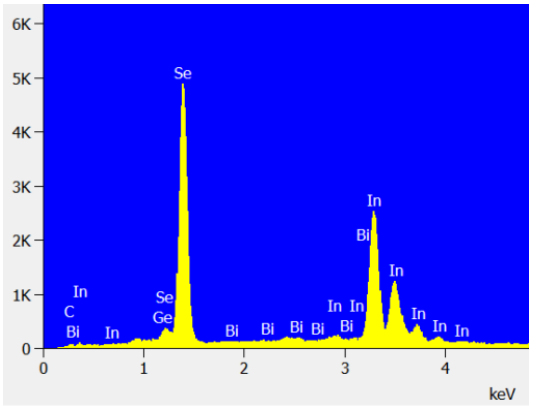


(c). $In_2Se_3$-4 Bi

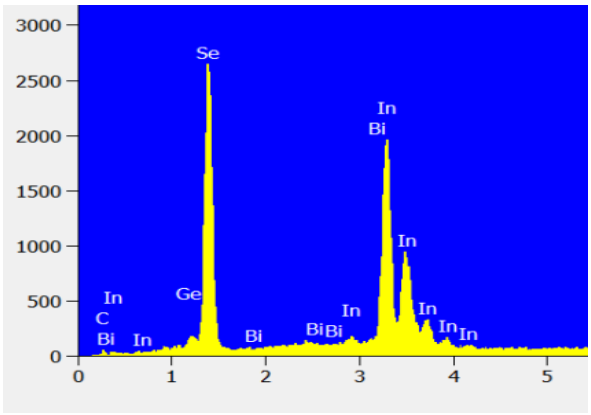


(d). $In_2Se_3$-6% Bi

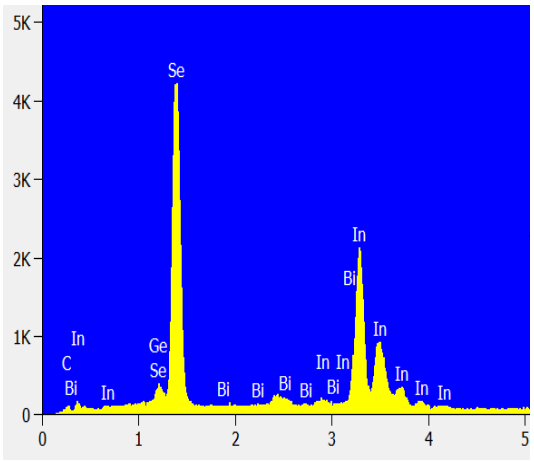


(e). $In_2Se_3$-8% Bi

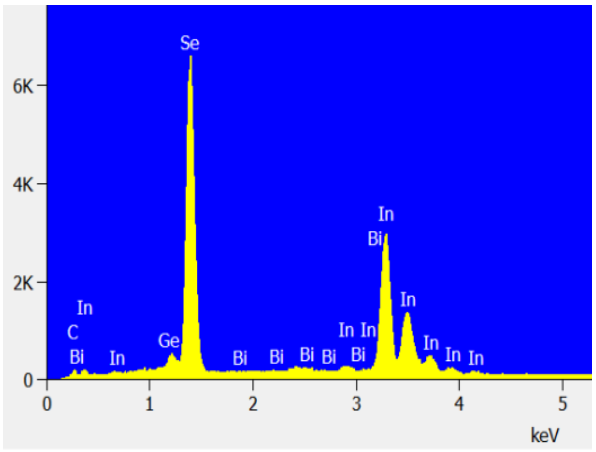


(f). $In_2Se_3$-10% Bi

**Figure 5.23(a-f): EDS images for as synthesized powder samples of $In_2Se_3$: X% Bi**

Figure 5.23(a-f) shows EDS spectra for as synthesized powder. All the constituent elements were present in all the samples. There was also presence of carbon which was used to seal the samples. Germanium was also recorded as a result of contamination during sample synthesis.

### 5.8.4 EDS spectra for annealed $In_2Se_3$: X% Bi powder samples

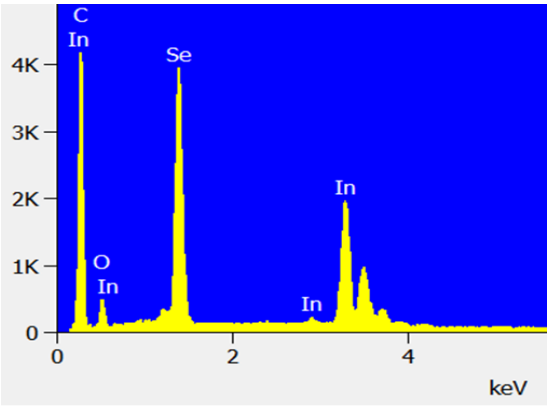


(a) . $In_2Se_3$-0% Bi

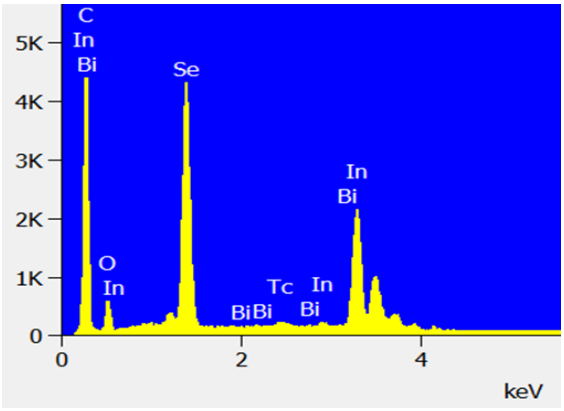


(b). $In_2Se_3$-2% Bi

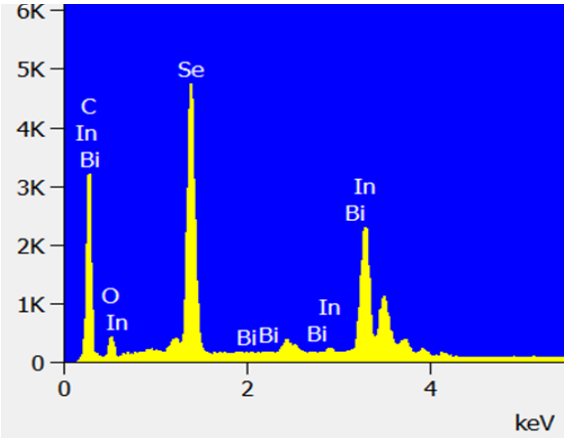


(c) $In_2Se_3$-4% Bi

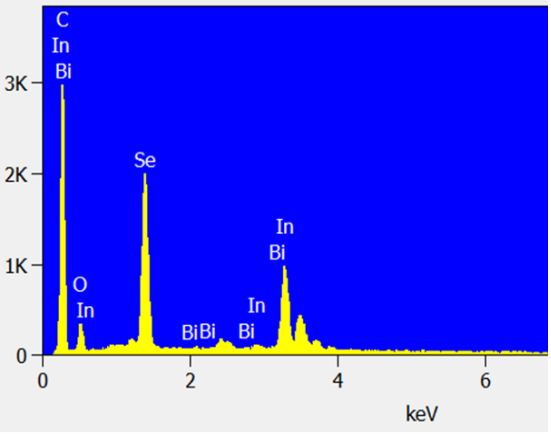


(d). $In_2Se_3$-6% Bi

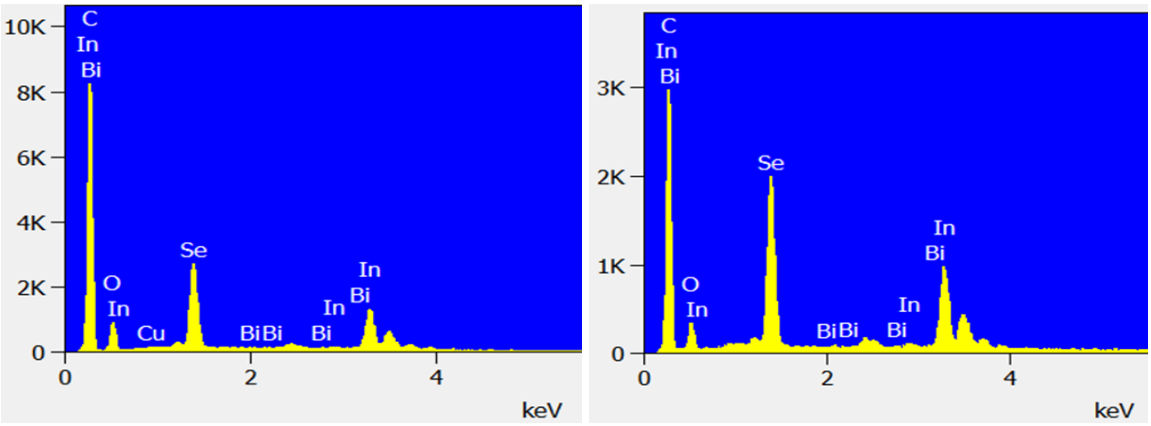


(e). $In_2Se_3$-8% Bi (f). $In_2Se_3$-10% Bi

**Figure 5.24 (a-f): EDS images for annealed powder samples of $In_2Se_3$:X% Bi**

Figures 5.24(a-f) represent EDS spectra for annealed powder samples of $In_2Se_3$: X% Bi. All the samples had the constituent elements but carbon was in large quantity since it was used to seal the powder samples. There was also presence of oxygen due to exposure to air while running the samples in the equipment. The composition of $In_2Se_3$: X% Bi is paramount since device properties can be altered by deviation from stoichiometry (Noufi *et al.*, 1984).

### 5.8.5 SEM images for $In_2Se_3$: X% Bi thin films

To study morphological properties and chemical composition of the thin films, a comprehensive analysis by FESEM and EDS techniques was performed. Figures 5.25(a-f) shows FE-SEM images of $In_2Se_3$: X% Bi annealed thin film samples. The thin film images depict a uniform structure composed of large and small spherical particles. Particles are spherical in shape and are scattered irregularly on the film surface.

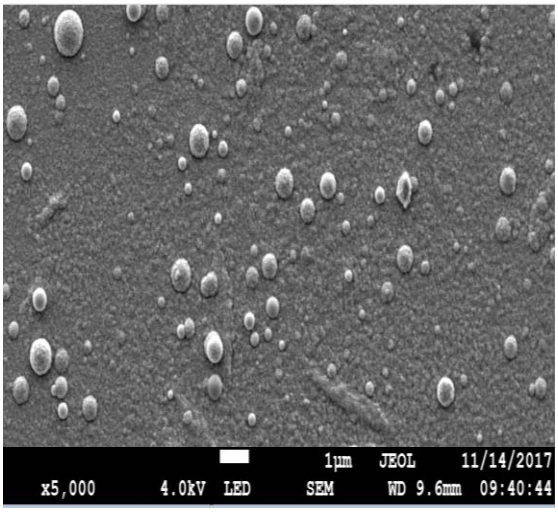


(a). $In_2Se_3$-0% Bi

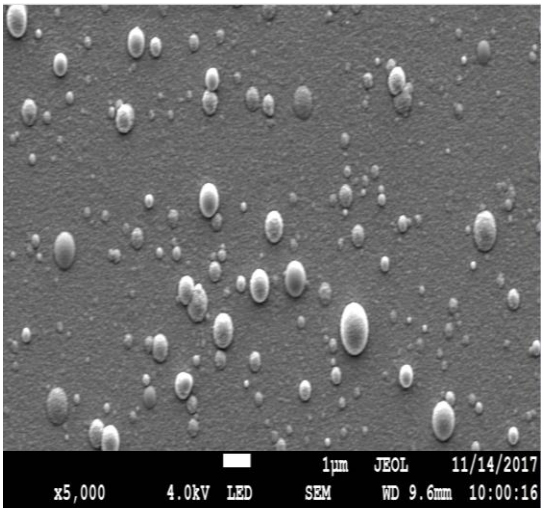


(b).$In_2Se_3$-2%Bi

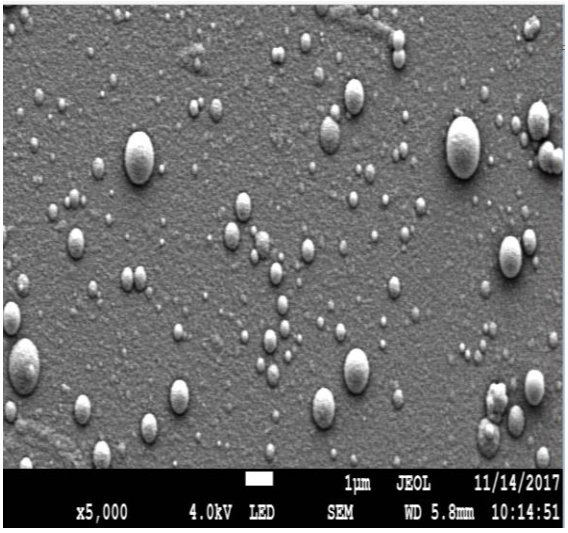


(c). $In_2Se_3$-4% Bi

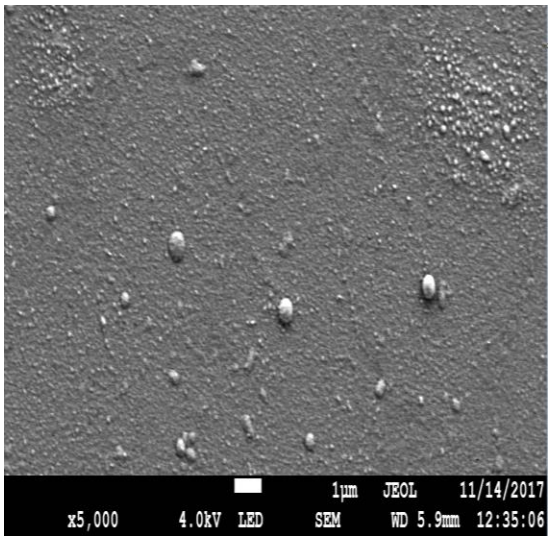


(d). $In_2Se_3$-6% Bi

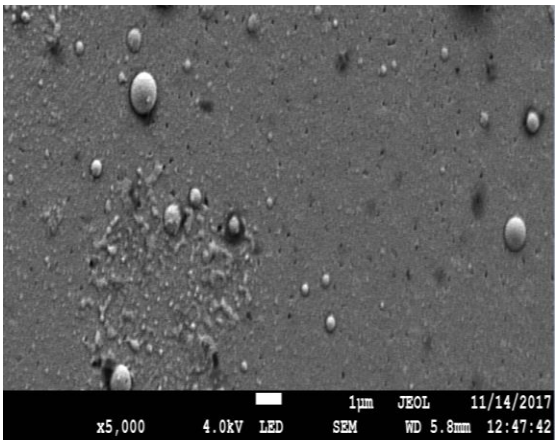


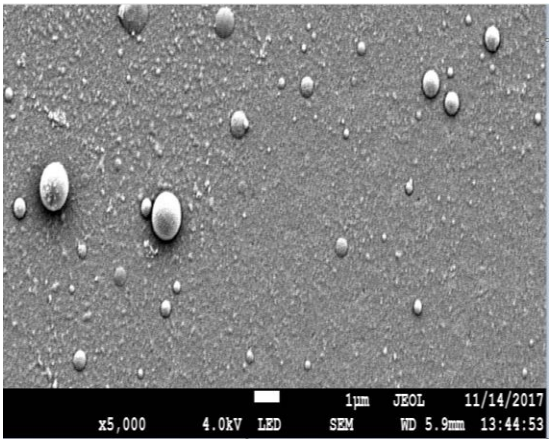


(e). $In_2Se_3$-8% Bi (f). $In_2Se_3$-10% Bi

**Figure 5.25(a-f): SEM micrographs for $In_2Se_3$: X% Bi annealed thin films samples**

### 5.8.6 EDS Images of $In_2Se_3$: X% Bi annealed thin films samples

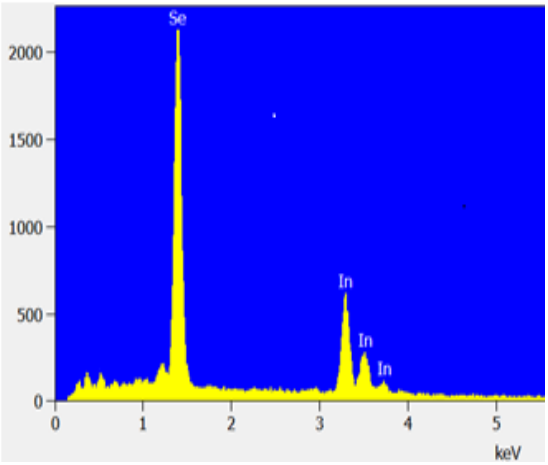


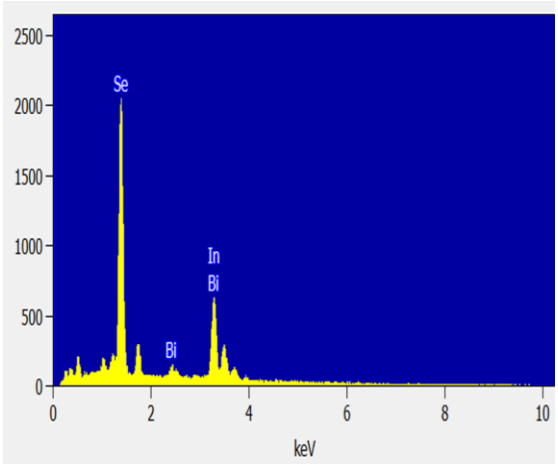


(a). $In_2Se_3$-0% Bi (b). $In_2Se_3$-2% Bi

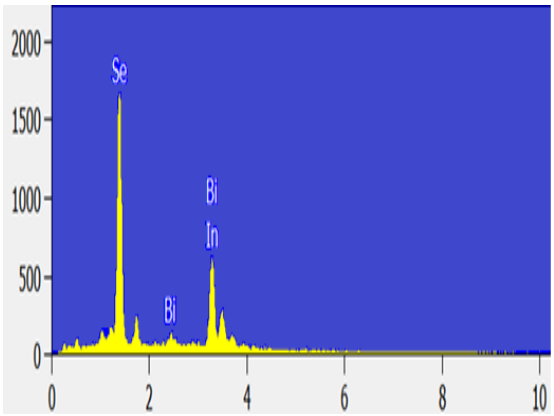


(c). $In_2Se_3$-4% bi

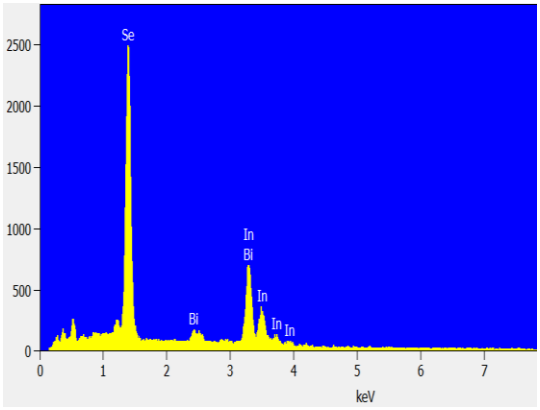


(d). $In_2Se_3$-6% Bi

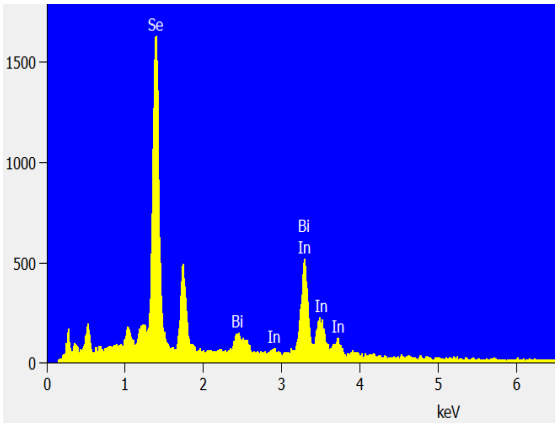


(e). $In_2Se_3$-8% Bi

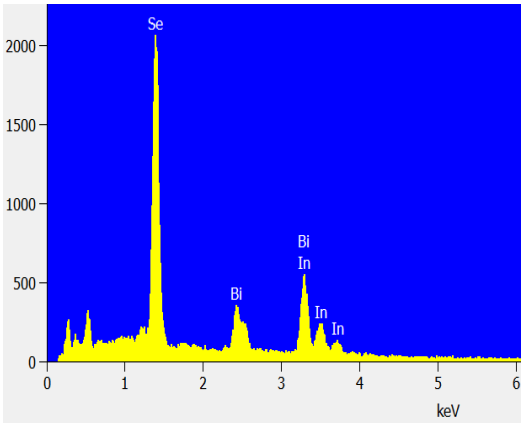


(f). $In_2Se_3$-10% Bi

**Figure 5.26 (a-f): EDS images of $In_2Se_3$-X% Bi annealed thin films samples**

Figure 5.26(a-f) shows EDS images of $In_2Se_3$: X% Bi thin films for all the samples. The results confirm presence of all the elements i.e selenium, Indium and bismuth.

### 5.9 Differential Scanning Calorimetry analysis

Differential Scanning Calorimetry (DSC) thermographs of $In_2Se_3$: X% Bi glasses obtained at constant rates of heating $\beta$ = 5, 10, 15, 20 and 25 K/min are presented in

figure 5.27. These figures exhibit single exothermic peak which represent crystallization transitions. The position of the peak is assigned to peak crystallization temperature $T_P$.

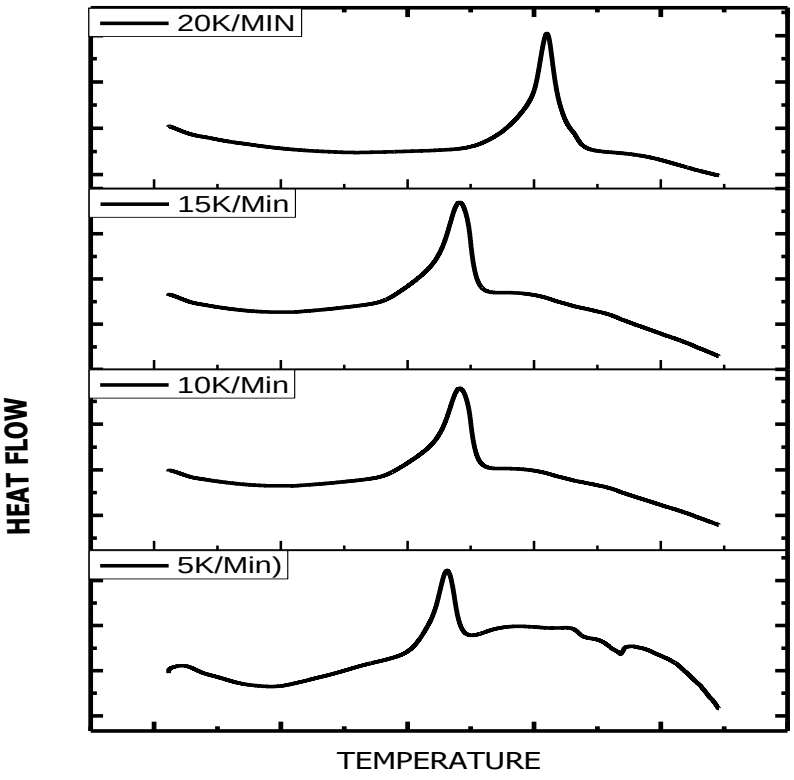


**Figure 5.27: DSC curves for 5, 10, 15 and 20K/min heating rates for $In_2Se_3$: X% Bi as-synthesized powder sample**

The measured values of $T_p$ for $In_2Se_3$: X% Bi material for various heating rates are tabulated in table 5.7 (a-e). From the values, it is conspicuous that $T_p$ increases with increase in percentage of bismuth. The change of $T_p$ with heating rates signifies the kinetic nature of glass transition. As the heating rates rise from 5 to 25K/min, $T_p$ shifts

towards higher temperature values. From these values, Kissinger equation was applied to derive a curve from which activation energy was determined.

**Table 5.7: Peak temperature values for $In_2Se_3$: X% Bi samples**

**(a) 5 k/min**

| **Sample** | 0 | 2 | 4 | 6 | 8 | 10 |
|---|---|---|---|---|---|---|
| **$T_p$(K)** | 339.15 | 339.48 | 340.02 | 341.09 | 370.11 | 371.09 |

**(b) 10 k/min**

| **Sample** | 0 | 2 | 4 | 6 | 8 | 10 |
|---|---|---|---|---|---|---|
| **$T_p$(K)** | 340.26 | 341.68 | 342.28 | 343.04 | 374.91 | 381.65 |

**(c) 15 k/min**

| **Sample** | 0 | 2 | 4 | 6 | 8 | 10 |
|---|---|---|---|---|---|---|
| **$T_p$(K)** | 376.45 | 378.45 | 380.76 | 396.39 | 398.033 | 403.39 |

**(d) 20 k/min**

| **Sample** | 0 | 2 | 4 | 6 | 8 | 10 |
|---|---|---|---|---|---|---|
| **$T_p$(K)** | 378.13 | 380.77 | 383.23 | 386.04 | 405.05 | 408.28 |

**(e) 25 k/min**

| **Sample** | 0 | 2 | 4 | 6 | 8 | 10 |
|---|---|---|---|---|---|---|
| **$T_p$(K)** | 382.62 | 383.28 | 389.45 | 391.79 | 409.48 | 411.78 |

Table 5.8 shows derived crystallization kinetics values while figure 5.28 shows a plot of $\ln(\beta T_p^{-2})$ versus $1000T_p^{-1}$ fitted using a linear fit for $In_2Se_3$: 0% Bi sample. The slope yields activation energy according to Kissinger model (Kissinger, 1957) which was found to be 0.231 eV for $In_2Se_3$: 0%Bi sample. This was repeated to yield tables 5.9 to 5.13 which resulted in curves 5.29 to 5.33 from which activation energies for the other samples were derived.

**Table 5.8: Crystallization kinetics values for $In_2Se_3$: 0% Bi samples**

| Heating rate β (K/min) | $T_p$ (K) | $1000T_p^{-1}(K^{-1})$ | $\ln(\beta T_p^{-2})$ |
|---|---|---|---|
| 5 | 339.15 | 2.957267 | -10.0375 |
| 10 | 340.26 | 2.938929 | -9.35683 |
| 15 | 376.45 | 2.656395 | -9.15352 |
| 20 | 378.13 | 2.644593 | -8.87474 |
| 25 | 382.62 | 2.613559 | -8.67521 |

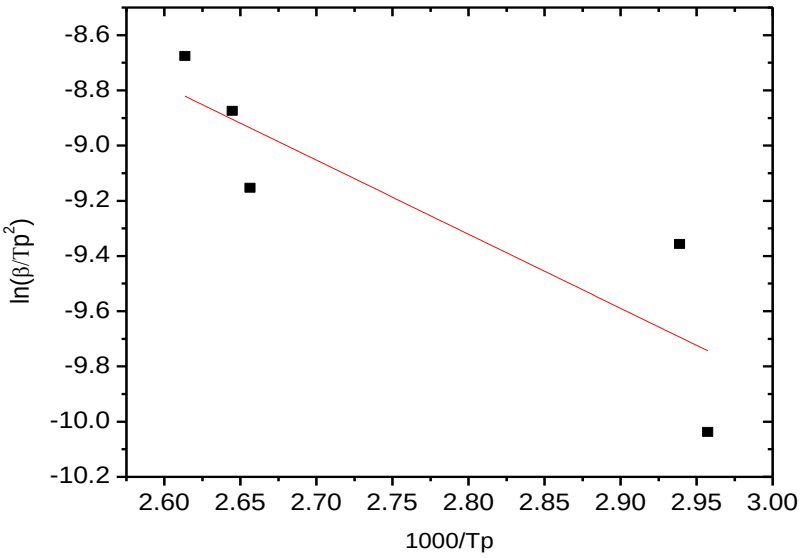


**Figure 5. 28: Plot of $\ln(\beta T_p^{-2})$ versus $1000T_p^{-1}$ for $In_2Se_3$: 0% Bi sample**

Crstallization kinetics values on table 5.8 were used to plot curve 5.28. The slope of the curve yielded the activation energy.

**Table 5.9: Crystallization kinetics values for $In_2Se_3$: 2% Bi samples**

| Heating rate β (K/min) | $T_p$ (K) | $1000T_p^{-1}(K^{-1})$ | $\ln(\beta T_p^{-2})$ |
|---|---|---|---|
| 5 | 339.48 | 2.945682 | -10.0454 |
| 10 | 341.68 | 2.926629 | -9.36522 |
| 15 | 378.45 | 2.642008 | -9.16438 |
| 20 | 380.77 | 2.626257 | -8.88866 |
| 25 | 383.28 | 2.609059 | -8.67866 |

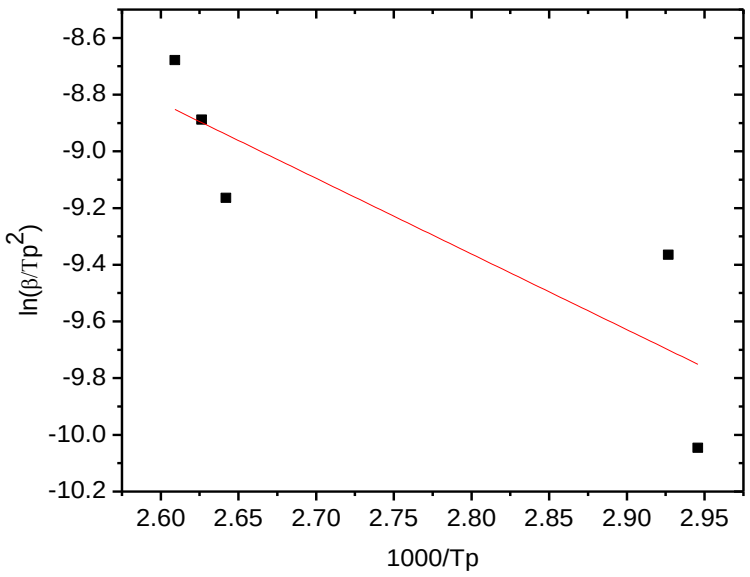


**Figure 5.29: Plot of $In(\beta T_p^{-2})$ versus $1000T_p^{-1}$ for $In_2Se_3$: 2% Bi sample**

Table 5.9 values were used to plot curve 5.29. From the slope of the curve, activation energy for the sample was derived.

**Table 5.10: Crystallization kinetics values for $In_2Se_3$: 4% Bi samples**

| Heating rate β (K/min) | $T_p$ (K) | $1000T_p^{-1}(K^{-1})$ | $In(\beta T_p^{-2})$ |
|---|---|---|---|
| 5 | 340.02 | 2.941003 | -10.048571 |
| 10 | 342.28 | 2.921585 | -9.3686731 |
| 15 | 380.76 | 2.642357 | -9.1641177 |
| 20 | 383.23 | 2.609399 | -8.9015384 |
| 25 | 389.45 | 2.567724 | -8.7105951 |

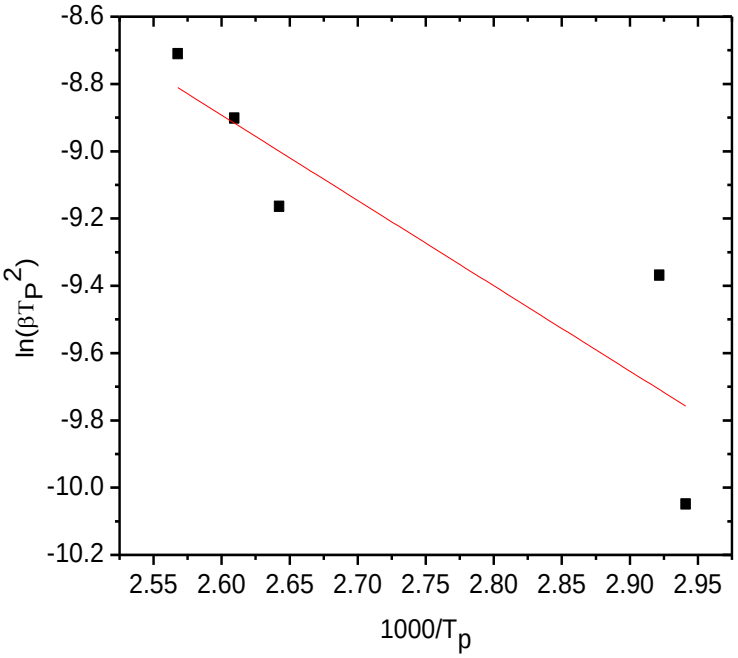


**Figure 5.30: Plot of $\ln(\beta T_p^{-2})$ versus $1000T_p^{-1}$ for $In_2Se_3$: 4% Bi sample**

The curve on figure 5.30 was derived from values on table 5.10. The slope gave activation energy.

**Table 5.11: Crystallization kinetics values for $In_2Se_3$: 6% Bi samples**

| Heating rate β (K/min) | $T_p$ (K) | $1000T_p^{-1}(K^{-1})$ | $\ln(\beta T_p^{-2})$ |
|---|---|---|---|
| 5 | 341.09 | 2.931778 | -10.054855 |
| 10 | 343.05 | 2.911632 | -9.375498 |
| 15 | 396.39 | 2.522768 | -9.2567469 |
| 20 | 386.04 | 2.590405 | -8.9161497 |
| 25 | 391.79 | 2.552388 | -8.7225761 |

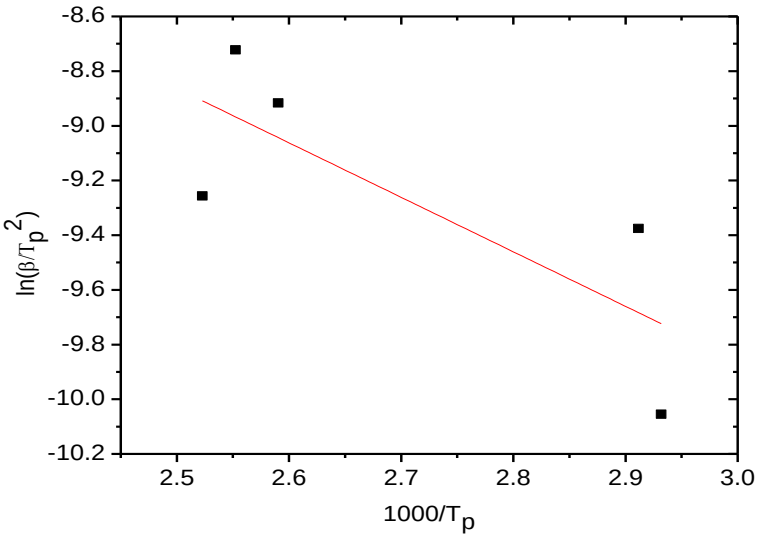


**Figure 5.31: Plot of $\ln(\beta T_p^{-2})$ versus $1000T_p^{-1}$ for $In_2Se_3$: 6%Bi sample**

Crystallization values on table 5.11 gave rise to curve on figure 5.31. Activation energy was derived from the slope of the curve.

**Table 5.12: Crystallization kinetics values for $In_2Se_3$: 8% Bi samples**

| Heating rate β (K/min) | $T_p$ (K) | $1000T_p^{-1}(K^{-1})$ | $\ln(\beta T_p^{-2})$ |
|---|---|---|---|
| 5 | 370.11 | 2.701899 | -10.218163 |
| 10 | 374.91 | 2.667307 | -9.5507869 |
| 15 | 398.03 | 2.512373 | -9.2650046 |
| 20 | 405.05 | 2.468831 | -9.0122888 |
| 25 | 409.48 | 2.442122 | -8.8109003 |

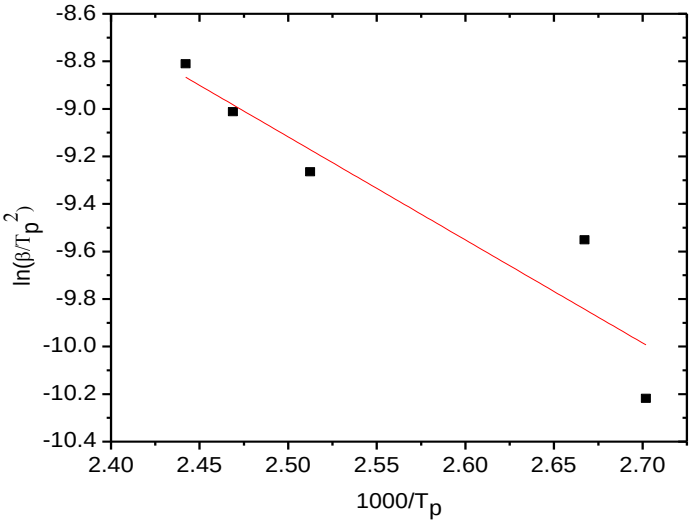


**Figure 5.32: Plot of $\ln(\beta T_p^{-2})$ versus $1000T_p^{-1}$ for $In_2Se_3$: 8%Bi sample**

Table 5.12 shows crystallization values for 8% sample. Curve 5.32 was plotted to give activation energy.

**Table 5.13: Crystallization kinetics values for $In_2Se_3$: 10% Bi samples**

| Heating rate β (K/min) | $T_p$ (K) | $1000T_p^{-1}(K^{-1})$ | $\ln(\beta T_p^{-2})$ |
|---|---|---|---|
| 5 | 371.69 | 2.690414 | -10.226682 |
| 10 | 381.65 | 2.620202 | -9.5864228 |
| 15 | 403.39 | 2.478991 | -9.2917575 |
| 20 | 408.28 | 2.4493 | -9.0281742 |
| 25 | 411.48 | 2.430252 | -8.820645 |

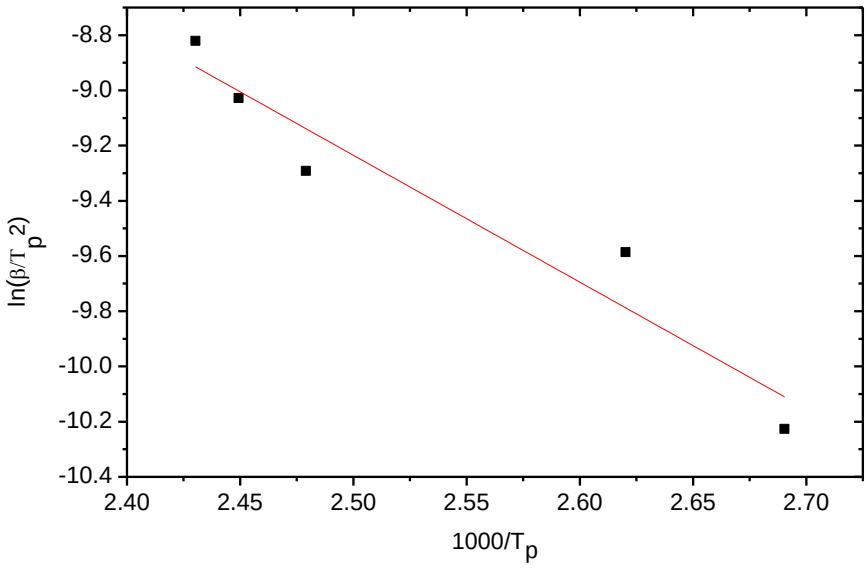


**Figure 5.33: Plot of $\ln(\beta T_p^{-2})$ versus $1000T_p^{-1}$ for $In_2Se_3$: 10% Bi sample**

Crystallization parameters for 10% Bi sample were tabulated on table 5.13. The values yielded curve 5.33 from where activation energy was derived. From figures 5.28 to 5.33, activation energy values were derived as listed in table 5.14.

**Table 5.14: Activation energy in eV for In2Se3: X% Bi (X=0, 2, 4, 6, 8 and 10%)**

| % Bi | 0 | 2 | 4 | 6 | 8 | 10 |
|---|---|---|---|---|---|---|
| Activation energy (eV) | 0.231 | 0.230 | 0.218 | 0.172 | 0.373 | 0.396 |

Table 5.14 shows values of activation energy for various samples of $In_2Se_3$: X% Bi (X = 0, 2, 4, 6, 8, and 10). The values range between 0.172 eV to 0.396 eV. The activation energy decreased with increase in bismuth for 0%, 2%, 4% and 6% Bi as shown in figure 5.34.

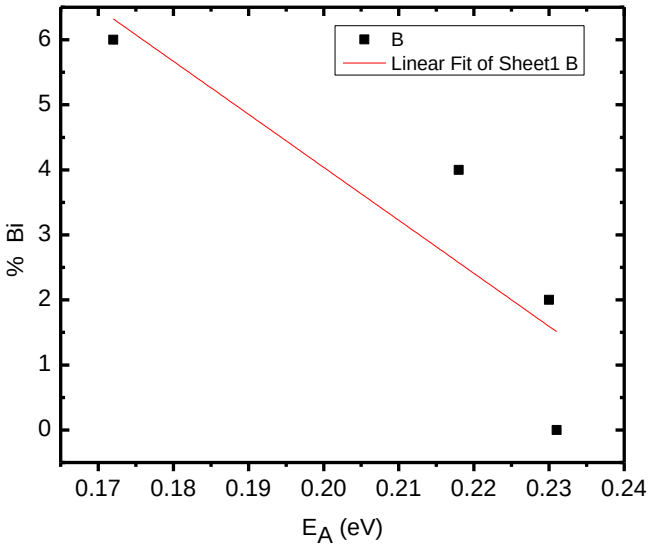


**Figure 5.34: A graph of percentage bismuth versus activation energy**

From figure 5.34, it is clearly portrayed that activation energy decreases with rise in bismuth concentration for 0 to 6% Bi concentration. However, at higher bismuth percentages of 8% and 10%, the material changes and activation energy increases with increase in bismuth concentration. This may be due to the fact that additional Bi atom is incorporated in cross-linking the Se chains by bonding with Se atoms. Further addition of Bi leads to a breaking of the chains and the formations of a large number of smaller chains (Ashraf and Zulfequar, 2019).

### 5.10 X-Ray Photoelectron Spectroscopy characterization

X-Ray Photoelectron Spectroscopy (XPS) spectra of the material sample give composition of the thin films. All samples showed similar results for XPS analysis. Figure 5.35 shows the XPS spectra for Indium where the $3d_{5/2}$ peak is at 445.0 eV and the

$3d_{3/2}$peak at 452.5 eV. The two peaks are analogous to spin orbit splitting of the d orbitals (Petroni *et al.*, 2018). Figure 5.36 illustrates the binding energies for Selenium for 3d orbitals as 54.3 eV. These correspond to the elemental state (Bindu *et al.*, 2002)**.**

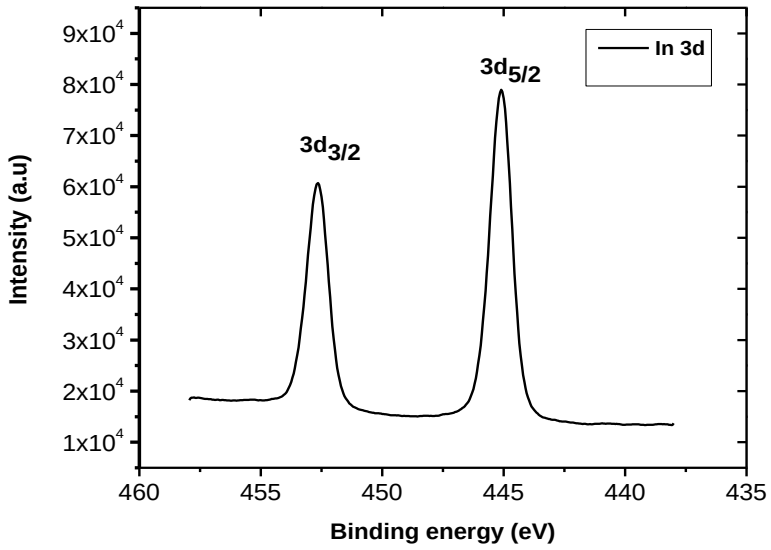


**Figure 5.35: XPS spectrum for Indium**

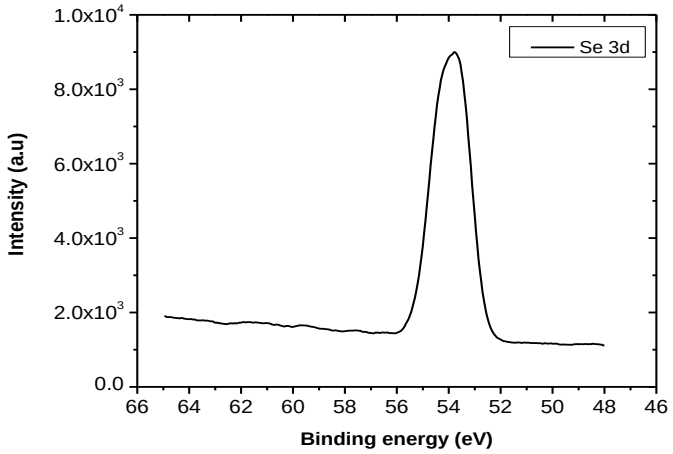


**Figure 5.36: XPS spectrum for selenium**

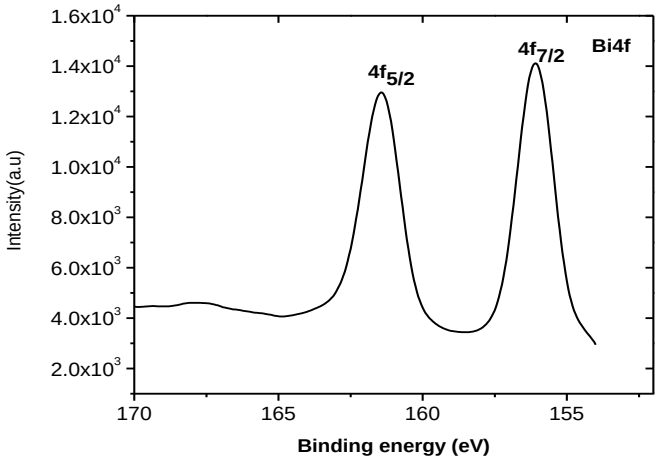


**Figure 5.37: XPS spectra for bismuth**

Figure 5.37 shows XPS spectra for Bismuth. Bi 4f region has well separated spin-orbit components (5.38 eV). The peaks in this region are asymmetric representing bismuth metal. The two peaks at 161.46 eV and 156.08 eV conform to Bi $4f_{5/2}$ and Bi $4f_{7/2}$ respectively. Similar results were documented by a group of researchers (Escobar-Alarcón*et al.,* 2015).

# CHAPTER SIX

# CONCLUSIONS AND RECOMMENDATIONS

## Conclusions

Powder samples and thin films of $In_2Se_3$:X%Bi (X= 0, 2, 4, 6, 8 and 10) were successfully synthesized and deposited respectively. Structural, optical, electrical, morphological and crystallization kinetics investigations on resulting samples were carried out. Powder samples quenched in liquid nitrogen were amorphous and transformed to polycrystalline upon annealing. The phase transformation was confirmed

using XRD technique. Crystallinity of both bulk and thin film samples increased with increase in bismuth concentration.

Thin films were prepared by evaporation technique employing pulsed laser deposition method. The resulting thin films of $In_2Se_3$:X% Bi were also found to be amorphous and changed phase to crystalline upon annealing. The film thicknesses were determined by alpha step method in addition to simulation of the optical transmittance by use of scout software. The film thicknesses from the two methods were in agreement. Diffuse reflectance curves were used to estimate band gap values using Kubelka Munk equation. It is evident that band gap values declined from 1.36 eV to 1.30 eV for as synthesized powder samples with increase in percentage bismuth. Similar observations were made for annealed samples where the band gap energy values decreased from 1.85 eV to 1.79 eV as percentage bismuth increases.

Electrical resistivity was found to decrease from 85.19 MΩcm to 22.96 MΩcm with increase in percentage bismuth. Activation energy of the samples was determined using Kissinger equation. It was found to decrease from 0.231 eV to 0.172 eV with increase in percentage bismuth for percentage values of 0% to 6%. There was change in behavior for higher percentage values of bismuth of 8% and 10% where activation energy increased with increase in bismuth concentration. This reduction in band gap energies and activation energy with increase in bismuth concentration means less switching time and low power consumption for a phase change memory device fabricated using $In_2Se_3$: X% Bi material. This may be attributed to the change in band gap and valence alternation pair

with doping. A valence alternation centre effectively pin the Fermi level but this effect is reduced by addition of charged elements (Fritzsche and Kastner, 1978).

A comprehensive analysis of the morphological properties and chemical composition of all samples was carried by FESEM and EDS respectively. From FE-SEM images the material was made up of agglomeration of irregularly shaped particles for as synthesized powder samples which appear to change in form after annealing. This is attributed to change of phase from amorphous to crystalline. For $In_2Se_3$:X% Bi thin films, SEM images depict spherical shaped particles irregularly distributed on the surface of the film. EDS results for both powder and thin films confirmed the three elements i.e indium, selenium and bismuth were present in the samples under test. XPS studies confirmed elemental composition of the samples where for indium $3d_{5/2}$ peak was at 445.0 eV and $3d_{3/2}$ peak was at 452.5 eV binding energies. The two peaks are associated with spin-orbit splitting of the d orbitals. XPS spectrum for selenium showed a peak for 3d orbitals at 54.3eV binding energy. Bismuth exhibits two asymmetrical peaks at $4f_{5/2}$ and $4f_{7/2}$ respectively.

From the discussion above, we can conclude that addition of Bismuth to the binary alloy of indium and selenium enhanced its qualities for use in phase change memory applications in terms of low power consumption and less switching time due to decrease in resistivity and activation energy.

**Recommendations**

After carrying out above analysis, it is recommended that a prototype of a phase change memory cell be fabricated and characterized from this material. Also there is need for a physics based model to allow simulation of a PCM device from $In_2Se_3$:X% Bi (where X = 0, 2, 4, 6, 8 and 10) material with the aim of optimizing the sample. X-ray absorption near edge structure (XANES) technique should be applied to understand better the structure of the memory cell.

## REFERENCES

Achamma, G., Sushama, D., Asokan, S., Awasthi, A. M. and Predee, P. (2007) Glass transformation studies in Ge-Se-Bi system. *Glass Physics and Chemistry*. **33**:562-568.

Agarwal, P., Goel, S., Tripathi, S. K. and Kumar, A. (1991) Amorphous to crystalline transition in glassy $Se_{100-x}In_x$. *Physica B.* **172**:511-516.

Aggarwal, I. D. and Sanghera, J. S. (2002) Development and applications of chalcogenide glass optical fibers. *Journal of Optoelectronics and Advanced Materials*. **4:**665-678.

Ashraf, S. S. and Zulfequar, M. (2019) Bismuth additive non-isothermal crystallization kinetics of $In_3Te_7BixSe_{90-x.}$ *Chalcogenide Letters.* **16**:603 – 614.

Allais, M. and Gandais, M. (1991) Growth study concerning Cd(S,Se) nanocrystals in silicate glass. High resolution transmission electron microscopy (HRTEM). *Materials Science and Engineering, B.* **9**:429-432

Alvin, M. A. (2014) Study of phase separation in amorphous Se-Te-Bi material. *Supalattices and microstructures.***73**:1-11.

Ardenne, M. V. (1937) Improvements in electronics microscopes, *British patent no 511204*, convention date (Germany) February.

Asokan, S., Prasad, M. V. N., Parthasarathy, G. and Gopal, E. S. R. (1989). Mechanical and chemical thresholds in IV-VI chalcogenide glasses. *Physics Review Letters.* **62**:808.

Ates, A., Kundakci, M., Amstam, A. and Yildirim, M. (2008). Annealing and light effect on optical and electrical properties of evaporated indium selenide thin films. *Physica E.* **40**:2709.

Ates, A., Atsam, A., Kundakci, M. and Yildirim, M. (2009) Characteristic properties of indium selenide thin films grown by the successive ionic layer adsorption and reaction method. *Journal of optoelectronics and advanced materials.* **11:**644-648.

Ball, J. and Moore, A. D. (1979) Essential physics for radiographers, Blackwell publishing, First edition, Oxford.

Barreau, N., Marsillac, S., Bernede, J. C., Nashallah, T. B. and Belgacem, S. (2001) Optical properties of wide band gap indium sulphide thin films obtained by physical vapor deposition. *Physica status solidi* A. **184**:179-186.

Bhargava, R. (1997) Properties of Wide Bandgap II-VI Semiconductor. *Inspec direct Publications, London.*

Bhat, N. A., Sangunni, K. S. and Rao, K. S. R. K. (2001) The role of defects in carrier type reversal in bismuth doped Ge-Se glasses by photoluminescence spectroscopy. *Journal of optoelectronics and advanced materials.* **3:**735-740.

Bindu, K., Lakshmi, M., Bini, S., Kartha, C. S., Vijayakumar, K. P., Abe, T. and Kashiwaba, Y. (2002) Amorphous selenium thin films prepared using chemical bath deposition: optimization of the deposition process and characterization. *Semiconductor Science and Technology*. **17**:270-274.

Boggs, S. and Krinsley, D. (2006) Application of cathodoluminesence imaging to the study of sedimentary rocks, Cambridge University Press, England.

Burr, G. W., Breitwisch, M. J., Francheschini, M., Garetto, D., Goparakrishna, K., Jackson, B., Kurdi, B., Lam, C., Lastras, L. A., Padilla, A., Rajidan, B., Raoux, S. and Shenoy, R. S. (2010) Phase change memory technology. *Journal of vacuum science and technology.* **28**:223-262.

Chen, R., and Mckeever, S. W. S. (1997) Theory of thermoluminescence and related phenomena, World scientific publishers, Singapore, London, Hong Kong.

Cheng, K. (2010) Evaluation of crystallization kinetics of glasses by non-isothermal analysis. *Journal of materials science.* **36**:1043-1048.

Choi, Y., Jung, M. and Lee Y. (2009) Effect of heating rate on the activation energy for crystallization of amorphous $Ge_2Sb_2Te_5$ thin film. *Electrochemical and solid-state letters.* **12**:F17-F19.

Choi, Y., Song, I., Park, M. H., Chung, H., Chang, S., Cho, B., Kim, J., Oh, Y., Kwon, D., Sunwoo, J., Shin, J., Rho,Y., Lee,C., Kang, M. G., Lee,J., Kwon, Y., Kim, S. Kim, J., Lee, Y. J., Wang, Q., Cha, S., Ahn, S., Horii, H., Lee, J., Kim, K., Joo, H., Lee,K., Lee,Y. T., Yoo, J. and Jeong, G. (2012) A 20nm 1.8V 8Gb PRAM with 40MB/s program bandwidth. Solid –state circuits conference digest of technical papers (ISSCC). *IEEE international.*

Chrisey D. B. and Hubler G.K (1994) Pulsed Laser Deposition of Thin Film, John Wiley & Sons, Inc., New York.

Cullity, B. D. (1956) Elements of X-ray diffraction. Addison Wesley publishing company, USA.

Damodardas, V. and Karunakaran, D. (1983) Semiconducting behavior of $Ag_2Te$ thin films and the dependence of band gap on thickness. *Journal of applied physics.* **54**:5252-5255.

Damon, R. W. and Redington, R. W. (1954) Electrical and Optical Properties of Indium Selenide. *Physical review*. **96**:1498–1500.

Davis, E. A. and Mott, N. F. (1970) Conduction in non-crystalline systems V. Conductivity, optical absorption and photoconductivity in amorphous semiconductors. *Philosophical Magazine.* **22:**903.

Egerton, R. F. (2005) Physical principles of electron microscopy: An introduction to TEM, SEM and AEM, Springer US, Berlin.

El-Oyoun, A. M. (2000) Crystallization kinetics of the chalcogenide $Bi_{10}Se_{90}$ glass. *Journal of physics and chemistry of solids.* **61**:1653-1662.

El–Sayed, S. M. (2004) Optical investigations of the indium selenide glasses. *Vacuum.* **72**:169–175.

El-Zahed, H. and El-Korashy A. ( 2000) Influence of composition on the electrical and optical properties of Ge-Bi-Se films. *Thin solid films.* **238:**236-240.

Escobar-Alarcón, L., Morales-Mendez, J. G., Solís-Casados, D. A., Romero, 1. S., Fernández1, M. and Haro-Poniatowski, E. (2015) Preparation and characterization of bismuth nanostructures deposited by pulsed laser ablation. *Journal of Physics.* **582:** 012013.

Fayek, S. A., Fadel, M., Abou-heral, M. O. and Shakra, A. M. (2008) Kinetic study of non-isothermal crystallization in SeGeX (X=O, Bi, In, and Sb) chalcogenide glasses. *Chalcogenide Letters.* **5**:317-331.

Fritzsche, H. and Kastner, M. (1978) The effect of charged additives on the carrier concentrations in lone-pair semiconductors. *Philosophical Magazine Part B.* **37**:285-292.

Geohegan, D. B., Puretzky, A. A. and Rader, D. L. (1999) Gas-phase nanoparticle formation and transport during pulsed laser deposition of $Y_1Ba_2Cu_3O_{7-d}$. *Applied Physics Letters.* **74**:3788.

Geusic, J. E., Marcos, H. M. and Uitert, L. G. (1966) Laser oscillations in Nd-Doped Yttrium aluminum, Yttrium gallium and gadolinium garnets. *Applied physics letters***.** **4**:182.

Gfroerer, T. H. (2000) Photoluminescence in analysis of surfaces and interfaces. In *Encyclopedia of Analytical chemistry*, R. A. Meyers (Ed.) 9209-9231, John Wiley & Sons Ltd, Chichester.

Goldstein, G. I., Newbury, D. E., Echlin, P., Joy, D. C., Fiori, C. and Lifshin, E. (1981) Scanning electron microscopy and x-ray analysis. Plenum press. Newyork.

Goldstein, J. I., Newbury, D. E., Joy, D. C., Lyman, C. E., Echlin, P., Lifshin, E., Sawyer, L. and Michael, J. R. (2003) Scanning electron microscopy and x-ray microanalysis,3rd edition, Kluwer Academic, New York.

Goo, H., Kwon, M. H., Kang, D., Lee, D. and Kim, K. B. (2011) New method of evaluating the crystallization activation energy of GST by In-situ resistance measurements. *Japanese Journal of Applied Physics.* **50:**020214.

Goodwin, T. J., Leppert, V. L., Risbud, S. H., Kennedy, I. M. and Lee, H.W.H. (1997) Synthesis of gallium nitride quantum dots through reactive laser ablation. *Applied Physics Letters.* **70**:3122.

Gopal, S., Viswanathan, C., Karunagaran, B., Narayandass, S. K., Mangalaraj, D. and Junsin, Y. (2005) Preparation and characterization of electrodeposited indium selenide thin films. *Crystal research and technology.* **40**:557–562.

Gupta, P., Lohia, P. and Dwivedi, D. K. (2021) Phase change memory: Operation, current challenges and future prospects. *International journal of engineering, science and technology.*
**13**:93-97.

Harrero, J. and Otega, J. (1987) Elechemical synthesis of photoactive $In_2Se_3$ thin films. *Solar energy materials.* **16**:477-485.

Hiereche, L. and Belhadgi, M. (2007) The methods Matusita, Kissinger and Ozawa in the study of crystallization of glasses. The case of Ge-Sb-Te Alloys. *Chalcogenide Letter.* **4**:23-33.

Hwang, Y. N., Hon, J. S., Lee, S. H., Ahn, S. I., Jeong, G. T., Koh, G. H., Oh, J. H., Kim, H. J., Jeong, W. C., Lee, S. Y., Park, J. H., Ryoo, K. C., Horii, H., Ha, Y. H., Yi, J. H., Cho, W. Y., Kim, Y. T., Lee, K. H., Joo, S. H., Park, S. O., Chung, U. I., Jeong, H. S. and Kim, K. (2003) Full integration and reliability evaluation of phase change RAM based on 0.24μm CMOS technologies, Samsung Electronics Symposium on VLSI Technology Digest of Technical Papers.

Imran, M. M., Bhandari, D. and Saxena, N. S. (2001) Enthalpy recovery during structural relaxation of $Se_{96}In_4$. chalcogenide glass. *Physica B:Condensed matter*. **293**:394-401.

Julien, C., Chevy, A. and Siapkas, D. (1990) Optical properties of $In_2Se_3$ phases. *Physica Status Solidi A***118**:553–559.

Kambo, M. S., Kaur, G. and Thangaraj, R. (2002) Dark and photoconductivity of amorphous Se-Te-Pb thin films. *Thin solid films.* **420**:350-353.

Karpov, V. G., Kryukov, Y. A., Savransky, S. D. and Karpov, I. V. (2007) Nucleation switching in phase change memory. *Applied physics letters* **90**:123504.

Kasap, S. O., Wagner, T., Aiyah, V., Krylouk, O., Bekirov, A., and Tichy, L. (1999) Amorphous chalcogenide Se1−x−y TexPy semiconducting alloys: thermal and mechanical properties. *Journal of materials science.* **34:**3779–3787.

Kastner, M. (1972) Bonding Bands, Lone-Pair Bands, and Impurity States in Chalcogenide Semiconductors. *physics review letters.* **28**:355-357.

Kastner, M., Aldler, D. and Fritzsche, H. (1976) Valence-Alternation Model for Localized Gap States in Lone-Pair Semiconductors. *physics review letters.* **37**:1504-1507.

Khan, Z. H., Zulfequar, M. and Hussain M. (1997*)* Optical properties of amorphous $Ga_{20}Se_{80-x}Bi_x$ thin films. *Journal of modern optics.* **44**:55-68.

Kim, K. and Ahn, S. J. (2005) Reliability investigations for manufacturable high density PRAM. *In IEEE International Reliabity Physics symposium* 157-162.

Kissinger, H. E. (1957**)** Reaction kinetics in differential thermal analysis. *Analytical chemistry.* **29:**1702-1706.

Kolobov, A. V. (1996) On the origin of p-type conductivity in amorphous chalcogenides. *Journal of non-crystalline solids.* **198**:723-731.

Komkov, O. S., Glinskii, G. F., Pikhtin, A. N. and Ramgolam, Y. K. (2009) Exciton effects and Franz-Keldysh oscillations in photo reflectance of ultrapure GaAs epilayers. *Physica status solidi A.* **206**:842-846.

Lakowicz, J. R. (2006) Principles of fluorescence spectroscopy. Springer, New york.

Lathrop, D. and Eckert, H. (1989) Chemical Disorder in Non-Oxide Chalcogenide Glasses. Site Speciation in the System Phosphorus-Selenium by Magic Angle Spinning NMR at Very High Spinning Speeds. *Journal of Physical Chemistry.* **93**:7895-7902.

Le Gallo, M. and Sebastian, A. (2020) An overview of phase-change memory device physics. *Journal of physics D: Applied physics.* **53**:213002.

Lopez-Riots, T. (2012) Enhanced Raman scattering mediated by long wave vector surface plasmonpolaritons. *Physical review B.* **85**:125438.

Lovu, M. S., Shutov, S. D. and Propescu, M. (2002) Relaxation of photodarkening in amorphous As–Se films doped with metals. *Journal of non-crystalline solids.* **299**:924-928.

Macfarlane, D. R., Matecki M. and Poulain M. (1984) Crystallization in fluoride glasses. *Journal of Non-Crystalline Solids.* **64**:351-362.

Madugu, M. L., Bowen, L., Echendu, O. K. and Dharmadasa, I. M. (2014) Preparation of indium selenide thin film by electrochemical technique. *Journal of materials science: Materials in electronics*. **25**:3977–3983.

Matsuzaki, N., Kuotsuchi, K., Matsui Y., Tonomura, O., Yamamoto, N., Fujisaki, Y., Kitai, N., Takemura, R., Osada, K., Hanzawa, S., Moriya, H., Iwasaki, T., Kawahara, T., Takaura, N., Terao, M., Matsuoka, M. and Moniwa, M. (2005) Oxygen doped GeSbTe phase change memory cells featuring 1.5V/100-standard 0.13m CMOS operations. In *IEDM Technical Digest* 738-741

Mattox, D. M. (1998) Hand book of physical vapour deposition (PVD) processing: film formation, adhesion, surface preparation and contamination control. Noyes Publications, New Jersey.

Matusita, K. and Sakka, S. (1979) Study on Crystallization Kinetics in Glass by Differential Thermal Analysis. *Thermochimicaacta.* **33**:351-354.

Mehra, R. M., Kohli, S., Pundir, A., Sachdev, V. K. and Mathur, P. C. (1997) n-Type conduction in Pb doped Se–In chalcogenide glasses. *Journal of applied physics.* **81**:7842-7844.

Mehta, N. and Kumar, A. (2005) Applicability of Kissinger's relation in the determination of activation energy of glass transition process. *Journal of optoelectronics and advanced materials.* **7:** 1473-1478.

Mehta, N., Zulfequar, M. and Kumar, A. (2004). Crystallization kinetics of some Se-Te-Ag chalcogenide glasses. *Journal of optoelectronics and advanced materials*. **6**:441-448.

Mehta, N., Zulfequar, M. and Kumar, A. (2005). Kinetic parameters of crystallization in glassy $Se_{100-x}Sb_x$ alloys. *Physical status solid*. **20**3:236-246.

Mendoza-Galván, A. and González-Hernández, J. (2000) Drude-like behavior of Ge:Sb:Te alloys in the infrared. *Journal of applied physics.* **87**(2):760-765.

Mercus, S. D. and Foster, R. F. (1993) Characterization of low pressure chemically vapor-deposited tungsten nitride films. *Thin solid films.* **236**:330-333

Merschjann, C., Schoke, B. and Imlau, M. (2007) Influence of chemical reduction on the particular number densities of light-induced small electron and hole polarons in nominally pure LiNbO3. *Physical review B.* **76**:085114.

Miyaji, K., Hung, C. and Takeuchi, K. (2012) Scaling trends and tradeoffs between short channel effect and channel boosting characteristics in Sub-20 nm Bulk/Silicon-on-Insulator NAND Flash Memory. *Japanese Journal of Applied Physic.* **51**(4): 04DD12.

Miyaji, K., Hung, C. and Takeuchi, K. (2011) Pushing scaling limit due to short channel effects and channel boosting leakage from 13nm to 8nm with SOI NAND Flash Memory Cells. *International Conference on Solid State Devices and Materials (SSDM)* 128-129.

Morale, A.E., Mora, E.S. and Pal, U. (2007) Use of diffuse reflectance spectroscopy for optical characterization of un-supported nanostructures. *Revista mexicana de física.* **53**:18.

Morikawa, T., Kurotsuchi, K., Kinoshita, M., Matsuzaki, N., Matsui, Y., Fujisaki, Y., Hanzawa, S., Kotabe, A., Terao, M., Moriya, H., Iwasaki, T., Matsuoka, M., Nitta, F., Moniwa, M., Koga, T. and Takaura, N. (2007). In *IEDM Technical Digest.* **12.3**:307-310.

Moskovits, M. (1985) Surface-enhanced spectroscopy. *Reviews of modern physics.* **57**:783-826.

Mott, N. F. (1967) Electrons in disordered structures. *Advances in Physics.* **16**:49-144

Mott, N. F. (1976) Increase in the conductivity of chalcogenide glasses by the addition of certain impurities. *Philosophical Magazine.* **34**: 1101-1106.

Mott, N. F., Davis, E. A. and Street, R. A. (1975) States in the gap and recombination in amorphous semiconductors. *Philosophical magazine.* **32**:961-996.

Nagels, P., Rotti, M. and Vikhrov, W. (1981) Doping of chalcogenide glasses in the Ge-Se and Ge-Te systems. *Journal physique.* **42**:907.

Nagels, P., Tichy, L., Tiska, A. and Ticha, H. (1983) Photoconductivity of vitreous chalcogenides chemically modified by Bismuth. *Journal of non-crystalline solids.* **59/60**:999.

Naseem, A., Muzamil, H., Nida, Z., Hassaan, A., Syed, M. Z. M., Uzair, S. and Mohammed, A. (2020) Optimization of Cr seed layer effect for surface roughness of as-deposited silver film using electron beam deposition method. *Journal- Chemical Society of Pakistan.* **42**:23-30.

Navinsek, B. and Panjan, P. (1993) Oxidation resistance of PVD Cr, Cr—N and Cr—N—O hard coatings. *Surface and coatings technology.* **59**:244-248.

Nilanthy, B., Christopher, R. S., Emily, F. S., Jakub, S., Dean, G., Garry, W. M., Oleg, M., Zakhar, R. K., Zakhar, D. K., Laurence, E., Amalia, P. and Peter, H. B. (2016) Quantum confinement and photoresponsivity of β-$In_2Se_3$ nanosheets grown by physical vapour transport. *2D Materials.* **3:**025030.

Nilanthy, B., Elisabeth, D. S., Emily, F. S., Zakhar, R. K., Zakhar, D. K., Laurence, E., Amalia, P. and Peter, H. B. (2018) Epitaxial growth of γ-InSe and α, β, and γ-In2Se3 on ε-GaSe. *2D Mateials.* **5:** 035026.

Njoroge, W. K., Woltgens, H. W. and Wuttig, M. (2001) Density changes upon crystallization of $Ge_2Sb_{2.04}Te_{4.74}$ films. *Journal of Vacuum Science and Technology.* **A20** (1):230-233.

Noufi, R., Axton, R., Herrington, C. and Deb, S.K. (1984) Electronic properties versus composition of thin films of $CuInSe_2$. *Applied Physics Lett*ers. **45**(6):668.

Ogugua, S. N., Ntwaeaborwa, O. M. and Swart, H. C. (2020) Latest development on pulsed laser deposited thin films for advanced luminescence applications. *Coatings.* **10**:1078.

Ovshinsky, S. R. (1968) Reversible Electrical switching phenomenon in Disorderd Structures. *Physics review letters.* **21**:1450.

Pandian, R. (1978) Phase change thin films: Resistance switching and isothermal crystallization studies. PHD Dissertation, University of Groningen, India.

Park, S., Kim, S. S., Yoon, S., Byoung, Y. and Choi, S. (2008) Phase transition, characteristics and device performance of Si-doped $Ge_2Sb_2Te_5$. *Semiconductor science and technology.* **23**:1-4.

Parlak, M. and Ercelebi, M. (1998) The effect of substrate and post-annealing temperature on the structural and optical properties of polycrystalline InSe thin films. *Thin solid films.* **322**:334–339.

Patel, C. K. N. (1964) Interpretation of $CO_2$ optical maser experiments. P*hysics Review Letters* **12:**588 -590.

Pesce, A. J., Rosen, C. G. and Pasby, T. L. (1971) Fleuroscence spectroscopy: An introduction for Biology and Mdecicine. Marcel Dekker, New York.

Peter. C. (2010) Phase-change memory found in handset. EETimes.UBMTechInsights.

Petroni, E., Lago, E., Bellani, S., Boukhvalov, D. W., Politano, A., Gürbulak, B. (2018) Liquid-phase exfoliated indium-selenide flakes and their application in hydrogen evolution reaction.

Pillai, S. O. (2010) Solid State Physics, New Age International Publications, New Delhi.

Poelman, D. and Smet, P. F. (2014) Time resolved microscopic cathodoluminescence spectroscopy for phosphor research. *Physica B.* **439:** 35-40.

Quan, D. T. (1987) SnSe thin films synthesized by solid state reactions. *Thin solid films*. **149**: 197-203.

Rabinal, M. K., Sangunni, K. S. and Gopal, E. S. R. (1995) Chemical ordering in $Ge_{20}Se_{80-x}In_x$ glasses. *Journal of non-crystalline solids***. 188**: 98-106.

Rao, K. J. and Mohan, R. (1980) Glass transition in As-Se glasses. *Journal of Physical Chemistry.* **84**: 1917.

Rao, T. L. S., Dhurundar, H. N., Kirit, N. L. A. and Pratap, A. (2008) Kinetic analysis of crystallization process in amorphous 2826A ($Ni_{36}Fe_{32}Cr_{14}P_{12}B_6$) metallic glass. *Indian journals of pure and applied physics.* **46**: 390-393.

Raoux, S., Jordan-sweet, J. L. and Kellock, A. J. (2008). Crystallization properties of ultrathin phase change films. *Journal of Applied physics.* **103**(11):114310.

Reinhold, E., Botzler, P. and Deus, C. (1991) EB-PVD process management for highly productive zirconia thermal barrier coating of turbine blades. *Surface and coatings technology*. **120-121**:77-83.

Schottmiller, J. C., Bowman, D. L. and Wood, C. (1968) New Vitreous Semiconductor. *Journal of applied physics*.**39:**1663-1669.

Schulz, U. and Schmucker, M. (1998) Microstructure of ZrO2 thermal barrier coatings applied by EB-PVD. *Materials Science and engineering A.* **276:** 1-8.

Sharma, A., Mehta, N. and Kumar, A. (2011) Dielectric relaxation in Se80-xTe20Snx chalcogenide glasses. *Journal of Material Science.* **46**:4509–4516.

Sharma, P., Sharma, V., Barman, P. B. and Katyal, S. C. (2012) Effect of bismuth addition on the optical band gap and extinction coefficient of thermally evaporated As-Se-Ge thin films. *Optoelectronics and advanced materials – rapid communications.* **6:**804-806.

Shay, J. L. and Nahory, R. E. (1969) Exciton reflectance and photoreflectance in GaAs. *Solid State Communications.***7**:945-948.

Shukla, R., Agarwal, P. and Kumar, A. (2010) Crystallization kinetics in glassy $Se_{100-x}$ In $_x$ system using iso-conversional methods. *Chalcogenide Letters.* **7**:249-255.

Singh, H., Singh, P., Singh, R., Sharma, J., Singh, A. P., Kumar, A. and Thakur, A. (2019) Composition dependent structural phase transition and optical band gap tuning in InSe thin films. *Heliyon* **5**: e02933

Singh, A. K., Singh. K. and Saxena, N. S. (2008). Effect of annealing on structures and effective thermal conductivity of $SE_{90}In_{10}$chalcogenide glass. *Journal of Ovonic Research.* **4:**107-111.

Singh, G., Sharma, J., Thakur, A., Goyal, N., Saini, G. S. S. and Tripath, S. K. (2005) Effect of bismuth on the electrical properties of a-$Ge_{20}Se_{80}$ glasses. *Jounal of optoelectronics and advanced materials.* **7:**2069-2076.

Smet, P. F., Botterman, J., Parmentier, A. B. and Poelman, D. (2013) Thermal quenching at the microscopic level in multi-phase thiosilicate phosphors. *Optical Materials.* **35**:1970-1975.

Smith, H. M. and Tuner, A. F. (1965) Vacuum deposited thin films using a ruby laser. *Applied optics.* **4**:147-148.

Smits, F. M. (1958) Measurement of sheet resistivities with the four-point probe. *Bell System Technical Journal*. **37**:711–718.

Suri. N, Bindra, K, and Thangaraj, R. (2006) Electrical conduction and photoconduction in $Se_{80-x}Te_{20}Bi_x$ thin films. *Journal of Physics: Condensed Matter*.**18**:9129.

Suri, N., Bindra, K. S., Kumara, P., Kambojb, M. S. and Thangaraj, R. (2006) Thermal investigations in bulk Se80-xTe20Bix chalcogenide glass. *Journal of Ovonic Research.* **2:**111-118.

Szczytko, J., Kappei, L., Berney, J., Morier-Genoud, F., Portella-Oberli, M. T. and Deveaud, B. (2005) Origin of excitonic luminescence in quantum wells: Direct comparison of the exciton population and Coulomb correlated plasma models. *Physical review* B .**71**:1953131-1953139.

Tanaka, K. (1989) Structural phase transitions in chalcogenide glasses. *Physical Review B.* **39**:1270.

Tohge, N., Minami, T. and Tanaka, M. (1983) Electrical properties of glasses in the Ge-Bi-Sb-Se and Ge-Bi-S systems. *Journal of non-crystalline solids.* **59/60:**1015.

Tohge, N., Minami, T., Yamamoto, Y. and Tanaka, M. (1980). Electrical and optical properties of n-type semiconducting chalcogenide glasses in the system Ge-Bi-Se. *Journal of applied physics* **51**:1048-1053.

Tohge, N., Yamamoto,Y., Minami, T. and Tanaka, M. (1979) Preparation of n-type semiconducting $Ge_{20}Bi_{10}Se_{70}$ glass. *Journal of applied physics letters.* **34:** 640.

Tominaga, J., Kikukawa, T., Takahashi, M. and Philips, R. T. (1997) Structure of optical phase change memory alloy, Ag-V-In-Sb-Te, determined by optical spectroscopy and electron diffraction. *Journal of Applied Physics.* **82**(7):3214-3218.

Valew, B. (2002) Molecular fleuroscence: principles and applications, wiley-VCH, Weinheim.

Vazquez, J., Barreda, D-G. G., Lopez-Alemany, P. L., Villare, P. and Jimenezi-Garay, R. (2004). Crystallization of $Ge_{0.08}Sb_{0.15}Se_{0.77}$ glass studied by DSC. *Journal of non-crystalline solids.* **345/346**:142-147.

Wang, Z., Tu, C., Li, Y. and Chen, Q. (1995) The effects of Sn and Bi additions on properties and structure in Ge-Se-Techalcogenide glass. *Journal of Non-Crystalline Solids.* **191:** 132-137.

Xia, X., Chen, Q., Tsay, C., Arnold, C. B. and Madsen, C. K. (2010) Low-loss chalcogenide waveguides on lithium niobate for the mid-infrared. *Optical letters.* **35**:3228-3230.

Yong, Y., Shasha, L., Yufeng, O., Yaxin, J., Zhou, Y., Lian, L., Chuanpeng, Y., Yong, Z., and Yong, Z. (2014) Effects of pressure and deposition time on the characteristics of $In_2Se_3$ films grown by magnetron sputtering. *Materials Letters.* **10:** 1093-1101.

Yamada, N., Ohno, E., Nishiuchi, K., Akahira, N. and Takao, M. (1991). Rapid-phase transitions of GeTe-$Sb_2Te_3$ pseodobinary amorphous thin-films for an optical disk memory. *Journal of Physics.* **69**(5):2849-2856.

Zahed, H. E. and Korashy, A. E. (2000) Influence of composition on the electrical and optical properties of $Ge_{20}Bi_xSe_{80-x}$ films. *Thin Solid Films.* **376**:236-240.

Zhang, Y., Gu, H. and Iijima, S. (1998) Single-wall carbon nanotubes synthesized by laser ablation in a nitrogen atmosphere. *Applied Physics Letters.***73**:3827.

Zogg, H. and Arnold, M. (2007) Narrow spectra band monolothic lead-chalcogenide-on-Si mid-IR photodetectors. *Infrared physics and technology.* **49**: 183-186.

# APPENDICES

## Appendix I


**Field Emission Scanning Electron Microscope at college of Science, Engineering and Technology, Department of Physics of the University of South Africa (UNISA) in Johannesburg, South Africa.**

## Appendix II

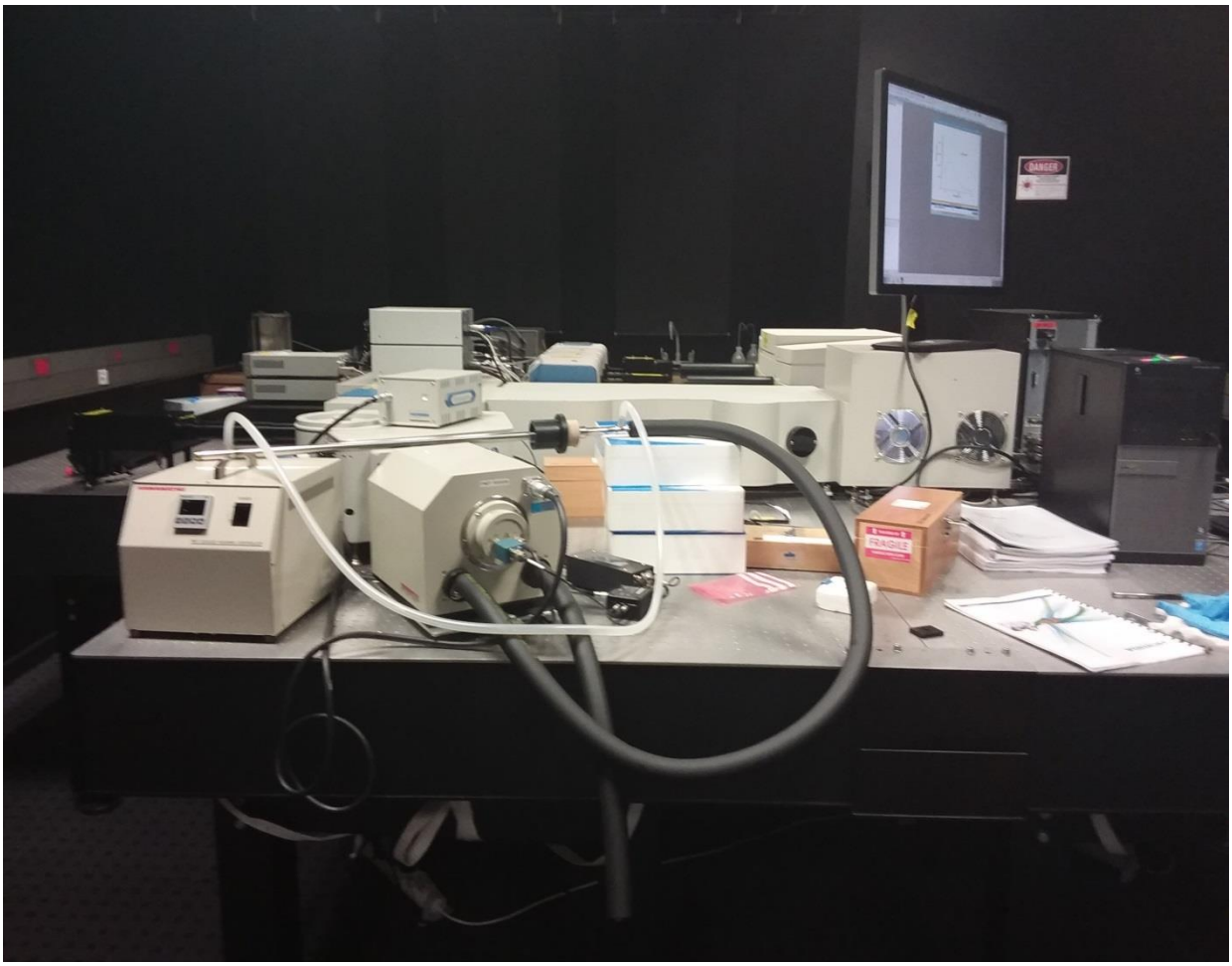


**UV-VIS Spectrophotometer at college of Science, Engineering and Technology, Department of Physics of the University of South Africa (UNISA) in Johannesburg, South Africa.**

Appendix III

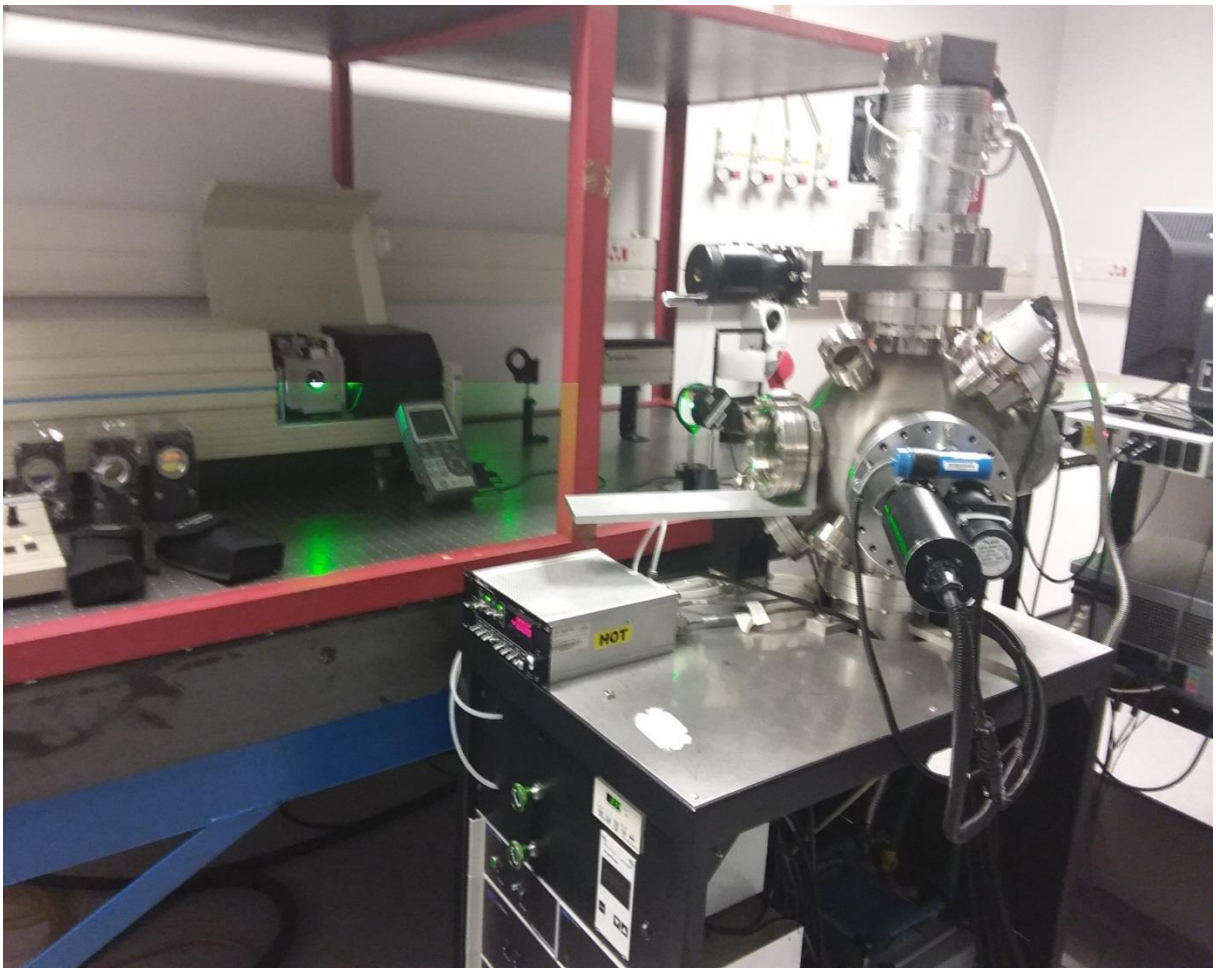


Pulsed laser deposition system at the Department of Physics of the University of the Free State (UFS), Bloemfontein, South Africa.